Development of Lagrangian numerical models for the simulation of the behavior of tidal turbines

Camille Choma Bex

Normandie Université

THÈSE

Pour obtenir le diplôme de doctorat

Spécialité MECANIQUE DES FLUIDES, ENERGETIQUE, THERMIQUE, COMBUSTION, ACOUSTIQUE

Préparée au sein de l'Université Le Havre Normandie

Développement de modèles numériques lagrangiens pour la simulation du comportement d'hydroliennes

Présentée et soutenue par
CAMILLE CHOMA BEX

Thèse soutenue le 09/07/2021 devant le jury composé de		
M. CHRISTOPHE CORRE	PROFESSEUR DES UNIVERSITES, ECOLE CENTRALE LYON	Rapporteur du jury
M. ERIC LAMBALLAIS	PROFESSEUR DES UNIVERSITES, UNIVERSITE POITIERS	Rapporteur du jury
MME LUMINITA DANAILA	PROFESSEUR DES UNIVERSITES, UNIVERSITE DE ROUEN NORMANDIE	Membre du jury
M. GRÉGORY PINON	MAÎTRE DE CONFERENCES (HDR), UNIVERSITE LE HAVRE NORMANDIE	Membre du jury
M. FRANCESCO SALVATORE	CHARGE DE RECHERCHE, CNR-INM, ROME	Membre du jury
MME MIREILLE BOSSY	DIRECTEUR DE RECHERCHE, INRIA SOPHIA ANTIPOLIS	Président du jury
M. ELIE RIVOALEN	PROFESSEUR DES UNIVERSITES, INST NAT SC APPLIQ ROUEN NORMANDIE	Directeur de thèse
M. GRÉGORY GERMAIN	INGENIEUR DE RECHERCHE (HDR), IFREMER	Co-directeur de thèse

Thèse dirigée par ELIE RIVOALEN et GRÉGORY GERMAIN, Laboratoire Ondes et Milieux Complexes

UNIVERSITÉ LE HAVRE NORMANDIE

ED 591 PSIME

LABORATOIRE ONDES et MILIEUX COMPLEXES

Acknowledgements

My most heartfelt and sincere thanks to all who have made this work possible ; beginning with my three co-supervisors, Elie Rivoalen, Grégory Germain, and Grégory Pinon, for their continued guidance as well as patience and understanding. I would also like to thank the teams of IFREMER in Boulogne for their welcome and support despite my distanced situation, as well as my colleagues from the LOMC in Le Havre for seeing me through this experience.

My thanks as well to Francesco Salvatore for his warm welcome in Rome, and for taking the time to make my brief stay at CNR-INSEAN both very enjoyable and enlightening.

Last but not least, my thanks to my family and friends who have supported me throughout all the ups and downs as well as particular challenges of the last few years.

Table of Contents

Introduction

The production of energy features among the central issues of our time. In the face of the imminent scarcity of fossil fuels and the reality of global warming, finding new sources of energy respectful of our environment is becoming a matter of urgency. France features among the countries investing heavily into the development of renewable energies. Given its geographical situation and the extent of its maritime area, marine renewable energies play an important part in this mix. After offshore wind energy development which is set to play a significant part in the near future with seven offshore parks currently under way, tidal and marine current energy displays the second most important exploitable energy source, with many potential energy locations under consideration. The french companies Sabella and Hydroquest have already deployed functioning prototypes in the sites of the Fromveur straight and Paimpol-Bréhat respectively. However the cost of technological development to pursue the highest level of Technology Readiness Level and the technical complications associated with the installation and maintenance of tidal turbine prototypes in very high current and difficult accessibility conditions remain somewhat prohibitive. While scaled flume tank models can provide many more detailed measurements and show interesting results within their specific controlled conditions, they remain limited in scale and accurate depiction of site conditions. It is therefore of great importance and current interest to also dispose of an arsenal of numerical solutions for the simulation of tidal turbine farms, with the ability to cover as many aspects of their functioning and realistic conditions as possible.

The scale of these simulation tools can vary from that of a whole tidal farm site including coastal topology and marine environment, to that of the detailed design of a turbine blade. With an expectation of reasonable computational costs, an array of methods can be considered, each better suited to one of these scales and with its own strengths and weaknesses. For instance, Blade Element Momentum Theory (BEM/BEMT) is a low cost method best suited to a general picture of energy output [1–4], while Large Eddy Simulation (LES) or full Computational Fluid Dynamics (CFD) will allow for a highly detailed account of the flow surrounding a turbine but require very high computational costs [5, 6]. Lagrangian methods are less common, and could be estimated as a middle of the pack type method in terms of compromise between detailed results and computational efficiency.

The Dorothy simulation code is a Lagrangian simulation code, developed in collaboration between IFREMER (Institut Français de Recherche pour l'Exploitation de la Mer) and LOMC (Laboratoire Ondes et Milieux Complexes) for the computation of tidal turbines. The development of this code has played an important role in the three back to back PhDs of Fabrice Maganga [7], Paul Mycek [8] and Clément Carlier [9]. While each of these research projects has focused on different aspects of the code and often been paired with experimental considerations, some basic principles remain unchanged, which is why Mycek and Carlier in particular will be often cited in the course of this continuation of their work. Aside from the constant and fruitful efforts towards the optimization of

the Dorothy software in collaboration with the CRIANN (Centre Régional Informatique et d'Applications Numériques de Normandie), it has been the object of many successive add-ons and improvements. The long term goal of these undertakings is to dispose of a comprehensive and eventually open-sourced tool for the simulation of tidal turbines, yielding results as accurate and representative as possible and encompassing as many of the conditions present and important to tidal sites as can be incorporated into the software. The first Chapter will provide a general description of the software's current capabilities and the Vortex Particle Method on which it is based.

Among the key conditions important to its continued development, the primary areas of focus of the work presented here have been the computation of efforts and the account for ambient turbulence, both integral to the estimation of the power output of a tidal turbine array. The first step consists in the simulation of a single turbine including its power output depending on the configuration of the upstream incoming flow, as well as the configuration of its wake and surrounding flow, which will be essential later on in order to account for turbine interactions. Most of the methods commonly used for these types of simulations will have a stronger emphasis on either the computation of efforts or of the fluid wake configuration. In the former category, BEM can easily provide good quality power results, as shown for instance in the works of Bahaj [10] or Batten [11], although it is limited by the fact that it relies on tabulated values. It is often paired with other methods necessary to obtain information on the wake, such as CFD in the works of Malki [12], or lifting line analogies. In the latter category, LES can provide highly detailed depictions of turbine wakes, however its computational cost remains prohibitive to its use for the computation of multi-turbine arrays. Other possibilities include potential codes, which can provide both wake and performance results, but require additional viscous corrections in order to operate in many conditions, as shown by Salvatore [13]. The Vortex Particle Method (VPM) used in the scope of this work performs well in terms of accurate depiction of turbine wakes, as has been shown by comparison with flume tank results [14]. However while the singularity method included within this framework could inform a detailed computation of localised efforts, it has shown to require additional developments to be fully satisfactory.

In the previous work of Mycek [8] and Carlier [9], an infinitely thin representation was used for the turbine blades. This infinitely thin representation of the blade is rather uncommon in the Lagrangian community where most prefer a full three dimensional representation of the blade [13,15–17], often coupling source and dipole distributions. These infinitely thin blades have allowed for very interesting results in terms of wake computations, together with the use of the Vortex Blob representation giving the opportunity to study very interesting features in terms of diffusion and turbulence modelling. However, from the earlier works of Pinon *et al.* [18] on, some discrepancies were identified regarding the evaluation of force and hence, the power and thrust coefficients of the turbine. The previous attempts in the PhD of Clément Carlier [9] focusing on refining this already existing thin blade representation did not solve the problem of performance evaluation. Furthermore, even if a solution could be found to overcome this issue, for the time being and to the best of our knowledge, the modelling of stall is not possible with such a representation. Therefore, in order to give this simulation code a chance to compute the power and thrust coefficients more accurately than is presently the case, and considering the possibility of the treatment of stall in a near future, the choice was made to move on to a full three-dimensional representation of the blades using an adapted panel method combining source and dipole distributions.

The first part of this manuscript will cover the basic methods used in the pre-existing software as well as those considered for this new adaptation. Chapter 1 will explain the

functioning of the "Dorothy" simulation code and the Vortex Particle Method on which it is based. Chapter 2 will then present the first key milestones towards a full three dimensional representation of turbine blades within this Lagrangian Vortex Blob framework.

Once it can be ensured that individual turbines are correctly accounted for, the next step consists in the simulation of tidal turbine arrays. With the increase of pre-commercial tidal farms (EnFAIT project, Meygen , etc.), it is becoming urgent to have tools to model such configurations with an accurate account of wake-turbine interactions. Karsten *et al.* [19] recently simulated hundreds of tidal turbines in the Bay of Fundy, Canada, with a linear momentum actuator disc theory in a regional code. Such studies were interesting for global resource assessment, and also possible global impact, but the methodology and discretisation used were not accurate enough to study turbine interactions. Similar conclusions could be drawn for the work of Divett *et al.* [20] using the Gerris code, even if the size of the farm was smaller (about 15 turbines) and using an adaptive mesh refinement. One of the first attempts very relevant for these types of pre-commercial farms was the study of Churchfield *et al.* [21], who computed 3D configurations of layouts with up to 5 turbines and using an LES code. However, the mesh was quite large (with up to 11×10^6 cells approximately) and, unfortunately at the time, the results were not compared to experimental data. Interactions between two aligned turbines to compare with the experimental results of Mycek *et al.* [22] were already attempted by the same research group using the Lagrangian Vortex framework (Mycek *et al.* [8]). These preliminary results were really promising, even though a better account of the blade was already invoked. This motivated us to enhance the software [18] so that the computations could be improved : larger array, finer discretisation, account of ambient turbulence, etc.

This last topic of ambient turbulence assessment in tidal energetic sites is of growing importance. Following the pioneering works of Osalusi *et al.* [23, 24] measuring ambient turbulence characteristics in the Fall of Warness at EMEC in Scotland, several research teams have carried on such investigations with increasing precision. Notable works include those of Thomson *et al.* [25] in the Puget Sound in western Canada, Milne *et al.* [26] in the Sound of Islay in the UK or even McCaffrey *et al.* [27] reanalysing some of Thomson *et al.*'s results with increased insights into the physics. These works paved the way for more recent studies such as [28–30]. Very recently, and very interestingly for a part of this PhD work pertaining to the Alderney Race, the results originating mainly from two French research programs (THYMOTE and HYD2M) were published, most of them in a special issue of the Philosophical Transaction of the Royal Society A [31–38]. All these works will be extremely valuable for the upcoming computations applied to farm configurations in the Alderney Race, and especially for the configuration which will be treated in the present work.

However simulating ambient turbulence can be a significant challenge. Most of the numerical codes being based on the Eulerian approach, the majority of the attempts were in this category. Therefore in most cases, an initialisation of the inlet boundary condition is necessary using a synthetic approach, being either the Synthetic Eddy Method (SEM) of Jarrin *et al.* [39], the Mann algorithm, or even predefined toolboxes such as TurbSim for instance. When using this technique, it is very complicated to maintain the ambient turbulence level over the entire computational domain, as was already largely highlighted for instance in the work of Jarrin *et al.*. Some research teams are trying to mitigate this phenomenon by either increasing the order of the numerical scheme and/or reducing the size of the mesh cells. Very interesting works in this respect were performed by Bernard *et al.* [40] in the wind energy sector, Ahmed *et al.* [6] in the tidal energy sector or even Mercier *et al.* [30, 41] also in the tidal energy sector using Lattice Boltzmann Method for the

last one. However the Lagrangian approach considered here is a very different formalism requiring an entirely different treatment. Chatelain *et al.* [42] have already performed computations with ambient turbulence in their Vortex-in-cell formalism. Bossy *et al.* [43] also applied a similar stochastic approach for computing interaction of wind turbines. Within this context, an adaptation of the SEM based on the initial works of Jarrin *et al.* [39] was integrated into the present Lagrangian Vortex software [44]. One of the major advantages of this approach is that the ambient turbulence level and characteristics are fully preserved throughout the entire computational domain, with no numerical damping whatsoever. This recently implemented ambient numerical approach combined with the accurate and fast numerical treatment of turbine-turbine interactions [45] make the Dorothy code a good candidate for computations of wake-turbine interactions in a farm.

This will be demonstrated in the second part of this manuscript, focusing on the addition of the account for ambient turbulence within the Dorothy simulation code. Chapter 3 will elaborate on the initial integration presented in the PhD work of Clément Carlier [9], detailing the formalism adapted from the work of Jarrin *et al.* [39] along with its thorough validation and the study of its impact on physical characteristics of the flow. Chapter 4 will show a similar study of an alternative implementation, based on a Diverge Free revision of Jarrin's initial SEM, namely the DFSEM of Poletto *et al.* [46], further improving on the physics of the method. Chapter 5 will demonstrate the effectiveness of the use of the present VPM software together with the initially integrated SEM for the simulation of turbine wakes and wake interactions, using the characteristics of a real considered test configuration within the Alderney Race.

Part I

Numerical methods for tidal turbine simulation

Chapter 1

Vortex Particle Method and DOROTHY simulation code

1.1 Introduction

Particle methods were among the first techniques to ever be used for the numerical simulation of fluids, starting in the 1930s with the pioneering calculations by hand of the evolution of a vortex sheet by Rosenhead [47] and continuing at the advent of Computational Fluid Dynamics in the 1970s with the works of Chorin [48] and Leonard [49]. The Vortex Particle Method originating with works such as those of Rehbach [50] describes the evolution of vortical flows. This allows for the restriction of computations to the sole areas where vorticity is present, easily adaptable to any configuration or combination of lifting bodies and obstacles to the flow.

These obstacles are accounted for using a singularity method, also known as boundary element or boundary integral method. Hess [51] was among the first to use this type of method for the computation of potential flows. Widely popularized as of the 1970s, a history of these methods and their origins can be found in Cheng and Cheng [52]. A later book by Bousquet [53] describes the thorough mathematical derivation of the singularity methods used in this current work.

Several developments have been undertaken at the LOMC in Le Havre for the past few decades, based on the Vortex Particle Method applied to Navier-Stokes' equations for an incompressible fluid, and later on combined with a singularity method for the account of obstacle surfaces. They have resulted in the simulation of vortex rings [54], marine propellers and wind turbines [55], boat sails [56, 57], transversal jets [58, 59], and now finally three-bladed horizontal axis tidal turbines [8, 18]. This latest iteration has lead to a collaboration with IFREMER, resulting in the creation of a dedicated simulation code named Dorothy.

1.2 Vortex Particle Method

This Section will present an overview of both the Vortex Particle and singularity methods as well as their numerical implementations, as used in the simulation code Dorothy. Many of these elements have already been described in the theses of Paul Mycek [8] and Clément Carlier [9], of which this work is the continuation. Chapter 2 will provide more details on the derivation of the singularity method specifically, along with an alternative to its current approach.

1.2.1 Navier-Stokes equations and velocity decomposition

Navier-Stokes Equations

The Navier-Stokes equations describe the velocity and pressure fields $(\boldsymbol{u}, p)$ of an incompressible unsteady flow :

$$\begin{cases} \boldsymbol{\nabla} \cdot \boldsymbol{u} = 0 & (1.1) \\ \dfrac{\partial \boldsymbol{u}}{\partial t} + (\boldsymbol{u} \cdot \boldsymbol{\nabla})\boldsymbol{u} + \dfrac{1}{\rho}\boldsymbol{\nabla} p = \nu \Delta \boldsymbol{u} & (1.2) \end{cases}$$

with ρ the fluid density and ν the cinematic viscosity.

Applying the rotational operator $\boldsymbol{\nabla}\times$ to the second equation leads to an alternative equivalent formulation in terms of velocity $\boldsymbol{u}$ and vorticity $\boldsymbol{\omega} = \boldsymbol{\nabla}\times \boldsymbol{u}$:

$$\begin{cases} \boldsymbol{\nabla} \cdot \boldsymbol{u} = 0 & (1.3) \\ \dfrac{D\boldsymbol{\omega}}{Dt} = (\boldsymbol{\omega} \cdot \boldsymbol{\nabla})\boldsymbol{u} + \nu \Delta \boldsymbol{\omega} & (1.4) \end{cases}$$

where the material derivative $\frac{D\boldsymbol{\omega}}{Dt}$ denotes :

$$\frac{D\boldsymbol{\omega}}{Dt} = \frac{\partial \boldsymbol{\omega}}{\partial t} + (\boldsymbol{u} \cdot \boldsymbol{\nabla})\boldsymbol{\omega} \; . \tag{1.5}$$

Velocity decomposition

Helmotlz's theorem states that any sufficiently smooth vector field $\boldsymbol{u}$ in a three-dimensional space can be written as the sum of an irrotational (curl-free) vector field and a solenoidal (divergence-free) vector field. If $\boldsymbol{u}$ is differentiable then there exist a scalar potential φ and vector potential $\boldsymbol{\psi}$ such that :

$$\boldsymbol{u} = \boldsymbol{\nabla}\varphi + \boldsymbol{\nabla}\times \boldsymbol{\psi} \; . \tag{1.6}$$

These potentials satisfy the relations :

$$\boldsymbol{\nabla}^2 \varphi = \theta \; , \tag{1.7}$$

where $\theta = \boldsymbol{\nabla}\cdot \boldsymbol{u}$ is the expansion of the velocity field $\boldsymbol{u}$ (with $\theta = 0$ for the case of an incompressible flow as prescribed by Equation (1.3)), and

$$\boldsymbol{\nabla}^2 \boldsymbol{\psi} = -\boldsymbol{\omega} \; . \tag{1.8}$$

For the sake of convenience, we can isolate an additional part of the velocity corresponding to the upstream incoming velocity, considered for the time being to be a fixed uniform constant value $\boldsymbol{u_\infty}$. Thus in the current chapter we consider $\boldsymbol{u}$ the entirety of the velocity field to be written as :

$$\boldsymbol{u} = \boldsymbol{u}^{\varphi} + \boldsymbol{u}^{\psi} + \boldsymbol{u_\infty} \; , \tag{1.9}$$

with $\boldsymbol{u}^{\varphi} = \boldsymbol{\nabla}\varphi$ the potential component of the velocity field, $\boldsymbol{u}^{\psi} = \boldsymbol{\nabla}\times \boldsymbol{\psi}$ its rotational component, and $\boldsymbol{u_\infty}$ the constant value of the irrotational upstream velocity.

The treatment of this decomposition will be covered once more in the following chapter, where a mathematical reasoning can lead to an interpretation of the potential component $\boldsymbol{u}^{\varphi}$ slightly different from the one presented hereafter. However these interpretations are not incompatible, as the method presented here and currently used for all turbine simulations can be considered as a particular case of the more general framework derived in Section 2.2.

1.2.2 Rotational velocity component

Formulation

The rotational component $\boldsymbol{u}^{\psi}$ of the velocity is derived from the vector potential $\boldsymbol{\psi}$. As stated in Equation (1.8), we have :

$$\boldsymbol{\nabla}^2 \boldsymbol{\psi} = -\boldsymbol{\omega} \ . \tag{1.10}$$

With the assumption that $\boldsymbol{\omega}$ vanishes at infinity with order r^{-3}, adding the condition that $\boldsymbol{\psi}$ goes to zero at infinity, the solution to Equation (1.10) is unique and given by :

$$\begin{aligned} \boldsymbol{\psi}(\boldsymbol{x}) &= -\int_{\boldsymbol{y}\in\mathbb{R}^3} \frac{1}{4\pi}\frac{1}{|\boldsymbol{y}-\boldsymbol{x}|}\,\boldsymbol{\nabla}_{\boldsymbol{y}}\times \boldsymbol{u}(\boldsymbol{y})dy \\ &= -\int_{\boldsymbol{y}\in\mathbb{R}^3} G(\boldsymbol{x},\boldsymbol{y})\boldsymbol{\omega}(\boldsymbol{y})dy \ , \end{aligned} \tag{1.11}$$

with G the Green function :

$$G(\boldsymbol{x},\boldsymbol{y}) = \frac{1}{4\pi}\frac{1}{|\boldsymbol{y}-\boldsymbol{x}|} \ . \tag{1.12}$$

The rotational velocity component $\boldsymbol{u}^{\psi}$ is then obtained by taking the rotational of the potential $\boldsymbol{\psi}$:

$$\begin{aligned} \boldsymbol{u}^{\psi}(\boldsymbol{x}) &= \frac{1}{4\pi}\int_{\boldsymbol{y}\in\mathbb{R}^3} \boldsymbol{\nabla}_{\boldsymbol{x}}\left(\frac{1}{|\boldsymbol{y}-\boldsymbol{x}|}\right)\times\boldsymbol{\omega}(\boldsymbol{y})dy \\ &= \frac{1}{4\pi}\int_{\boldsymbol{y}\in\mathbb{R}^3} \frac{\boldsymbol{y}-\boldsymbol{x}}{|\boldsymbol{y}-\boldsymbol{x}|^3}\times\boldsymbol{\omega}(\boldsymbol{y})dy \ . \end{aligned} \tag{1.13}$$

Noting $\boldsymbol{K}$ the Biot and Savart kernel :

$$\boldsymbol{K}(\boldsymbol{x},\boldsymbol{y}) = \frac{1}{4\pi}\frac{\boldsymbol{y}-\boldsymbol{x}}{|\boldsymbol{y}-\boldsymbol{x}|^3} \ , \tag{1.14}$$

we have finally :

$$\boldsymbol{u}^{\psi}(\boldsymbol{x}) = \int_{\boldsymbol{y}\in\mathbb{R}^3} \boldsymbol{K}(\boldsymbol{x},\boldsymbol{y})\times\boldsymbol{\omega}(\boldsymbol{y})dy \ . \tag{1.15}$$

Regularisation

The Biot and Savart kernel $\boldsymbol{K}$ has a singular behavior when $\boldsymbol{r} = \boldsymbol{y}-\boldsymbol{x}$ tends to zero. This singularity must be regularised for the sake of numerical computations. This is accomplished by introducing a desingularised Biot and Savart kernel $\boldsymbol{K}_{\epsilon}$ replacing the kernel K defined in Equation (1.14), such that :

$$\lim_{\epsilon\to 0} \boldsymbol{K}_{\epsilon} = \boldsymbol{K} \ , \tag{1.16}$$

where ϵ is a regularisation parameter to be specified as a parameter of the computations, depending on the chosen spacial discretisation.

Many possible expressions exist for regularisation functions and associated kernels [60]. In the present computations, the formulation chosen is that of Moore-Rosenhead :

$$\boldsymbol{K}_{\epsilon}(\boldsymbol{x},\boldsymbol{y}) = -\frac{1}{4\pi}\frac{\boldsymbol{y}-\boldsymbol{x}}{\left(|\boldsymbol{y}-\boldsymbol{x}|^2+\epsilon^2\right)^{3/2}} \ . \tag{1.17}$$

Paul Mycek's thesis [8] provides more detailed information on the choice and use of regularisation kernels in the simulation code Dorothy, as formulated for instance in the works of Beale and Majda [61].

From this point on, the rotational velocity component $\boldsymbol{u}^{\psi}$ is reconsidered accordingly :

$$\boldsymbol{u}^{\psi}(\boldsymbol{x}) \simeq \int_{\boldsymbol{y}\in\mathbb{R}^3} \boldsymbol{K}_{\epsilon}(\boldsymbol{x},\boldsymbol{y}) \times \boldsymbol{\omega}(\boldsymbol{y}) dy \ . \tag{1.18}$$

Discretisation

With the continuous expression for the rotational velocity established by Equation (1.18), it must now be transformed into a discrete formulation for the sake of numerical computations. To this end, the fluid domain is considered as a collection of individual subsets $(\mathscr{P}_i)_{i=1}^{N} \subset \mathbb{R}^3$, viewed as the supports of N fluid particles i. The rotational velocity $\boldsymbol{u}^{\psi}$ given by Equation (1.18) can be rewritten :

$$\boldsymbol{u}^{\psi}(\boldsymbol{x}) \simeq \sum_{i=1}^{N} \left(\int_{\boldsymbol{y}\in\mathscr{P}_i} \boldsymbol{K}_{\epsilon}(\boldsymbol{x},\boldsymbol{y}) \times \boldsymbol{\omega}(\boldsymbol{y}) dy \right) \ . \tag{1.19}$$

On the support $\mathscr{P}_i$ of each fluid particle i, the vorticity $\boldsymbol{\omega}$ is approximated by a constant $\boldsymbol{\Omega}_i$:

$$\boldsymbol{\Omega}_i = \int_{\boldsymbol{y}\in\mathscr{P}_i} \boldsymbol{\omega}(\boldsymbol{y}) dy \ . \tag{1.20}$$

Each fluid particle i is also assigned a central point :

$$\boldsymbol{x}_i = \frac{\displaystyle\int_{\boldsymbol{y}\in\mathscr{P}_i} \boldsymbol{y} \ dy}{\displaystyle\int_{\boldsymbol{y}\in\mathscr{P}_i} dy} \ , \tag{1.21}$$

and a volume :

$$V_i = \int_{\boldsymbol{y}\in\mathscr{P}_i} dy \ . \tag{1.22}$$

Finally, the discrete approximation of the rotational velocity $\boldsymbol{u}^{\psi}$ is given by :

$$\boldsymbol{u}^{\psi}(\boldsymbol{x}) \simeq \sum_{i=1}^{N} \boldsymbol{K}_{\epsilon}(\boldsymbol{x},\boldsymbol{x}_i) \times \boldsymbol{\Omega}_i \ . \tag{1.23}$$

This choice of representation of the fluid domain as an assembly of evolving and interacting particles is the key element of the Vortex Particle Method. This choice presents some notable advantages over its Eulerian counterparts, such as the ease and adaptability of the shape of the wake when interacting either with itself or with other turbines.

1.2.3 Potential velocity component

Formulation

As stated previously, the potential velocity component $\boldsymbol{u}^{\varphi}$ originating from the Helmholtz decomposition (1.9) derives from a velocity potential φ solution of the Poisson equation :

$$\boldsymbol{\nabla}^2 \varphi = 0 \ . \tag{1.24}$$

Figure 1.1: *Schematic representation of the passage from the "true" thick geometry of a turbine blade to the thin profile mean camber surface used in the simulations carried out with the Dorothy simulation code.*

One possible solution to this equation can be obtained by applying a singularity method [53] to the boundary surfaces of the objects placed in the flow, in this case tidal turbines. In the existing simulation code Dorothy, the tidal turbine and more specifically each turbine blade is approximated by its singular zero-thickness mean camber surface, as represented in Figure 1.1. This approximation allows for a simplification of the process of vorticity shedding into the turbine wake at the trailing edges of the mesh, where there is only one mesh face to consider per vorticity emission line, as will be seen later on.

Let $\mathscr{S}_B$ denote the grouping of all obstacle body surfaces in the flow. One possible solution to the Poisson Equation (1.24) is given by the velocity potential φ induced by a normal dipole distribution of intensity $\boldsymbol{\gamma} = \mu \boldsymbol{n}$, where $\boldsymbol{n}$ is the normal to the surface $\mathscr{S}_B$ and μ a scalar distribution on the surface $\mathscr{S}_B$:

$$\varphi(\boldsymbol{x}) = \int_{\boldsymbol{y} \in \mathscr{S}_B} \boldsymbol{K}(\boldsymbol{x}, \boldsymbol{y}) \cdot (\mu(\boldsymbol{y}) \boldsymbol{n}(\boldsymbol{y}))\, dy \;, \tag{1.25}$$

with $\boldsymbol{K}$ the Biot and Savart kernel defined in Equation (1.14). Within this framework, the distribution μ on $\mathscr{S}_B$ is treated as an unknown quantity. However it can be shown that the value of μ in this Equation corresponds to the potential jump over its surface of discontinuity $\mathscr{S}_B$: $\mu = \Delta\varphi$ (see for instance Appendix H of Paul Mycek's thesis [8]).

From this potential is derived the potential velocity component :

$$\begin{aligned} \boldsymbol{u}^{\varphi}(\boldsymbol{x}) &= \boldsymbol{\nabla}_{\boldsymbol{x}} \left[\int_{\boldsymbol{y} \in \mathscr{S}_B} \boldsymbol{K}(\boldsymbol{x}, \boldsymbol{y}) \cdot (\mu(\boldsymbol{y}) \boldsymbol{n}(\boldsymbol{y}))\, dy \right] \\ &= \int_{\boldsymbol{y} \in \mathscr{S}_B} \mu(\boldsymbol{y})\, \boldsymbol{\nabla}_{\boldsymbol{x}} \left[\boldsymbol{K}(\boldsymbol{x}, \boldsymbol{y}) \cdot \boldsymbol{n}(\boldsymbol{y}) \right] dy \;. \end{aligned} \tag{1.26}$$

Boundary condition

The unknown scalar dipole intensity μ is calibrated so as to ensure that the entire fluid velocity $\boldsymbol{u}$ verifies a slip condition along the surface $\mathscr{S}_B$. Noting $\boldsymbol{u}_B$ the relative velocity at each point of the surface $\mathscr{S}_B$, this slip condition can be written as :

$$\forall \boldsymbol{x} \in \mathscr{S}_B,\; \boldsymbol{u}(\boldsymbol{x}) \cdot \boldsymbol{n}(\boldsymbol{x}) = \boldsymbol{u}_B(\boldsymbol{x}) \cdot \boldsymbol{n}(\boldsymbol{x}) \;. \tag{1.27}$$

When replacing the velocity field $\boldsymbol{u}$ by its Helmholtz decomposition (1.9) we obtain :

$$\left(\boldsymbol{u}^{\varphi}(\boldsymbol{x}) + \boldsymbol{u}^{\psi}(\boldsymbol{x}) + \boldsymbol{u}_{\infty} \right) \cdot \boldsymbol{n}(\boldsymbol{x}) = \boldsymbol{u}_B(\boldsymbol{x}) \cdot \boldsymbol{n}(\boldsymbol{x}) \;, \tag{1.28}$$

i.e.

$$\boldsymbol{u}^{\varphi}(\boldsymbol{x}) \cdot \boldsymbol{n}(\boldsymbol{x}) = \left(-\boldsymbol{u}^{\psi}(\boldsymbol{x}) - \boldsymbol{u}_{\infty} + \boldsymbol{u}_B(\boldsymbol{x}) \right) \cdot \boldsymbol{n}(\boldsymbol{x}) \;. \tag{1.29}$$

For the case of a classic horizontal axis tidal turbine, the relative velocity $\boldsymbol{u}_B$ felt on the surface $\mathscr{S}_B$ is induced by the rotation of the turbine :

$$\forall \boldsymbol{x} \in \mathscr{S}_B,\; \boldsymbol{u}_B(\boldsymbol{x}) = \boldsymbol{\phi} \times \boldsymbol{OX} \;, \tag{1.30}$$

with O the center of rotation of the turbine, X the point of vector coordinates $\boldsymbol{x}$, and the vector $\boldsymbol{\phi}$ denoting the rotational speed of the turbine.

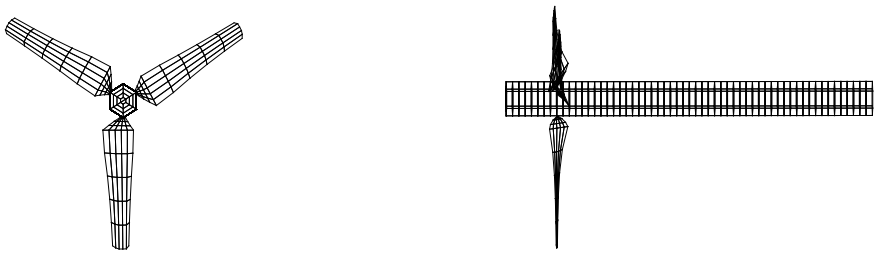

Figure 1.2: *Example of discretisation of a three-bladed horizontal axis tidal turbine into a zero-thickness quadrangular surface mesh.*

Discretisation

With the continuous expression for the rotational velocity established by Equation (1.26), it must also be transformed into a discrete formulation for the sake of numerical computations. To this end, the turbine body surface $\mathscr{S}_B$ is separated into mesh faces : $\mathscr{S}_B = \cup_{j=1}^{N_f} \mathscr{S}_j$. Figure 1.2 shows an example of this discretisation for a single tidal turbine. The potential velocity $\boldsymbol{u}^{\boldsymbol{\varphi}}$ of Equation (1.26) can then be written as :

$$\boldsymbol{u}^{\boldsymbol{\varphi}}(\boldsymbol{x}) = \sum_{j=1}^{N_f} \left(\int_{\boldsymbol{y} \in \mathscr{S}_j} \mu(\boldsymbol{y}) \, \boldsymbol{\nabla}_{\boldsymbol{x}} \left[\boldsymbol{K}(\boldsymbol{x}, \boldsymbol{y}) \cdot \boldsymbol{n}(\boldsymbol{y}) \right] dy \right) . \tag{1.31}$$

Each mesh face $\mathscr{S}_j$ is assigned a central point $\boldsymbol{x}_j$. Within the mesh face j, the normal $\boldsymbol{n}$ is assumed to be a constant value $\boldsymbol{n}_j = \boldsymbol{n}(\boldsymbol{x}_j)$, as is the dipole intensity μ_j. With these approximations, we now have :

$$\boldsymbol{u}^{\boldsymbol{\varphi}}(\boldsymbol{x}) = \sum_{j=1}^{N_f} \left(\mu_j \int_{\boldsymbol{y} \in \mathscr{S}_j} \boldsymbol{\nabla}_{\boldsymbol{x}} \left[\boldsymbol{K}(\boldsymbol{x}, \boldsymbol{y}) \cdot \boldsymbol{n}_j \right] dy \right) . \tag{1.32}$$

Through a series of mathematical and geometrical manipulations, the semi-discrete above expression is transformed into a fully discrete formulation, assuming an entirely quadrangular mesh :

$$\boldsymbol{u}^{\boldsymbol{\varphi}}(\boldsymbol{x}) = \frac{1}{4\pi} \sum_{j=1}^{N_f} \left(\mu_j \sum_{k=1}^{4} \boldsymbol{\alpha}_j^k(\boldsymbol{x}) \right) . \tag{1.33}$$

Using the notations shown in Figure 1.3 : X is the point of coordinates $\boldsymbol{x}$ where the velocity is being evaluated, C_j the central point of coordinates $\boldsymbol{x}_j$ of the mesh face $\mathscr{S}_j$, $(P_j^k)_{k=1}^4$ its four corner points, and the vectors $\boldsymbol{r}_j^k = \boldsymbol{X}\boldsymbol{P}_{\boldsymbol{j}}^{\boldsymbol{k}}$; the vector coefficient $\boldsymbol{\alpha}_j^k$ can be written as :

$$\boldsymbol{\alpha}_j^k(\boldsymbol{x}) = \left[|\boldsymbol{r}_j^k| + |\boldsymbol{r}_j^{k+1}| \right] \left[1 - \frac{\boldsymbol{r}_j^k \cdot \boldsymbol{r}_j^{k+1}}{|\boldsymbol{r}_j^k||\boldsymbol{r}_j^{k+1}|} \right] \frac{\boldsymbol{r}_j^k \times \boldsymbol{r}_j^{k+1}}{|\boldsymbol{r}_j^k \times \boldsymbol{r}_j^{k+1}|^2} , \tag{1.34}$$

where $k+1$ is defined modulo 4. The passage from the semi-discrete formulation of Equation (1.32) to the fully discrete formulation of Equation (1.33) is detailed in pages 305-338 of Bousquet's book [53].

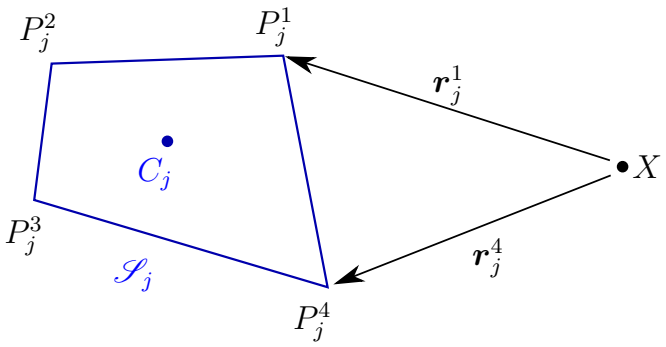

Figure 1.3: *Schematic representation of a mesh face $\mathscr{S}_j$ showing the notations used to compute its interaction with a distant point X.*

Dipole intensities

The last remaining step for the definition of the potential velocity component $\boldsymbol{u}^{\varphi}$ is the calculation of the dipole intensities μ_j on each mesh face j. To this end, the slip condition (1.29) is applied to each mesh face center point $\boldsymbol{x}_j$:

$$\forall j \in [\![1, N_f]\!], \quad \boldsymbol{u}^{\varphi}(\boldsymbol{x}_j) \cdot \boldsymbol{n}_j = \Big(-\boldsymbol{u}^{\psi}(\boldsymbol{x}_j) - \boldsymbol{u}_{\infty} + \boldsymbol{u}_B(\boldsymbol{x}_j)\Big) \cdot \boldsymbol{n}_j \ . \tag{1.35}$$

This condition can be written in the form of a linear system of size $N_f \times N_f$ and unknown $\boldsymbol{\mu} = (\mu_j)_{j=1}^{N_f}$:

$$\overline{\overline{\boldsymbol{A}}}\boldsymbol{\mu} = \boldsymbol{b} \ . \tag{1.36}$$

The coefficients A_{ij} of the influence matrix $\overline{\overline{\boldsymbol{A}}}$ are given by :

$$A_{ij} = \frac{1}{4\pi} \sum_{k=1}^{4} \boldsymbol{\alpha}_j^k(\boldsymbol{x}_i) \cdot \boldsymbol{n}_i \ , \tag{1.37}$$

and the coefficients b_i of the vector $\boldsymbol{b}$:

$$b_i = \Big[\boldsymbol{u}_B(\boldsymbol{x}_i) - \boldsymbol{u}^{\psi}(\boldsymbol{x}_i) - \boldsymbol{u}^{\infty}\Big] \cdot \boldsymbol{n}_i \ . \tag{1.38}$$

All of these quantities are known or can be computed. Thus, the resolution of this linear system will provide dipole intensities μ_j to be entered into the discrete formulation (1.33) for the potential velocity component $\boldsymbol{u}^{\varphi}$. This completes the definition of the potential component $\boldsymbol{u}^{\varphi}$ and ensures that the fluid velocity will respect the slip condition along obstacle surfaces as formulated in Equation (1.27).

Mycek *et al.* [45] provide more details on the numerical treatment of the resolution of this linear system in the Dorothy simulation code.

1.2.4 Particle emission

The potential velocity component representing the influence of the turbine bodies and the rotational velocity component representing the influence of their vortical wake are connected through the emission of fluid particles at the trailing edges of the lifting body meshes. This release of vortices is caused by the discontinuity of the velocity field between the innner and outer sides (intrados and extrados) of the surfaces representing the obstacles to the flow.

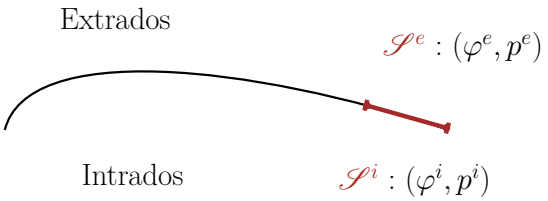

Figure 1.4: *Schematic representation of a thin blade profile showing both sides of its trailing edge mesh face.*

Bernoulli relation

This discontinuity is characterized using Bernoulli's relation, under the assumption that the fluid velocity is predominantly potential in the vicinity of the lifting body surface meshes. Bernoulli's relation, for an unsteady potential irrotational flow $\boldsymbol{u}^{\boldsymbol{\varphi}}$ can be written as formulated by Batchelor [62] :

$$\frac{\partial \varphi}{\partial t} + \frac{1}{2}(\boldsymbol{u}^{\boldsymbol{\varphi}})^2 + \frac{p}{\rho} + gz = f(t) \,, \tag{1.39}$$

where the function $f(t)$ depends only on time and not on position in the fluid, z denotes the altitude and g the gravitational acceleration.

When considering this relation on the extrados and intrados sides $\mathscr{S}^e$ and $\mathscr{S}^i$ of the same emission face $\mathscr{S}$ along the blade trailing edge as shown in Figure 1.4 and writing the difference between the two expressions at any time t, we obtain :

$$\frac{\partial}{\partial t}(\varphi^e - \varphi^i) + \frac{1}{2}\left((\boldsymbol{u}^{\boldsymbol{\varphi}^e})^2 - (\boldsymbol{u}^{\boldsymbol{\varphi}^i})^2\right) + \frac{p^e - p^i}{\rho} + g(z^e - z^i) = 0 \,. \tag{1.40}$$

Along the trailing edge, $p^e = p^i$ and $z^e = z^i$. Thus :

$$\frac{\partial}{\partial t}(\varphi^e - \varphi^i) + \frac{1}{2}\left((\boldsymbol{u}^{\boldsymbol{\varphi}^e})^2 - (\boldsymbol{u}^{\boldsymbol{\varphi}^i})^2\right) = \frac{\partial}{\partial t}(\varphi^e - \varphi^i) + \frac{\boldsymbol{u}^{\boldsymbol{\varphi}^e} + \boldsymbol{u}^{\boldsymbol{\varphi}^i}}{2} \cdot \left(\boldsymbol{u}^{\boldsymbol{\varphi}^e} - \boldsymbol{u}^{\boldsymbol{\varphi}^i}\right) = 0 \,. \tag{1.41}$$

Let $\boldsymbol{u}_{\boldsymbol{m}}^{\boldsymbol{\varphi}} = \dfrac{\boldsymbol{u}^{\boldsymbol{\varphi}^e} + \boldsymbol{u}^{\boldsymbol{\varphi}^i}}{2}$ denote the average potential flow at the trailing edge. Recalling that $\boldsymbol{u}^{\boldsymbol{\varphi}} = \boldsymbol{\nabla}\varphi$ and $\mu = \Delta\varphi$, i.e. at the trailing edge $\mu = \varphi^e - \varphi^i$, the previous expression can be translated as :

$$\frac{\partial \mu}{\partial t} + \boldsymbol{u}_{\boldsymbol{m}}^{\boldsymbol{\varphi}} \cdot \boldsymbol{\nabla}\mu = 0 \,, \tag{1.42}$$

which indicates that the distribution of normal dipoles μ is introduced into the flow with the initial velocity $\boldsymbol{u}_{\boldsymbol{m}}^{\boldsymbol{\varphi}}$ from the trailing edges.

Configuration

The vorticity induced by the normal dipole distribution is first assumed to be shed in the form of "imaginary" added mesh faces placed in the continuation of each trailing edge mesh face. By applying the Kutta condition to these trailing edges, we can establish that the contribution of the new imaginary wake faces is that of a normal dipole with the same intensity μ_k as its corresponding emission face. This reasoning is further detailed in Paul Mycek's thesis [8]. These contributions will later on be converted in the forms of vorticity carrying fluid particles, as formulated in Paragraph 1.2.2.

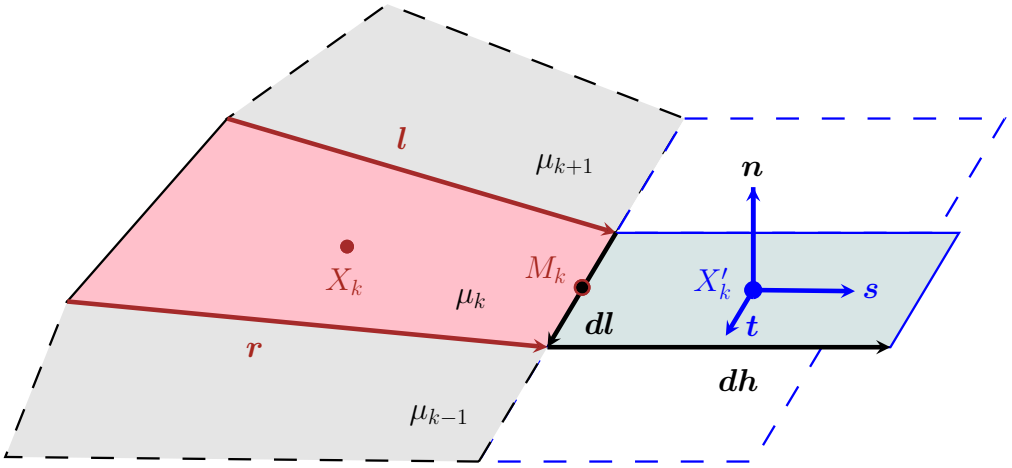

Figure 1.5: *Schematic representation of the emission of an imaginary wake mesh face $\mathscr{S}'_k$ behind the trailing edge mesh face $\mathscr{S}_k$.*

For the time being, let us consider a mesh face $\mathscr{S}_k$ situated at the trailing edge of the solid body surface mesh, and $\mathscr{S}'_k$ the associated imaginary face placed in its wake, as shown in Figure 1.5. The points X_k and X'_k of vector coordinates $\boldsymbol{x}_k$ and $\boldsymbol{x}'_k$ denote the centers of $\mathscr{S}_k$ and $\mathscr{S}'_k$ respectively. Three vectors $(\boldsymbol{s}, \boldsymbol{n}, \boldsymbol{t})$ form the basis of a frame of reference linked to the imaginary face $\mathscr{S}'_k$.

The newly emitted imaginary face is considered to be rectangular in shape, driven by the vectors $\boldsymbol{dl}$ corresponding to the emission segment and $\boldsymbol{dh}$ based on the emission velocity. The emission velocity $\boldsymbol{u}^{\varphi}_{\boldsymbol{m}}$ defined in the previous paragraph is approximated to :

$$\boldsymbol{u}^{\varphi}_{\boldsymbol{m}} \simeq \boldsymbol{u}(\boldsymbol{m}) \,, \tag{1.43}$$

where the vector $\boldsymbol{m}$ corresponds to the middle point M_k of the emission line, from which we obtain :

$$\boldsymbol{dh} = \boldsymbol{u}^{\varphi}_{\boldsymbol{m}} dt \,, \tag{1.44}$$

with dt the timestep of the simulation. At the first iteration of the simulation, when the dipole intensities μ and thus the potential velocity $\boldsymbol{u}^{\varphi}$ have yet to be established, the driving vector $\boldsymbol{dh}$ is assumed instead to prolong the sides $\boldsymbol{r}$ and $\boldsymbol{l}$ of the corresponding emission face :

$$\boldsymbol{dh} = \frac{\boldsymbol{r} + \boldsymbol{l}}{2} \,. \tag{1.45}$$

The unit vectors $(\boldsymbol{s}, \boldsymbol{n}, \boldsymbol{t})$ are deduced from these directions : $\boldsymbol{t} = \dfrac{\boldsymbol{dl}}{dl}$, $\boldsymbol{s} = \dfrac{\boldsymbol{dh}}{dh}$, and $\boldsymbol{n} = \boldsymbol{t} \times \boldsymbol{s}$.

From mesh faces to particles

The contribution of the mesh faces thus established could be computed as the velocity induced by a normal dipole distribution of intensities μ'_k on each imaginary face $\mathscr{S}'_k$, and the turbine wake accounted for as an additional mesh. However for the sake of this Lagrangian formulation, the contributions of the normal dipoles μ'_k on the faces $\mathscr{S}'_k$ must be converted into equivalent fluid particles $\mathscr{P}'_k$.

To this end, we use the equivalence detailed in the appendices to Paul Mycek's thesis [63]. This reasoning states that the potential velocity $\boldsymbol{u}^{\phi}$ induced by a normal dipole

distribution on any surface $\mathscr{S}$ can be equated to the contribution of two distinct vortices [64]. The first vortex sheet of intensity $\boldsymbol{\Gamma} = \boldsymbol{n} \times \boldsymbol{\nabla}\mu$ is attached to the surface $\mathscr{S}$ itself, while a second vortex line of intensity $\mu\boldsymbol{dl}$ is concentrated on its contour $\mathscr{C}$. Therefore, the vortex particle $\mathscr{P}'_k$ equivalent to the imaginary mesh face $\mathscr{S}'_k$ is attributed a vortical weight $\boldsymbol{\Omega}'_k$ corresponding to the intensity $\boldsymbol{\Gamma}'_k = \boldsymbol{n} \times \boldsymbol{\nabla}\mu$ integrated on the surface of the imaginary face $\mathscr{S}'_k$:

$$\begin{aligned} \boldsymbol{\Omega}'_k &= \int_{\boldsymbol{y}\in\mathscr{S}'_k} \boldsymbol{n}(\boldsymbol{y}) \times (\boldsymbol{\nabla}\mu(\boldsymbol{y}))\, dy && (1.46)\\ &\simeq \int_{\boldsymbol{y}\in\mathscr{S}'_k} \boldsymbol{n}'_k \times (\boldsymbol{\nabla}\mu(\boldsymbol{x}_k))\, dy && (1.47)\\ &= dh\ dl\ \boldsymbol{n}'_k \times \boldsymbol{\nabla}\mu_k\ , && (1.48) \end{aligned}$$

where $\boldsymbol{n}'_k = \boldsymbol{n}$ is the normal to the imaginary face $\mathscr{S}'_k$ and $\boldsymbol{\nabla}\mu(\boldsymbol{x}_k) = \boldsymbol{\nabla}\mu_k$ is the spacial gradient of the dipole intensity μ evaluated at the center X_k of the emission face $\mathscr{S}_k$.

The vector intensity $\boldsymbol{\Gamma}'_k = \boldsymbol{n} \times \boldsymbol{\nabla}\mu_k$ can be projected onto the local frame of reference $(\boldsymbol{s}, \boldsymbol{n}, \boldsymbol{t})$:

$$\begin{aligned} \boldsymbol{\Gamma}'_k &= \boldsymbol{n} \times \boldsymbol{\nabla}\mu_k \\ &= \boldsymbol{n} \times (\boldsymbol{\nabla}_{\boldsymbol{s}}\mu_k\boldsymbol{s} + \boldsymbol{\nabla}_{\boldsymbol{t}}\mu_k\boldsymbol{t} + \boldsymbol{\nabla}_{\boldsymbol{n}}\mu_k\boldsymbol{n}) && (1.49)\\ &\simeq \boldsymbol{\nabla}_{\boldsymbol{t}}\mu_k\boldsymbol{s} - \boldsymbol{\nabla}_{\boldsymbol{s}}\mu_k\boldsymbol{t}\ , \end{aligned}$$

noting the directional direvatives $\boldsymbol{\nabla}_{\boldsymbol{s}}\mu_k = \boldsymbol{\nabla}\mu_k \cdot \boldsymbol{s}$ *etc.*, and supposing for the last line the basis $(\boldsymbol{s}, \boldsymbol{n}, \boldsymbol{t})$ to be close enough to orthonormal. This shows that the vortical intensity $\boldsymbol{\Gamma}'_k$ has two components : one tangential $(\boldsymbol{t})$ and one perpendicular $(\boldsymbol{s})$ to the trailing edge in the direction of the emission plane.

The tangential component $\boldsymbol{\Gamma}'_k \cdot \boldsymbol{t}$ is determined using Equation (1.42) deduced from Bernoulli's relation. Given the definition of the direction $\boldsymbol{s} = \dfrac{\boldsymbol{u}^{\boldsymbol{\varphi}}_{\boldsymbol{m}}}{|\boldsymbol{u}^{\boldsymbol{\varphi}}_{\boldsymbol{m}}|}$ (via Equation (1.45)), this relation can be translated as :

$$\frac{\partial\mu_k}{\partial t} + |\boldsymbol{u}^{\boldsymbol{\varphi}}_{\boldsymbol{m}}|\boldsymbol{s} \cdot \boldsymbol{\nabla}\mu_k = 0\ , \tag{1.50}$$

i.e. :

$$\frac{\partial\mu_k}{\partial t} + |\boldsymbol{u}^{\boldsymbol{\varphi}}_{\boldsymbol{m}}|\boldsymbol{\nabla}_{\boldsymbol{s}}\mu_k = 0\ . \tag{1.51}$$

The tangential component is deduced from Equations (1.49) and (1.51) :

$$\begin{aligned} \boldsymbol{\Gamma}'_k \cdot \boldsymbol{t} &= -\boldsymbol{\nabla}_{\boldsymbol{s}}\mu_k \\ &= \frac{1}{|\boldsymbol{u}^{\boldsymbol{\varphi}}_{\boldsymbol{m}}|}\frac{\partial\mu_k}{\partial t}\ . && (1.52) \end{aligned}$$

The time derivative $\dfrac{\partial\mu_k}{\partial t}$ is estimated using the explicit Euler method :

$$\boldsymbol{\Gamma}'_k \cdot \boldsymbol{t} \simeq \frac{\mu_k(t) - \mu_k(t - dt)}{|\boldsymbol{u}^{\boldsymbol{\varphi}}_{\boldsymbol{m}}|dt}\ . \tag{1.53}$$

The perpendicular component $\boldsymbol{\Gamma}'_k \cdot \boldsymbol{s}$ is approximated by the finite difference scheme :

$$\begin{aligned} \boldsymbol{\Gamma}'_k \cdot \boldsymbol{s} &= \boldsymbol{\nabla}_{\boldsymbol{t}}\mu_k \\ &\simeq \frac{\mu_{k+1} - \mu_{k-1}}{2dl}\ , && (1.54) \end{aligned}$$

with μ_{k+1} and μ_{k-1} the dipole intensities associated to the neighboring faces $\mathscr{S}_{k+1}$ and $\mathscr{S}_{k-1}$ as shown in Figure 1.5. At the extremities of the turbine blade meshes, this scheme must be adapted to account for the fact that one of the neighboring faces $\mathscr{S}_{k+1}$ or $\mathscr{S}_{k-1}$ does not exist. What's more, a wide range of investigations beginning with those of Mansour [65] have shown that the intensity of the tip vortices released at the tip of an airfoil or turbine blade exceed by far those generated along its span. The tip vortical intensities are adjusted accordingly, by considering that if $\mathscr{S}_{k-1}$ does not exist :

$$\boldsymbol{\Gamma}'_k \cdot \boldsymbol{s} = \frac{\mu_k + \mu_{k+1}}{2dl} \ , \tag{1.55}$$

and if $\mathscr{S}_{k+1}$ does not exist :

$$\boldsymbol{\Gamma}'_k \cdot \boldsymbol{s} = -\frac{\mu_k + \mu_{k-1}}{2dl} \ . \tag{1.56}$$

Characteristics of the new particles

From the previous paragraphs, we can summarize the characteristics of the new fluid particles $\mathscr{P}'_k$ emitted behind each trailing edge mesh face $\mathscr{S}_k$.

— Central point, using the notations shown in Figure 1.5 :

$$\boldsymbol{x}'_k = \boldsymbol{m} + \frac{|\boldsymbol{u}^{\varphi}_{\boldsymbol{m}}|dt}{2}\boldsymbol{s} \ . \tag{1.57}$$

— Vortical weight, combining the results of Equations (1.48), (1.53) and (1.54) :

$$\begin{aligned} \boldsymbol{\Omega}'_k &= dh\, dl \left[\frac{\mu_k(t) - \mu_k(t-dt)}{|\boldsymbol{u}^{\varphi}_{\boldsymbol{m}}|dt}\boldsymbol{t} + \frac{\mu_{k+1} - \mu_{k-1}}{2dl}\boldsymbol{s} \right] \\ &= \left[\mu_k(t) - \mu_k(t-dt)\right] dl\, \boldsymbol{t} + \frac{\mu_{k+1} - \mu_{k-1}}{2}|\boldsymbol{u}^{\varphi}_{\boldsymbol{m}}|dt\, \boldsymbol{s} \ , \end{aligned} \tag{1.58}$$

unless $\mathscr{S}_k$ is a tip emission face :

$$\boldsymbol{\Omega}'_k = \begin{cases} \left[\mu_k(t) - \mu_k(t-dt)\right] dl\, \boldsymbol{t} + \dfrac{\mu_k + \mu_{k+1}}{2}|\boldsymbol{u}^{\varphi}_{\boldsymbol{m}}|dt\, \boldsymbol{s} & \text{if } \mathscr{S}_{k-1} \text{ does not exist,} \\ \left[\mu_k(t) - \mu_k(t-dt)\right] dl\, \boldsymbol{t} - \dfrac{\mu_k + \mu_{k-1}}{2}|\boldsymbol{u}^{\varphi}_{\boldsymbol{m}}|dt\, \boldsymbol{s} & \text{if } \mathscr{S}_{k+1} \text{ does not exist.} \end{cases} \tag{1.59}$$

— Particle volume :

$$\begin{aligned} V'_k &\simeq dh\, dl\, \epsilon \\ &\simeq |\boldsymbol{u}^{\varphi}_{\boldsymbol{m}}|dt\, dl\, \epsilon \ , \end{aligned} \tag{1.60}$$

with ϵ the regularisation parameter used in the computation of the desingularised Biot and Savart kernel of Equation (1.17). This regularisation parameter is used to assign a volume to the new particle by multiplying the area of its equivalent imaginary face $\mathscr{S}'_k$ by an elemental "near-zero" thickness.

Once the new particles ($\mathscr{P}'_k$) have been initialized with these properties, they are integrated into the set of fluid particles forming the wake of the turbine. As such, they will contribute to the rotational velocity component described in Paragraph 1.2.2, and be advected and evolve as will be seen later on.

Iterative process

However, the particle emission process is not as straightforward as surmising the new particles from the dipole distribution of the previous iteration and creating them immediately. The newly emitted particles will affect the residual velocity on the obstacle surface, as part of the set of particles used for the computation of the rotational velocity (1.23). This rotational velocity enters into the calculation of the right hand side vector $\boldsymbol{b}$ of Equation (1.38), thus affecting the linear system (1.36) from which the dipole intensities μ are deduced. These same dipole intensities are essential to the estimation of the new particle vortical weights as shown in Equations (1.58) and (1.59). This mutual dependency must be solved by an iterative process.

The iterative process for the emission of fluid particles is named "sub-iterations" as it must be realised at each time step of the simulation. The steps involved in the sub-iterations are summarised in the diagram of Figure 1.6. The three initialisation steps indicate the computation of terms which will not be modified in the iterative process. For instance, the emission velocity for a new particle $\mathscr{P}'_k$:

$$\boldsymbol{u}^{\varphi}_{\boldsymbol{m}k} = \boldsymbol{u}_{\infty} - \boldsymbol{u}_B(\boldsymbol{m}_k) + \boldsymbol{u}^{\psi}(\boldsymbol{m}_k) + \boldsymbol{u}^{\varphi}(\boldsymbol{m}_k) \tag{1.61}$$

is initialised by adjusting the constant upstream velocity $\boldsymbol{u}_{\infty}$ with the body velocity $\boldsymbol{u}_B(\boldsymbol{m}_k)$, and adding the rotational velocity $\boldsymbol{u}^{\psi}(\boldsymbol{m}_k)$ generated by the particles already present in the wake (*i. e.* all fluid particles except for those currently being emitted). None of these components will be modified by the iterative process. When updating the emission velocity in the course of the sub-iterations, the variable components can then be added in : namely the potential velocity $\boldsymbol{u}^{\varphi}(\boldsymbol{m}_k)$ generated by the dipole distribution and the missing part of the rotational velocity $\boldsymbol{u}^{\psi}(\boldsymbol{m}_k)$ generated particles currently being emitted. The same principle is applied to the characteristics of the new particles and the right hand side vector $\boldsymbol{b}$, for which a constant part can also be previously computed.

Moreover instead of solving the linear system $\boldsymbol{A\mu} = \boldsymbol{b}$ (see Equation (1.36)), we solve instead for a correction :

$$\boldsymbol{A\mu}_{\text{corr}}{}^{(p)} = \boldsymbol{b}_{\text{corr}}{}^{(p)} \ . \tag{1.62}$$

This system is updated at each sub-iteration p of the emission process. In order to ensure the convergence of this process, a convergence criterium is computed at each sub-iteration p, evaluating the gain from the previous solution $\boldsymbol{\mu}^{(p-1)}$ to the current solution $\boldsymbol{\mu}^{(p)}$. The sub-iteration process is halted once this convergence criterium reaches a target value ξ specified is a parameter of the simulation :

$$||\boldsymbol{\mu}^{(p)} - \boldsymbol{\mu}^{(p-1)}||_{\infty} < \xi \ , \tag{1.63}$$

signifying that the convergence is considered to be satisfactory.

1.3 Numerical treatment of the Navier-Stokes equations

This paragraph will focus on the evaluation of the particle derivative $\frac{D\omega}{Dt}$ as defined by Equation (1.5), essential to the resolution of the Navier-Stokes Equations (1.4). This term describes the evolution of the vortical weights $\boldsymbol{\Omega}_i$ of the fluid particles used in the Vortex method. In order to simplify notations, we will consider in this section a vortical flow free of any obstacle, meaning that the velocity $\boldsymbol{u}$ can be reduced to the sole components :

$$\boldsymbol{u} = \boldsymbol{u}^{\psi} + \boldsymbol{u}_{\infty} \ . \tag{1.64}$$

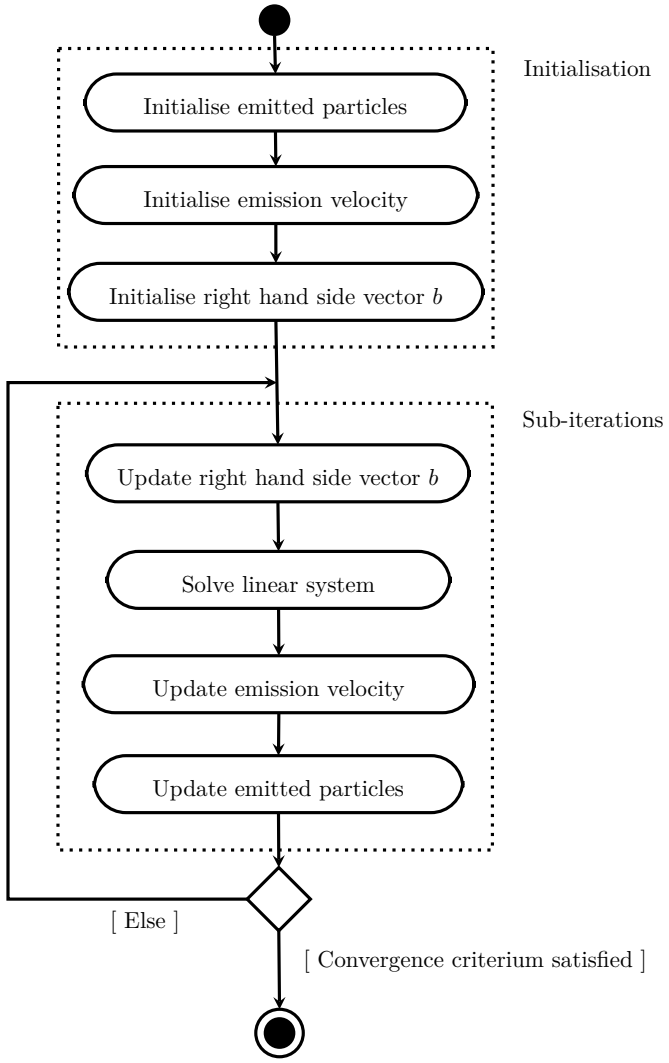

Figure *1.6:* *Flowchart representing the steps of the sub-iteration process for the emission of fluid particles at the trailing edges of the obstacle surface meshes.*

As a reminder, the Navier-Stokes Equations in their velocity-vorticity formulation (1.4) yield the expression :

$$\frac{D\boldsymbol{\omega}}{Dt} = \underbrace{(\boldsymbol{\omega}\cdot\boldsymbol{\nabla})\boldsymbol{u}}_{\text{Stretching term } \boldsymbol{S}} + \underbrace{\nu\Delta\boldsymbol{\omega}}_{\text{Diffusion term } \boldsymbol{L}} , \tag{1.65}$$

which can be broken into a stretching term $\boldsymbol{S}$ and a diffusion term $\boldsymbol{L}$.

1.3.1 Treatment of the stretching term

The Stretching term $\boldsymbol{S}$ of the previous decomposition of Equation (1.65) can be written as :

$$\begin{aligned} \boldsymbol{S} &= (\boldsymbol{\omega}\cdot\boldsymbol{\nabla})\,\boldsymbol{u} \\ &= \boldsymbol{\omega}\cdot(\boldsymbol{\nabla}\otimes\boldsymbol{u}) \\ &= \boldsymbol{\omega}\cdot\overline{\overline{\boldsymbol{J}}}_{\boldsymbol{u}}^{T} , \end{aligned} \tag{1.66}$$

where $\overline{\overline{\boldsymbol{J}}}_{\boldsymbol{u}}^{T}$ is the transpose of the Jacobian matrix $\overline{\overline{\boldsymbol{J}}}_{\boldsymbol{u}}$ calculated from the velocity $\boldsymbol{u}$:

$$\left(\overline{\overline{\boldsymbol{J}}}_{\boldsymbol{u}}\right)_{ij} = \left(\frac{\partial u_j}{\partial x_i}\right) . \tag{1.67}$$

Therefore each component $i = 1, 2, 3$ of the stretching term $\boldsymbol{S}$ can be expressed as the following :

$$S_i = \sum_{j=1}^{3} \omega_j \frac{\partial u_i}{\partial x_j} . \tag{1.68}$$

This stretching term $\boldsymbol{S}$ can also be expressed using two other equivalent formulations to the expression of Equation (1.68), leading to different discretised expressions (see [60, 63, 66, 67]).

Within this framework, the flow is assumed to have no obstacles and the upstream velocity is a uniform value :

$$\overline{\overline{\boldsymbol{J}}}_{\boldsymbol{u}} = \overline{\overline{\boldsymbol{J}}}_{\boldsymbol{u}^{\psi}} . \tag{1.69}$$

The stretching term $\boldsymbol{S}$ can now be rewritten using the continuous expression for the rotational velocity $\boldsymbol{u}^{\psi}$ of Equation (1.15) :

$$\begin{aligned} \boldsymbol{S}(\boldsymbol{x}) &= \sum_{j=1}^{3} \omega_j(\boldsymbol{x}) \frac{\partial \boldsymbol{u}^{\psi}(\boldsymbol{x})}{\partial x_j} \\ &= \omega_j(\boldsymbol{x}) \frac{\partial}{\partial x_j} \left(\int_{\boldsymbol{y}\in\mathbb{R}^3} \boldsymbol{K}(\boldsymbol{x},\boldsymbol{y}) \times \boldsymbol{\omega}(\boldsymbol{y}) dy \right) \\ &= \int_{\boldsymbol{y}\in\mathbb{R}^3} \left[\sum_{j=1}^{3} \left(\omega_j(\boldsymbol{x}) \frac{\partial}{\partial x_j} \boldsymbol{K}(\boldsymbol{x},\boldsymbol{y}) \right) \right] \times \boldsymbol{\omega}(\boldsymbol{y}) dy . \end{aligned} \tag{1.70}$$

This expression has a singularity issue around $\boldsymbol{x} = 0$ due to the Biot and Savart kerlenl $\boldsymbol{K}$. Therefore it is once again necessary to use a desingularised version $\boldsymbol{K}_{\epsilon}$ instead, as prescribed previously in Section 1.2.2. We obtain the desingularised expression :

$$\boldsymbol{S}_{\epsilon}(\boldsymbol{x}) = \int_{\boldsymbol{y}\in\mathbb{R}^3} \left[\sum_{j=1}^{3} \left(\omega_j(\boldsymbol{x}) \frac{\partial}{\partial x_j} \boldsymbol{K}_{\epsilon}(\boldsymbol{x},\boldsymbol{y}) \right) \right] \times \boldsymbol{\omega}(\boldsymbol{y}) dy . \tag{1.71}$$

The partial derivatives of the Moore-Rosenhead version of the desingularised kernel $\boldsymbol{K}_\epsilon$ are derived in Mycek's thesis [8] :

$$\begin{aligned}\boldsymbol{S}_\epsilon(\boldsymbol{x}) = \int_{\boldsymbol{y}\in\mathbb{R}^3} \chi_\epsilon(\boldsymbol{x},\boldsymbol{y})\left[(\boldsymbol{y}-\boldsymbol{x})\cdot\boldsymbol{\omega}(\boldsymbol{y})\right]\left[(\boldsymbol{y}-\boldsymbol{x})\times\boldsymbol{\omega}(\boldsymbol{y})\right] \\ + \frac{q_\epsilon(\boldsymbol{x},\boldsymbol{y}}{|\boldsymbol{y}-\boldsymbol{x}|^3}(\boldsymbol{\omega}(\boldsymbol{y})\times\boldsymbol{\omega}(\boldsymbol{x}))dy\ ,\end{aligned} \tag{1.72}$$

with $\chi_\epsilon(\boldsymbol{x})$ and $q_\epsilon(\boldsymbol{x})/|\boldsymbol{x}|^3$ defined as :

$$\begin{cases}\chi_\epsilon(\boldsymbol{x}) = \dfrac{3}{4\pi}\dfrac{1}{(|\boldsymbol{x}|^2+\epsilon^2)^{5/2}} & \text{(1.73a)}\\ q_\epsilon(\boldsymbol{x})/|\boldsymbol{x}|^3 = \dfrac{1}{4\pi}\dfrac{1}{(|\boldsymbol{x}|^2+\epsilon^2)^{3/2}}, & \text{(1.73b)}\end{cases}$$

The stretching field $\boldsymbol{S}_\epsilon$ acting on all N fulid particles $\mathscr{P}_i$ of center points $\boldsymbol{x_i}$, vortical weights $\boldsymbol{\Omega}_i$, and volumes V_i, can be discretized as :

$$\int_{\mathscr{P}_i} \boldsymbol{S}_\epsilon(\boldsymbol{x})dx \simeq \boldsymbol{S}_{\epsilon,i}V_i\ , \tag{1.74}$$

with :

$$\begin{aligned}\boldsymbol{S}_{\epsilon,i}V_i = \sum_{j=1}^{N}\chi_\epsilon(\boldsymbol{x}_j,\boldsymbol{x}_i)\left[(\boldsymbol{x}_i-\boldsymbol{x}_j)\cdot\boldsymbol{\Omega}_i\right]\left[(\boldsymbol{x}_i-\boldsymbol{x}_j)\times\boldsymbol{\Omega}_j\right] \\ + \frac{q_\epsilon(\boldsymbol{x}_j,\boldsymbol{x}_i)}{|\boldsymbol{x}_i-\boldsymbol{x}_j|^3}(\boldsymbol{\Omega}_j\times\boldsymbol{\Omega}_i)\ .\end{aligned} \tag{1.75}$$

1.3.2 Treatment of diffusion

The Diffusion term $\boldsymbol{L} = \nu\Delta\boldsymbol{\omega}$ from Equation (1.65) can also be discretized on each of the N fluid particles $\mathscr{P}_i$ of central point $\boldsymbol{x}_i$, vortical weight $\boldsymbol{\Omega}_i$ and volume V_i :

$$\begin{aligned}\int_{\mathscr{P}_i}\boldsymbol{L}(\boldsymbol{x})dx &\simeq \nu[\Delta\boldsymbol{\omega}]_{\boldsymbol{x}_i}V_i \\ &= \boldsymbol{L}_iV_i\ .\end{aligned} \tag{1.76}$$

When considering a viscous fluid with a constant viscosity ν, the molecular diffusion term $\boldsymbol{L}_iV_i$ can be treated using the Particle Strength Exchange method initially developed by Degond and Mas-Gallic [68] and Choquin and Huberson [69]. This method provides the approximation :

$$\boldsymbol{L}_iV_i = \nu[\Delta\boldsymbol{\omega}]_{\boldsymbol{x}=\boldsymbol{x}_i}V_i \simeq \nu\sum_{j=1}^{N}\left[\boldsymbol{\Omega}_jV_i - \boldsymbol{\Omega}_iV_j\right]\eta_\epsilon^{\text{lap}}\left(\boldsymbol{x}_i-\boldsymbol{x}_j\right), \tag{1.77}$$

where $\eta_\epsilon^{\text{lap}}$ is a regularised kernel built in order to approximate the three dimensional Laplacian operator. In the present study, $\eta_\epsilon^{\text{lap}}$ is defined as :

$$\eta_\epsilon^{\text{lap}}(\boldsymbol{x}) = \frac{1}{\epsilon^3}\eta^{\text{lap}}\left(\frac{\boldsymbol{x}}{\epsilon}\right), \tag{1.78}$$

with η^{lap} a second order Gaussian kernel :

$$\eta^{\text{lap}}(\boldsymbol{x}) = \frac{4}{\epsilon^2 \pi^{3/2}} \exp\left(-|\boldsymbol{x}|^2\right). \tag{1.79}$$

When developing a method to account for ambient turbulence in the surrounding flow, it becomes all the more important to account for turbulent diffusion among the Vortex particles. This is accomplished via the use of a Large Eddy Simulation model, in order to represent the influence of the non-resolved length scales. LES models are based on the definition of an eddy viscosity ν_T, which is usually not constant. The diffusion term $\boldsymbol{L}_i V_i$ of Equation (1.77) becomes :

$$\boldsymbol{L}_i V_i = \left[(\nu + \nu_T)\,\Delta\boldsymbol{\omega} + (\boldsymbol{\nabla}\nu_T) \wedge (\Delta\boldsymbol{u})\right]_{\boldsymbol{x}=\boldsymbol{x}_i} V_i. \tag{1.80}$$

Several expressions exist for the eddy viscosity ν_T, among which can be cited those of Smagorinsky (as described by Sagaut [70]), Mansfield *et al.* [71, 72], and Mansour [73]. Sagaut [70] has assembled a synthetic analysis of these various formulations. In the present study, the turbulent eddy viscosity is computed as defined by Mansour [73] :

$$\nu_T = (C_M \Delta)^2 \sqrt{2} |\boldsymbol{\omega}|, \tag{1.81}$$

where C_M is a constant to be fixed (in the present case at $C_M = 0.2$), and Δ is the average distance between particles. Thus, the turbulent eddy viscosity $\nu_{T,i}$ of for the i^{th}-particle can be expressed as :

$$\nu_{T,i} = \nu_T(\boldsymbol{x}_i) \simeq (C_M \Delta)^2 \sqrt{2} \frac{|\boldsymbol{\Omega}_i|}{V_i}. \tag{1.82}$$

An alternative numerical approach for diffusion is possible in the Lagrangian Vortex framework : the Diffusion Velocity Method (DVM), initially proposed by Ogami and Akamatsu [74] and recently analysed by Mycek *et al.* [75]. This last study also offers some perspective on the three-dimensional treatment of diffusion with LES using a DVM approach.

1.3.3 Numerical scheme and optimisations

The computations presented here are run using a second order Runge-Kutta time stepping scheme, although fourth order and simple Euler versions also exist within the software. A remeshing of the fluid particles onto a cartesian grid is carried out at regular intervals throughout the simulation in order to preserve inter-particle distance. In order to speed up the calculation of particle interactions by the Biot and Savart kernel, a Tree-code algorithm based on the version of Lindsay and Krasny [76] is used. This "divide and conquer" type algorithm is highly dependant on the strategy used for dividing and grouping particles, which was until recently purely geometrical. However profilings of the Dorothy software have shown higher efficiencies when using a K-means clustering [77] approach instead. Paul Mycek's thesis [8] provides more detailed descriptions of these numerical considerations.

One last significant optimization recently adopted within the software lies in the progressive dissipation of the fluid wake after a set distance. Careful studies have shown for instance that introducing such a dissipation as of 12.5 diameters downstream of a turbine has no significant impact on the first 10 diameter area of its wake typically used for comparison with experimental results. Naturally this distance must be extended when considering multi-turbine configurations requiring wake interactions. Limiting the number of fluid particles by discarding the ever extending and less physically relevant end of the

wake in this way allows for substantial gains in simulation time. This process is described in the thesis of Clément Carlier [9], although not yet widely used for most of his simulations.

Between this shortening of the wakes, the adoption of the K-means rather than geometrical clustering for the treecode speed-up algorithm, and various optimizations and reorganisations of the code carried out in the contexts of hackathons and profiling sessions, the average simulation runtime of the Dorothy code has been considerably decreased.

1.4 Simulation of tidal turbines

This Section will showcase numerical results obtained for a single turbine in basic inflow conditions, i.e. without the contribution of ambient turbulence which will be presented later on. These preliminary results aim to demonstrate and validate the outcome of the Vortex Particle Method described in this Chapter, by comparison with experimental flume tank measurements. The experimental results presented hereafter were gathered at the IFREMER flume tank in Boulogne-sur-Mer, and presented already in various publications [18, 78, 79].

1.4.1 Configuration

Scaling parameters

These experiments were carried out using a scaled turbine model, sized by the combination of Froude scaling with the Tip Speed Ratio (TSR) intended for the full size turbine. The Tip Speed Ratio is defined as :

$$\mathrm{TSR} = \frac{|\boldsymbol{\phi}|R}{|\boldsymbol{u}_\infty|}, \tag{1.83}$$

with $\boldsymbol{\phi}$ the rotational speed of the turbine, R its radius and $\boldsymbol{u}_\infty$ the upstream velocity. The Froude number is defined as :

$$Fr_\infty = \frac{|\boldsymbol{u}_\infty|}{\sqrt{gH}}, \tag{1.84}$$

with H being the water depth and $g = 9.81\mathrm{m.s}^{-2}$ the gravitational acceleration. Using the Froude scaling, a $1:\lambda$ applied to the turbine radius R or the water depth H with respect to full scale imposes a scaling factor of $\sqrt{\lambda}$ applied to the upstream velocity $\boldsymbol{u}_\infty$. Similarly, a scaling of $1:\lambda^{-1/2}$ applies to the rotational velocity Φ_x to both comply with the Froude scaling and TSR. A Reynolds Re_∞ can also be defined based on the turbine radius R such as :

$$Re_\infty = \frac{|\boldsymbol{u}_\infty|R}{\nu}, \tag{1.85}$$

with $\boldsymbol{u}_\infty$ still being the upstream velocity and ν the kinematic viscosity of water. Re_∞ is reduced by a factor of $\lambda\sqrt{\lambda}$ at the laboratory scale. Due to the size of the test section $2\,m \times 4\,m$ (cf. Figure 1.7) and in order to avoid too high a blockage ratio, the turbine radius was fixed at $R = 0.35\,m$. Therefore, at laboratory scale, the tidal turbine is defined with a ratio of $1:25$ with respect to the full scale. The different scaling ratios, model and prototype scales are summarised in the following Table 1.1.

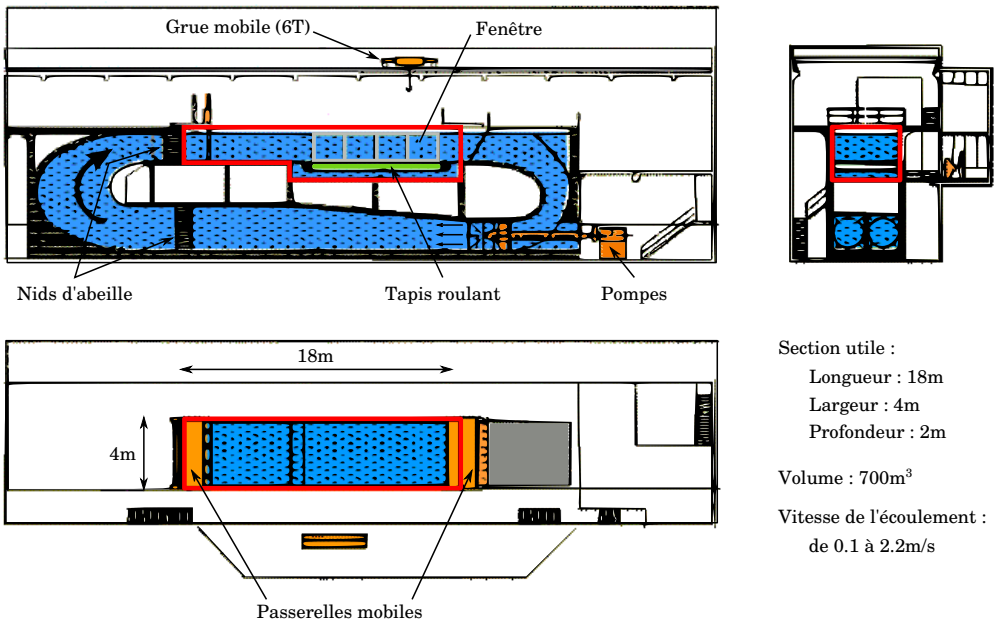

Figure 1.7: *Schematic representation of the IFREMER flume tank located in Boulogne-sur-Mer, France.*

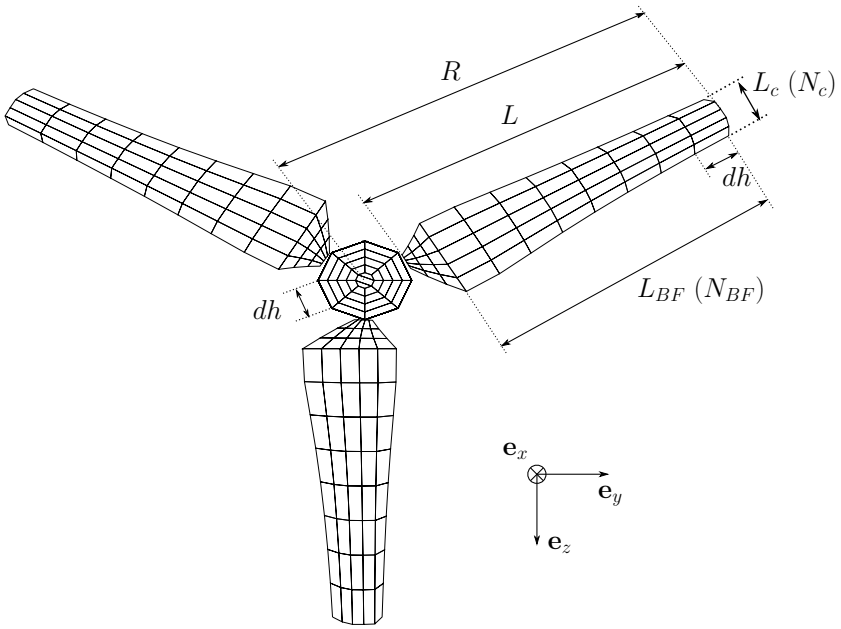

Figure 1.8: *Definition of the different variables characterising a turbine mesh.*

Variables	Scale 1	Scale 1 : 25	Ratio	Scaling
Radius R	8.75m	0.35m	$1:\lambda$	
Water depth H	50m	2m	$1:\lambda$	
Upstream velocity $\boldsymbol{u}_\infty$	4m.s^{-1}	0.8m.s^{-1}	$1:\sqrt{\lambda}$	$Fr_\infty \approx 0.18$
Rotational velocity Ω_x	16tr/min	80tr/min	$1:\lambda^{-1/2}$	TSR ≈ 3.67
Reynolds Re_∞	$\approx 3.5\times10^7$	$\approx 2.8\times10^5$	$1:\lambda\sqrt{\lambda}$	

Table *1.1:* *Correspondence between the length scales of the* $1:25$ *scaled model and the full scale prototype.*

Identifier	N_c	N_{BF}	N_c^{hub}	N_{BF}^{hub}	N_p	dh	ϵ
05x05	5	5	58	6	488	0.158	0.236
05x07	5	7	58	8	641	0.113	0.169
05x11	5	11	58	12	964	0.072	0.107
05x15	5	15	58	16	1278	0.053	0.079
05x23	5	23	58	24	1914	0.034	0.051

Table *1.2:* *Description of the different meshes used to compute tidal turbines.*

Turbine model

In Lagrangian Vortex computations, tidal turbines are represented by a surface as depicted in Figures 1.2 and 1.8. The geometry of the meshes used here was based on that of IFREMER's exeperimental tidal turbine model [18,22,63,78,80], as was precisely defined first in [18] and more recently in [80]. Several turbine meshes are presented in Table 1.2 and the meshes used will usually be designated by there number of chord and trailing edge elements $N_C \times N_{BF}$ ("BF" for the french "Bord de Fuite"), as shown in Figure 1.8.

The numerical parameters dh and ϵ of Table 1.2 denote respectively the characteristic mesh length, which also corresponds to the characteristic inter-particle spacing, and the smoothing paramater used to desingularise the Biot & Savart kernel $\boldsymbol{K}$ (see Equation (1.17)). These two variables dh and ϵ are related with the overlapping paramater $\kappa > 1$, most commonly chosen as 1.5 :

$$\kappa = \frac{\epsilon}{dh} = 1.5. \tag{1.86}$$

The two following paragraphs will deal with wake computations and performance assessment respectively. In order to showcase the starting point and motivations for the further developments covered in the following Chapters, the results presented here are those produced by the simulation code at the very start of this work, in the context of a preliminary internship. For the wake, these preliminary results do not take into account any ambient turbulence, this aspect being the major focus of the second part of this PhD work. As for the performance assessment, after a presentation of the existing method, its drawbacks will be highlighted as an introduction to the following Chapter 2 dedicated to an alternative approach to account for the full three-dimensional geometry of the turbine blades.

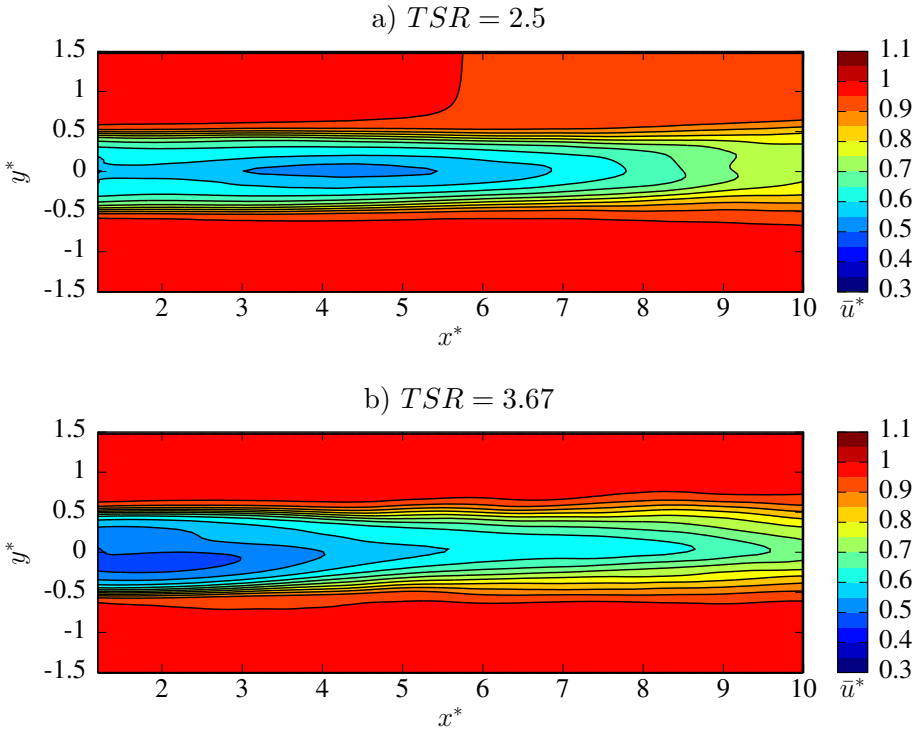

Figure *1.9:* *Simulated wake downstream of a single turbine, with an upstream velocity of $\boldsymbol{u}_\infty$ and rotational speeds corresponding to TSRs of 2.5 and 3.67.*

1.4.2 Turbine wake simulation

Apart from the tidal site scaled results shown in the last two Chapters of this manuscript, all simulations are habitually run dimensionless. This implies an incoming upstream velocity of $\boldsymbol{u}_\infty = (1, 0, 0)$ compared to the value of $\boldsymbol{u}_\infty = (0.8, 0, 0)$ most frequently used in the experiments, and $R = 1$ compared to the radius $R = 0.35$ of the scaled model. Only the kinematic viscosity ν is adjusted so as to obtain a Reynolds number representative of the IFREMER flume tank conditions. A more detailed description of the experimental set-up is presented in Mycek *et al.* [63, 78] and more recently in Gaurier *et al.* [80] for the latest revisions. The values of TSR chosen for the wake maps of Figure 1.9 are those most commonly tested at IFREMER. Three possible ambient turbulence intensities can be generated in the flume tank, ranging from $I_\infty = 1.5\%$ to $I_\infty = 15\%$. This ambient turbulence could not be taken into account in the simulations before the PhD work of Clément Carlier, at the end of which only the lowest ambient turbulent levels could be simulated without too much strain on the software capabilities [9]. From the wake velocity maps shown in Figure 1.9, the velocity deficits are important and obviously too high if compared with experimental tendencies. These aspects will largely be covered in the second part of this manuscript, with the continuation of this work on the incorporation of ambient turbulence generation in this Lagrangian context.

1.4.3 Performance results

Force computation method

Tidal turbine performances are characterised by a power coefficient C_P and a thrust coefficient C_T, defined as :

$$C_P = \frac{\mathcal{M}_x \phi_x}{\frac{1}{2}\rho\pi R^2 |\boldsymbol{u}_\infty|^3}, \tag{1.87}$$

$$C_T = \frac{\mathcal{F}_x}{\frac{1}{2}\rho\pi R^2 |\boldsymbol{u}_\infty|^2}, \tag{1.88}$$

with $\mathcal{M}_x$ being the torque along the x-axis (aligned with the incoming upstream velocity direction), $R = D/2$ the turbine radius, ϕ_x its rotational speed, ρ the fluid density and $\mathcal{F}_x$ the axial force applied to the whole tidal turbine. Prior to compute these two coefficients, it is necessary to evaluate the normal force $\boldsymbol{\mathcal{F}}_n$ applied to the turbine surfaces. Initially in the simulation code, following the work from Pinon *et al.* [18] inspired themselves form [55], the total normal force $\boldsymbol{\mathcal{F}_n}$ applied to a lifting surface $\mathscr{S}$ was calculated as :

$$\boldsymbol{\mathcal{F}}_n = \rho \int_{\boldsymbol{y}\in\mathscr{S}} \frac{\partial \mu(\boldsymbol{y})}{\partial t} \boldsymbol{n}(\boldsymbol{y}) dy + \rho \int_{\boldsymbol{y}\in\mathscr{S}} \boldsymbol{u}(\boldsymbol{y}) \times \boldsymbol{\gamma}(\boldsymbol{y}) dy + 2\rho \int_{\boldsymbol{y}\in\mathscr{S}} \boldsymbol{\phi} \times \boldsymbol{u}(\boldsymbol{y}) dy \ , \tag{1.89}$$

where $\boldsymbol{\gamma}$ is the vortex sheet attached to the surface $\mathscr{S}$ and the last term $2\rho \int_{\boldsymbol{y}\in\mathscr{S}} \boldsymbol{\phi}\times\boldsymbol{u}(\boldsymbol{y})dy$ is related to the pseudo-Coriolis force. Numerically speaking, the lifting surface $\mathscr{S}$ is decomposed into N_p surface elements $\mathscr{S}_p$ as depicted in Figure 1.8. Therefore, the total normal force $\boldsymbol{\mathcal{F}_n}$ applied to the tidal turbine can be computed as the sum of the elementary normal forces $\boldsymbol{f}_p$ acting on each surface elements $\mathscr{S}_p$:

$$\boldsymbol{\mathcal{F}}_n = \sum_{p=1}^{N_p} \boldsymbol{f}_p \tag{1.90}$$

with :

$$\boldsymbol{f}_p = \rho \int_{\boldsymbol{u}\in\mathscr{S}_p} \frac{\partial \mu(\boldsymbol{y})}{\partial t} \boldsymbol{n}(\boldsymbol{y}) dy + \rho \int_{\boldsymbol{y}\in\mathscr{S}_p} \boldsymbol{u}(\boldsymbol{y}) \times \boldsymbol{\gamma}(\boldsymbol{y}) dy + 2\rho \int_{\boldsymbol{y}\in\mathscr{S}_p} \boldsymbol{\phi} \times \boldsymbol{u}(\boldsymbol{y}) dy \ . \tag{1.91}$$

Normal forces $\boldsymbol{f}_p$ are then approximated by a mid-point quadrature :

$$\boldsymbol{f}_p \simeq \rho \left(\frac{\partial \mu}{\partial t}\right)_p \boldsymbol{n}_p \mathcal{A}_p + \rho \sum_{k=0}^{3} \boldsymbol{u}(\boldsymbol{L}_p^k) \times \boldsymbol{\mu}_p^k + 2\rho\boldsymbol{\phi} \times \boldsymbol{u}(\boldsymbol{x}_p)\mathcal{A}_p \ , \tag{1.92}$$

with $\boldsymbol{n}_p$ the normal vector of any surface element $\mathscr{S}_p$, $\mathcal{A}_p$ its area, $\boldsymbol{x}_p$ its centre, l_p^k the length of each segment vector $\boldsymbol{l}_p^k$ and $\boldsymbol{L}_p^k$ their centres. $\boldsymbol{\mu}_p^k$ is vortex attached to each segment l_p^k, given by :

$$\boldsymbol{\mu}_p^k = \begin{cases} \dfrac{\mathcal{A}_p}{\mathcal{A}_p + \mathcal{A}_p^{t,k}} \left(\mu_p - \mu_p^{t,k}\right) \boldsymbol{l}_p^k & \text{if } l_p^k \text{ has another adjancent surface element } \mathscr{S}_p^{t,k} \\ \mu_p \boldsymbol{l}_p^k & \text{otherwise.} \end{cases} \tag{1.93}$$

The last step to obtain the total normal force $\boldsymbol{\mathcal{F}_n}$ of the tidal turbine is to evaluate the temporal derivative of μ. This is done once again using a simple Euler numerical scheme :

$$\left(\frac{\partial \mu}{\partial t}\right)_p \simeq \frac{\mu_p(t) - \mu_p(t - dt)}{dt} \ . \tag{1.94}$$

Finally, the total torque $\boldsymbol{\mathcal{M}}_O$ computed at the centre of rotation $\boldsymbol{O}$ with respect to the turbine rotational axis is given by :

$$\boldsymbol{\mathcal{M}}_O = \sum_{p=1}^{N_p} \boldsymbol{OC_p} \times \boldsymbol{f}_p \,, \tag{1.95}$$

with C_p the centre face point of coordinate $\boldsymbol{x}_p$.

Numerical results

An example of this computed power coefficient is presented in Figure 1.10. A fairly good agreement with the experimental results is obtained for the lower part the TSR curve. Then from the experimental maximal C_P value on, the numerical power curve contirnues on its upwards trend, which is obviously incorrect. This outcome is surprising, as the numerical results correlate well with the experimental data for the lowest portion of TSR values, where the turbine blade should be affected by stall. However the occurrence of stall is not modelled and cannot be accounted for in this initial approach. Then, from the maximum C_P value at approximately TSR = 3.9 on, the flow is expected to be attached and adapted over most of the blade span. For higher values of TSR representing the over-speed region, some blade sections will start to move away from their optimal working point. At the blade section level, this would mean locally a lower angle of attack which should be accurately locally modelled but the present numerical approach. This is obviously not the case here based on the results shown in Figure 1.10. An alternative calculation was carried out without taking into account for the pseudo-Coriolis force $2\rho \int_{\boldsymbol{y}\in\mathscr{S}} \boldsymbol{\phi}\times\boldsymbol{u}(\boldsymbol{y})dy$ as included in Equation 1.89. As expected, the large overestimation and eventual divergence of the C_P values for TSR values higher than 3 is no longer visible. This could be considered as an optimistic and promising tendency, if the power curve was not still so far distant from the expected result in the over-speed region of TSR.

This issue was already evidenced to some extent in the previous work of Pinon *et al.* [18], Mycek [8], and Carlier [9], although no satisfying solution could be found when still considering an infinitely thin blade. For instance, difficulties were already encountered for the computation of accurate forces in [44] using a two-dimensional infinitely thin plate, even though it had been previously established that this method could give accurate results for a lifting flat plate at low angles of attack.

1.5 Conclusion

Within this context, one of the aims of this PhD work was to move on to a full three-dimensional representation of the turbine blades. Three-dimensional portrayals of turbines are widely and commonly used together with vortex sheet representations of the flow, but to our knowledge, never applied to the Vortex Blob representation. The following Chapter 2 will present the progress achieved towards the goal of taking into account full three-dimensional blades with the Vortex Blob representation of the flow.

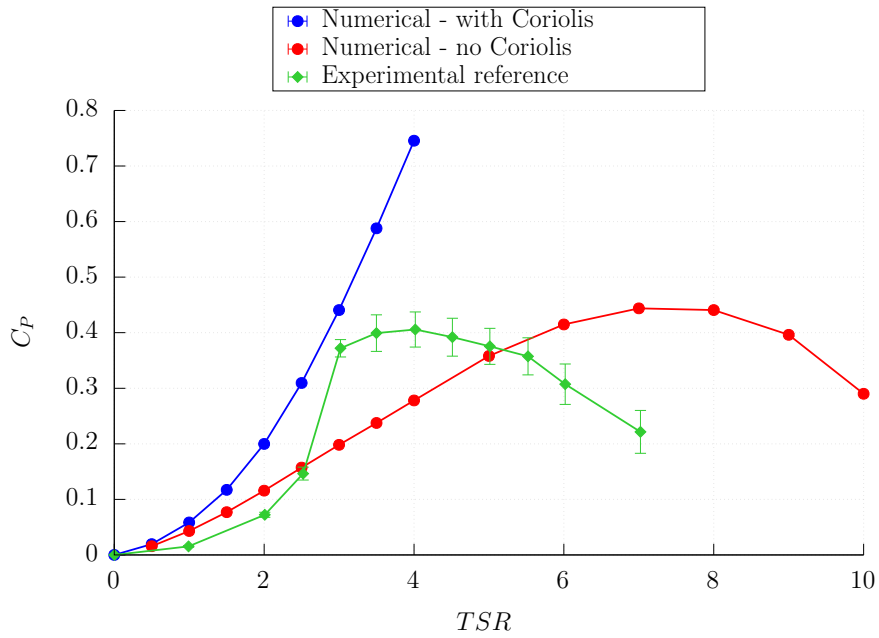

Figure *1.10:* *Current power curve of the IFREMER turbine computed using two different versions of the current Dorothy software power calculation, compared to flume tank experimental data provided by IFREMER.*

Chapter 2

Alternative decomposition adapted to a non zero thickness mesh

2.1 Introduction

The results presented in Section 1.4 have shown that the method described in the previous Chapter and currently in use in the Dorothy software yields goods results in terms of turbine wake configuration, but show some issues in terms of the simulated power curves. However it must be taken under consideration that these results are obtained using a simplified zero thickness representation of the turbine geometry. In order to improve upon the current computation of efforts, while also allowing for a generally more detailed and realistic rendering of the turbine blades, we will describe in this Chapter the formulation of an alternative method applicable to a fully three-dimensional non-zero thickness mesh.

This transition from a zero-thickness to a fully rendered mesh of the turbine blades entails first of all a revision of the singularity method to include a second type of singularity of the source type, in addition to the dipole type already present. The combination of source and dipole singularities for the representation of turbines meshes is fairly common among the literature. For instance, Riziotis and Voustinas use both sources and dipoles computed on turbine blade sections in the elaboration of their dynamic stall model [81]. Many more, such as Salvatore and Greco *et al.*, use a combination of sources and dipoles for fully potential turbine simulation codes [82–84].

Section 2.2 will describe the manner of combining source and dipole singularities considered in the scope of this work. This method can be derived directly from the Euler Equations, just as the dipole-only version considered in the previous Chapter. The mathematical derivation of this formulation is taken from the work of Morino [85].

Once the integral method for taking into account the full turbine blades has been formulated, the emission of fluid particles at the trailing edges of the lifting body meshes remains to be adjusted. The emission method must now take into account not one but two

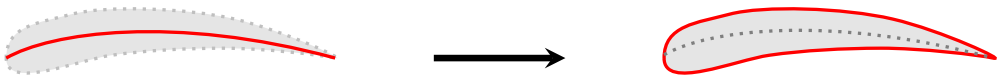

Figure *2.1: Reverting from the simplified mean camber zero-thickness surface representation of turbibe blades to a three-dimensional full-thickness rendition.*

mesh faces connected to each trailing edge segment, from the intrados and extrados sides of the blade mesh. This adaptation can be derived quite naturally based on the emission model already formulated for the zero thickness mesh, as will be described in Section 2.3.

These elements combined with the fluid model described in the previous Chapter provide a functioning framework for the simulation of the generation and evolution of the wake of fully rendered turbines. However, in this updated framework the method described in Section 1.4 for the computation of efforts is no longer relevant, as the dipoles are no longer the only type of singularity used on the mesh. Given that this method additionally did not provide satisfying results, the choice was made to revise it altogether rather than attempting to adapt it.

As an alternative, we have chosen a computation of efforts based on Bernoulli's relation providing localised pressure based on the velocity potential. This method is widely used in potential simulation codes, and is known to provide good results outside of the occurrence of stall [13, 83]. While this method appears in itself way more straightforward than the previous formulation, it does require the knowledge of the velocity potential on the mesh. In order to obtain this potential, rather than attempting to derive the potential contributions of each velocity component, we use a simple spacial integration formulated by Ogami [86]. Ogami's formulation allows for the computation of velocity potential based solely on the value of the complete velocity on the mesh, as will be shown in Section 2.4.

The aim of the formulation and combination of these elements was to obtain a reliable method for the simulation of the full-thickness realistic geometry of turbine blades. Unfortunately due to the hurdles of implementing new frameworks in an intricate simulation code, we have not yet been able to obtain the envisioned pressure coefficients and wake evolution. However the methods themselves remain of considerable interest, which is why this Chapter will focus on their description and preliminary validations. We hope in the near future to be able to demonstrate their full effectiveness.

2.2 Velocity formulation

This Section describes the new velocity decomposition proposed for the computation of a turbine and its wake. While it is similar to the decomposition currently used in the simulation code presented in Section 1.2, it incorporates one additional term accounting for a new source singularity distribution on the solid body mesh.

This alternative velocity decomposition including the new contribution will be approached differently to the previous Chapter. Rather than describing the resolution of each velocity term (potential and rotational) in isolation, we have chosen to begin by retracing the mathematical derivation of this velocity formulation in its entirety, based on the work of Morino [85]. This will not only prove its validity, but also justify specifically the choice of source and dipole singularity intensities, which does not always appear very clearly in most recent literature.

2.2.1 Helmholtz and integral decomposition

We begin once again from the Helmhotlz decomposition of the velocity presented in Paragraph 1.2.1 :

$$\boldsymbol{u} = \boldsymbol{\nabla}\varphi + \boldsymbol{\nabla}\times\boldsymbol{\psi} + \boldsymbol{u_\infty} \,, \tag{2.1}$$

where :

$$\boldsymbol{\nabla}^2\,\varphi = \theta \,, \tag{2.2}$$

with $\theta = \boldsymbol{\nabla}\cdot \boldsymbol{u}$ the expansion of the velocity field ($\theta = 0$ for an incompressible flow),

$$\boldsymbol{\nabla}^2 \boldsymbol{\psi} = -\boldsymbol{\omega} \ , \tag{2.3}$$

with $\boldsymbol{\omega} = \boldsymbol{\nabla}\times \boldsymbol{u}$ the fluid vorticity, and lastly $\boldsymbol{u_\infty}$ the upstream constant velocity.

As established in Parapgraph 1.2.3, with the assumptions that θ vanishes at infinity with order r^{-3}, and adding the condition that φ tends to zero at infinity, the solution to Equation (2.2) is unique and given by :

$$\begin{aligned} \varphi(\boldsymbol{x}) &= \int_{\boldsymbol{y}\in\mathbb{R}^3} G(\boldsymbol{x},\boldsymbol{y})\theta(\boldsymbol{y})dy \\ &= \int_{\boldsymbol{y}\in\mathbb{R}^3} G(\boldsymbol{x},\boldsymbol{y})\, \boldsymbol{\nabla}_{\boldsymbol{y}}\cdot \boldsymbol{u}(\boldsymbol{y})dy \end{aligned} \tag{2.4}$$

with G the Green function :

$$G(\boldsymbol{x},\boldsymbol{y}) = \frac{1}{4\pi}\frac{1}{|\boldsymbol{y}-\boldsymbol{x}|} \ . \tag{2.5}$$

Similarly, as established in Paragraph 1.2.2, with the assumption that $\boldsymbol{\omega}$ vanishes at infinity with order r^{-3} and adding the conditions that $\boldsymbol{\psi}$ tends to zero at infinity, the solution to Equation (2.3) is unique and given by :

$$\begin{aligned} \boldsymbol{\psi}(\boldsymbol{x}) &= -\int_{\boldsymbol{y}\in\mathbb{R}^3} G(\boldsymbol{x},\boldsymbol{y})\boldsymbol{\omega}(\boldsymbol{y})dy \\ &= -\int_{\boldsymbol{y}\in\mathbb{R}^3} G(\boldsymbol{x},\boldsymbol{y})\, \boldsymbol{\nabla}_{\boldsymbol{y}}\times \boldsymbol{u}(\boldsymbol{y})dy \end{aligned} \tag{2.6}$$

When integrating the integral solutions (2.4) and (2.6) into the Helmholtz decomposition (2.1), we obtain :

$$\boldsymbol{u}(\boldsymbol{x}) = \boldsymbol{\nabla}_{\boldsymbol{x}}\left[\int_{\boldsymbol{y}\in\mathbb{R}^3} G(\boldsymbol{x},\boldsymbol{y})\, \boldsymbol{\nabla}_{\boldsymbol{y}}\cdot \boldsymbol{u}(\boldsymbol{y})dy\right] - \boldsymbol{\nabla}_{\boldsymbol{x}}\times\left[\int_{\boldsymbol{y}\in\mathbb{R}^3} G(\boldsymbol{x},\boldsymbol{y})\, \boldsymbol{\nabla}_{\boldsymbol{y}}\times \boldsymbol{u}(\boldsymbol{y})dy\right] + \boldsymbol{u_\infty} \tag{2.7}$$

2.2.2 Introduction of an obstacle body

Let us first envision a solid obstacle immersed in the flow immersed in the flow. As represented in Figure 2.2, the solid body B occupies the volume $\mathscr{V}_B$ and is bounded by the surface $\mathscr{S}_B$. As such, $\mathscr{S}_B$ is a surface of discontinuity for the velocity $\boldsymbol{u}$. $\mathscr{V}_F = \mathbb{R}^3 \setminus \mathscr{V}_B$ denotes the remaining fluid domain.

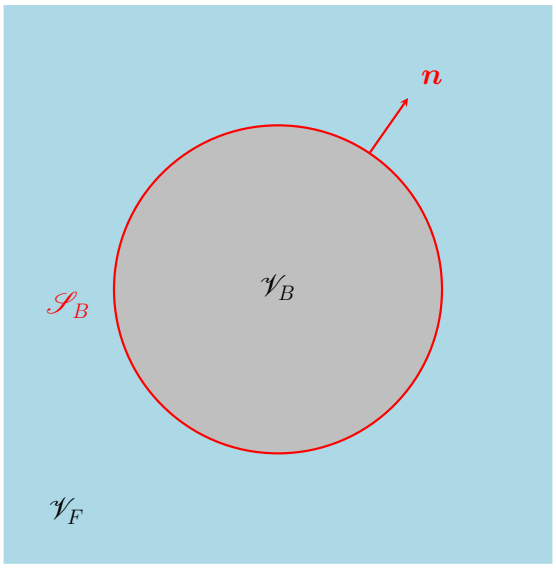

Figure 2.2: *Schematic representation of a solid body in a 3D fluid domain*

The fluid velocity $\boldsymbol{u}$ is considered null or constant inside the volume $\mathscr{V}_F$ bounded by the closed surface $\mathscr{S}_B$ with $\mathscr{S}_B$ a surface of discontinuity for $\boldsymbol{u}$. Using these assumptions, the integral velocity formulation of Equation (2.7) can be transformed by integration by parts and additional mathematical manipulations into :

$$\boldsymbol{u}(\boldsymbol{x}) = \boldsymbol{\nabla}_{\boldsymbol{x}} \left[\int_{\boldsymbol{y}\in\mathscr{V}_F} G(\boldsymbol{x},\boldsymbol{y})\, \boldsymbol{\nabla}_{\boldsymbol{y}} \cdot \boldsymbol{u}(\boldsymbol{y}) d\boldsymbol{y} \right] - \boldsymbol{\nabla}_{\boldsymbol{x}} \times \left[\int_{\boldsymbol{y}\in\mathscr{V}_F} G(\boldsymbol{x},\boldsymbol{y})\, \boldsymbol{\nabla}_{\boldsymbol{y}} \times \boldsymbol{u}(\boldsymbol{y}) d\boldsymbol{y} \right]$$
$$+ \boldsymbol{\nabla}_{\boldsymbol{x}} \left[\oint_{\boldsymbol{y}\in\mathscr{S}_B} G(\boldsymbol{x},\boldsymbol{y}) \boldsymbol{n}(\boldsymbol{y}) \cdot \boldsymbol{u}(\boldsymbol{y}) d\boldsymbol{y} \right] - \boldsymbol{\nabla}_{\boldsymbol{x}} \times \left[\oint_{\boldsymbol{y}\in\mathscr{S}_B} G(\boldsymbol{x},\boldsymbol{y}) \boldsymbol{n}(\boldsymbol{y}) \times \boldsymbol{u}(\boldsymbol{y}) d\boldsymbol{y} \right] + \boldsymbol{u}_{\boldsymbol{\infty}} \tag{2.8}$$

2.2.3 Application to the case of an incompressible quasi-irrotational flow

In this Paragraph, we will show how the previous decomposition may be used to analyze the flow around a body that is moving in arbitrary motion within an otherwise unbounded incompressible fluid.

Configuration

We consider once again a turbine in the form of the solid body B, occupying the three-dimensional volume $\mathscr{V}_B$ and bounded by the surface $\mathscr{S}_B$. A schematic representation of this configuration is shown in Figure 2.3. As a matter of simplicity, we will be showing hereafter an isolated turbine blade in place of the full three-bladed turbine body and the associated hub. However all methods described on a single blade can be naturally extended to the full turbine representation.

The turbine body B moves as a solid indeformable unit with the velocity $\boldsymbol{u}_B$, taking into account for instance the turbine rotation. Its wake W is often represented as a vortex layer shed at the trailing edge of the solid body onto a vortex sheet surface. However within the context of the Vortex Particle Method, there is no need for such an additional surface, as the fluid vorticity is accounted for in the form of equivalent fluid particles scattered throughout the fluid volume $\mathscr{V}_F$. As this equivalence has already been treated in Paragraph 1.2.4, we will be focusing only on the surfaces pertaining to the turbine body.

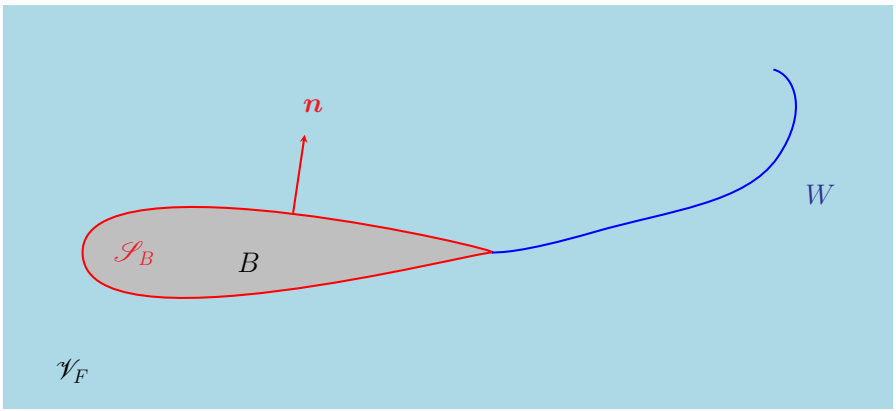

Figure 2.3: *Schematic representation of turbine blade and wake surfaces.*

Assumptions

In order to proceed with the refinement of the general velocity formulation of Equation (2.8), additional assumptions are required of the velocity field $\boldsymbol{u}$ which reflect this configuration.

1. $\boldsymbol{u}$ is incompressible, i.e. divergence-free :

$$\forall \boldsymbol{x} \in \mathbb{R}^3,\ \theta(\boldsymbol{x}) = \boldsymbol{\nabla}_{\boldsymbol{x}} \cdot \boldsymbol{u}(\boldsymbol{x}) = 0\ . \tag{2.9}$$

2. $\boldsymbol{u}$ is irrotational outside of the immediate vicinity of the sheer vortex layer W :

$$\forall \boldsymbol{x} \notin W,\ \boldsymbol{\omega}(\boldsymbol{x}) = \boldsymbol{\nabla}_{\boldsymbol{x}} \times \boldsymbol{u}(\boldsymbol{x}) = 0\ , \tag{2.10}$$

   or within the Lagrangian framework, outside of the immediate vicinity of the equivalent fluid particles.

3. $\boldsymbol{u}$ follows an impermeability condition along the boundary of the solid body :

$$\forall \boldsymbol{x} \in \mathscr{S}_B,\ \boldsymbol{u}(\boldsymbol{x}) \cdot \boldsymbol{n}(\boldsymbol{x}) = \boldsymbol{u}_B(\boldsymbol{x}) \cdot \boldsymbol{n}(\boldsymbol{x})\,. \tag{2.11}$$

   If noting $\Delta_{\mathscr{S}_B}\boldsymbol{u} = \boldsymbol{u} - \boldsymbol{u}_B$ the velocity jump between the outer and inner sides of the surface of discontinuity $\mathscr{S}_B$, this condition can also be written as :

$$\begin{aligned} \forall \boldsymbol{x} \in \mathscr{S}_B, \quad & \boldsymbol{u}(\boldsymbol{x}) \cdot \boldsymbol{n}(\boldsymbol{x}) - \boldsymbol{u}_B(\boldsymbol{x}) \cdot \boldsymbol{n}(\boldsymbol{x}) = 0 \\ & (\boldsymbol{u}(\boldsymbol{x}) - \boldsymbol{u}_B(\boldsymbol{x})) \cdot \boldsymbol{n}(\boldsymbol{x}) = 0 \\ & \Delta_{\mathscr{S}_B}\boldsymbol{u}(\boldsymbol{x}) \cdot \boldsymbol{n}(\boldsymbol{x}) = 0 \end{aligned} \tag{2.12}$$

2.2.4 Velocity decomposition

Once these assumptions have been laid out, we can continue to simplify the integral velocity formulation of Equation (2.8). To this end, we will be treating one after the other each of the four integral terms included in this sum :

$$\begin{aligned} \boldsymbol{u}(\boldsymbol{x}) = & \underbrace{\boldsymbol{\nabla}_{\boldsymbol{x}} \left[\int_{\boldsymbol{y} \in \mathscr{V}_F} G(\boldsymbol{x},\boldsymbol{y})\, \boldsymbol{\nabla}_{\boldsymbol{y}} \cdot \boldsymbol{u}(\boldsymbol{y}) d\boldsymbol{y} \right]}_{⓪} - \underbrace{\boldsymbol{\nabla}_{\boldsymbol{x}} \times \left[\int_{\boldsymbol{y} \in \mathscr{V}_F} G(\boldsymbol{x},\boldsymbol{y})\, \boldsymbol{\nabla}_{\boldsymbol{y}} \times \boldsymbol{u}(\boldsymbol{y}) d\boldsymbol{y} \right]}_{①} \\ & + \underbrace{\boldsymbol{\nabla}_{\boldsymbol{x}} \left[\oint_{\boldsymbol{y} \in \mathscr{S}_B} G(\boldsymbol{x},\boldsymbol{y}) \boldsymbol{n}(\boldsymbol{y}) \cdot \boldsymbol{u}(\boldsymbol{y}) d\boldsymbol{y} \right]}_{②} - \underbrace{\boldsymbol{\nabla}_{\boldsymbol{x}} \times \left[\oint_{\boldsymbol{y} \in \mathscr{S}_B} G(\boldsymbol{x},\boldsymbol{y}) \boldsymbol{n}(\boldsymbol{y}) \times \boldsymbol{u}(\boldsymbol{y}) d\boldsymbol{y} \right]}_{③} + \boldsymbol{u}_\infty \end{aligned} \tag{2.13}$$

Term ⓪

Term ⓪ of the sum can immediately be eliminated due to the incompressibility condition $\boldsymbol{\nabla}\cdot\boldsymbol{u}=0$, namely :

$$\boldsymbol{\nabla}_{\boldsymbol{x}}\left[\int_{\boldsymbol{y}\in\mathscr{V}_F} G(\boldsymbol{x},\boldsymbol{y})\,\boldsymbol{\nabla}_{\boldsymbol{y}}\cdot\boldsymbol{u}(\boldsymbol{y})dy\right]=0\,. \tag{2.14}$$

Term ①

In order to treat term ①, we begin by entering the rotational operator into the integral, after which we can apply the vector identity $\boldsymbol{\nabla}\times(\alpha\boldsymbol{F})=\nabla\alpha\times\boldsymbol{F}+\alpha\,\boldsymbol{\nabla}\times\boldsymbol{F}$, for any scalar field α and vector field $\boldsymbol{F}$:

$$\begin{aligned}&\boldsymbol{\nabla}_{\boldsymbol{x}}\times\left[\int_{\boldsymbol{y}\in\mathscr{V}_F} G(\boldsymbol{x},\boldsymbol{y})\,\boldsymbol{\nabla}_{\boldsymbol{y}}\times\boldsymbol{u}(\boldsymbol{y})dy\right]\\ =&\int_{\boldsymbol{y}\in\mathscr{V}_F}\boldsymbol{\nabla}_{\boldsymbol{x}}\times\left[G(\boldsymbol{x},\boldsymbol{y})\,\boldsymbol{\nabla}_{\boldsymbol{y}}\times\boldsymbol{u}(\boldsymbol{y})\right]dy\\ =&\int_{\boldsymbol{y}\in\mathscr{V}_F}\left[\boldsymbol{\nabla}_{\boldsymbol{x}}G(\boldsymbol{x},\boldsymbol{y})\times(\boldsymbol{\nabla}_{\boldsymbol{y}}\times\boldsymbol{u}(\boldsymbol{y}))+G(\boldsymbol{x},\boldsymbol{y})\,\boldsymbol{\nabla}_{\boldsymbol{x}}\times(\boldsymbol{\nabla}_{\boldsymbol{y}}\times\boldsymbol{u}(\boldsymbol{y}))\right]dy\end{aligned} \tag{2.15}$$

However given the mismatched derivation variables $\boldsymbol{\nabla}_{\boldsymbol{x}}\times(\boldsymbol{\nabla}_{\boldsymbol{y}}\times\boldsymbol{u}(\boldsymbol{y}))=0$ and thus the last part disappears :

$$\boldsymbol{\nabla}_{\boldsymbol{x}}\times\left[\int_{\boldsymbol{y}\in\mathscr{V}_F} G(\boldsymbol{x},\boldsymbol{y})\,\boldsymbol{\nabla}_{\boldsymbol{y}}\times\boldsymbol{u}(\boldsymbol{y})dy\right]=\int_{\boldsymbol{y}\in\mathscr{V}_F}\boldsymbol{\nabla}_{\boldsymbol{x}}G(\boldsymbol{x},\boldsymbol{y})\times(\boldsymbol{\nabla}_{\boldsymbol{y}}\times\boldsymbol{u}(\boldsymbol{y}))\,dy\,. \tag{2.16}$$

In this last formulation, we can replace the vorticity $\boldsymbol{\nabla}_{\boldsymbol{y}}\times\boldsymbol{u}(\boldsymbol{y})$ by its notation $\boldsymbol{\omega}(\boldsymbol{y})$ and the gradient of the Green function G by its known quantity, the Biot and Savart kernel $\boldsymbol{K}$:

$$\boldsymbol{\nabla}_{\boldsymbol{x}}\,G(\boldsymbol{x},\boldsymbol{y})=-\,\boldsymbol{\nabla}_{\boldsymbol{y}}\,G(\boldsymbol{x},\boldsymbol{y})=\boldsymbol{K}(\boldsymbol{x},\boldsymbol{y})=\frac{1}{4\pi}\frac{\boldsymbol{y}-\boldsymbol{x}}{|\boldsymbol{y}-\boldsymbol{x}|^3}\,. \tag{2.17}$$

Finally we obtain for term ① :

$$\boldsymbol{\nabla}_{\boldsymbol{x}}\times\left[\int_{\boldsymbol{y}\in\mathscr{V}_F} G(\boldsymbol{x},\boldsymbol{y})\,\boldsymbol{\nabla}_{\boldsymbol{y}}\times\boldsymbol{u}(\boldsymbol{y})dy\right]=\int_{\boldsymbol{y}\in\mathscr{V}_F}\boldsymbol{K}(\boldsymbol{x},\boldsymbol{y})\times\boldsymbol{\omega}(\boldsymbol{y})dy\,. \tag{2.18}$$

We can clearly identify this formulation as the rotational velocity component $\boldsymbol{u}^{\psi}$ of Equation (1.15).

Term ②

In order to rearrange surface integral term ②, we begin with the trick of expressing the velocity on $\mathscr{S}_B$ as :

$$\begin{aligned}\forall\boldsymbol{u}\in\mathscr{S}_B,\boldsymbol{u}(\boldsymbol{x})&=\boldsymbol{u}(\boldsymbol{x})-\boldsymbol{u}_B(\boldsymbol{x})+\boldsymbol{u}_B(\boldsymbol{x})\\ &=\Delta_{\mathscr{S}_B}\boldsymbol{u}(\boldsymbol{x})+\boldsymbol{u}_B(\boldsymbol{x})\end{aligned} \tag{2.19}$$

where as a reminder, $\Delta_{\mathscr{S}_B}\boldsymbol{u}=\boldsymbol{u}-\boldsymbol{u}_B$ denotes the velocity jump from the outer to inner sides of the discontinuity surface $\mathscr{S}_B$. When introducing this substitution, we obtain for term ② :

$$\begin{aligned}&\boldsymbol{\nabla}_{\boldsymbol{x}}\left[\int_{\boldsymbol{y}\in\mathscr{S}_B} G(\boldsymbol{x},\boldsymbol{y})\boldsymbol{n}(\boldsymbol{y})\cdot\boldsymbol{u}(\boldsymbol{y})dy\right]\\ =&\boldsymbol{\nabla}_{\boldsymbol{x}}\left[\int_{\boldsymbol{y}\in\mathscr{S}_B} G(\boldsymbol{x},\boldsymbol{y})\boldsymbol{n}(\boldsymbol{y})\cdot(\Delta_{\mathscr{S}_B}\boldsymbol{u}(\boldsymbol{y})+\boldsymbol{u}_B(\boldsymbol{y}))\,dy\right]\\ =&\boldsymbol{\nabla}_{\boldsymbol{x}}\left[\int_{\boldsymbol{y}\in\mathscr{S}_B} G(\boldsymbol{x},\boldsymbol{y})\boldsymbol{n}(\boldsymbol{y})\cdot\Delta_{\mathscr{S}_B}\boldsymbol{u}(\boldsymbol{y})dy\right]+\boldsymbol{\nabla}_{\boldsymbol{x}}\left[\int_{\boldsymbol{y}\in\mathscr{S}_B} G(\boldsymbol{x},\boldsymbol{y})\boldsymbol{n}(\boldsymbol{y})\cdot\boldsymbol{u}_B(\boldsymbol{y})dy\right]\end{aligned} \tag{2.20}$$

Due to the impermeability condition as formulated in Equation (2.12), $\boldsymbol{n}(\boldsymbol{y})\cdot\Delta_{\mathscr{S}_B}\boldsymbol{u}(\boldsymbol{y})=0$ and thus the first part of this expression disappears. Term ② can finally be written as :

$$\boldsymbol{\nabla}_{\boldsymbol{x}}\left[\int_{\boldsymbol{y}\in\mathscr{S}_B} G(\boldsymbol{x},\boldsymbol{y})\boldsymbol{n}(\boldsymbol{y})\cdot\boldsymbol{u}(\boldsymbol{y})dy\right]=\boldsymbol{\nabla}_{\boldsymbol{x}}\left[\int_{\boldsymbol{y}\in\mathscr{S}_B} G(\boldsymbol{x},\boldsymbol{y})\boldsymbol{n}(\boldsymbol{y})\cdot\boldsymbol{u}_B(\boldsymbol{y})dy\right] \tag{2.21}$$

We can identify this formulation as the velocity induced by a source singularity distribution of intensity $\sigma(\boldsymbol{y})=\boldsymbol{n}(\boldsymbol{y})\cdot\boldsymbol{u}_B(\boldsymbol{y})$ on $\mathscr{S}_B$, as will be revisited later on.

Term ③

The second surface integral term of ③ can also be rearranged using the substitution of Equation (2.19), leading to :

$$\begin{aligned}
&\boldsymbol{\nabla}_{\boldsymbol{x}}\times\left[\int_{\boldsymbol{y}\in\mathscr{S}_B} G(\boldsymbol{x},\boldsymbol{y})\boldsymbol{n}(\boldsymbol{y})\times\boldsymbol{u}(\boldsymbol{y})dy\right]\\
=&\,\boldsymbol{\nabla}_{\boldsymbol{x}}\times\left[\int_{\boldsymbol{y}\in\mathscr{S}_B} G(\boldsymbol{x},\boldsymbol{y})\boldsymbol{n}(\boldsymbol{y})\times\left(\Delta_{\mathscr{S}_B}\boldsymbol{u}(\boldsymbol{y})+\boldsymbol{u}_B(\boldsymbol{y})\right)dy\right]\\
=&\,\boldsymbol{\nabla}_{\boldsymbol{x}}\times\left[\int_{\boldsymbol{y}\in\mathscr{S}_B} G(\boldsymbol{x},\boldsymbol{y})\boldsymbol{n}(\boldsymbol{y})\times\Delta_{\mathscr{S}_B}\boldsymbol{u}(\boldsymbol{y})dy\right]+\boldsymbol{\nabla}_{\boldsymbol{x}}\times\left[\int_{\boldsymbol{y}\in\mathscr{S}_B} G(\boldsymbol{x},\boldsymbol{y})\boldsymbol{n}(\boldsymbol{y})\times\boldsymbol{u}_B(\boldsymbol{y})dy\right]
\end{aligned} \tag{2.22}$$

The second part of this expression can easily be eliminated if the solid body velocity $\boldsymbol{u}_B$ is a translation or rotation movement. We can then enter the curl operator into the remaining integral :

$$\begin{aligned}
&\boldsymbol{\nabla}_{\boldsymbol{x}}\times\left[\int_{\boldsymbol{y}\in\mathscr{S}_B} G(\boldsymbol{x},\boldsymbol{y})\boldsymbol{n}(\boldsymbol{y})\times\boldsymbol{u}(\boldsymbol{y})dy\right]\\
=&\,\boldsymbol{\nabla}_{\boldsymbol{x}}\times\left[\int_{\boldsymbol{y}\in\mathscr{S}_B} G(\boldsymbol{x},\boldsymbol{y})\boldsymbol{n}(\boldsymbol{y})\times\Delta_{\mathscr{S}_B}\boldsymbol{u}(\boldsymbol{y})dy\right]\\
=&\int_{\boldsymbol{y}\in\mathscr{S}_B}\boldsymbol{\nabla}_{\boldsymbol{x}}\times\left[G(\boldsymbol{x},\boldsymbol{y})\boldsymbol{n}(\boldsymbol{y})\times\Delta_{\mathscr{S}_B}\boldsymbol{u}(\boldsymbol{y})\right]dy
\end{aligned} \tag{2.23}$$

We use once more the vector identity $\boldsymbol{\nabla}\times(\alpha\boldsymbol{F})=\nabla\alpha\times\boldsymbol{F}+\alpha\,\boldsymbol{\nabla}\times\boldsymbol{F}$ in order to develop the expression :

$$\begin{aligned}
&\boldsymbol{\nabla}_{\boldsymbol{x}}\times\left[G(\boldsymbol{x},\boldsymbol{y})\boldsymbol{n}(\boldsymbol{y})\times\Delta_{\mathscr{S}_B}\boldsymbol{u}(\boldsymbol{y})\right]\\
=&\,\boldsymbol{\nabla}_{\boldsymbol{x}}\,G(\boldsymbol{x},\boldsymbol{y})\times\left(\boldsymbol{n}(\boldsymbol{y})\times\Delta_{\mathscr{S}_B}\boldsymbol{u}(\boldsymbol{y})\right)+G(\boldsymbol{x},\boldsymbol{y})\,\boldsymbol{\nabla}_{\boldsymbol{x}}\times\left(\boldsymbol{n}(\boldsymbol{y})\times\Delta_{\mathscr{S}_B}\boldsymbol{u}(\boldsymbol{y})\right)
\end{aligned} \tag{2.24}$$

where due to the mismatch in integration variables the second part disappears, and we can once more replace the gradient of G by the Biot and Savart Kernel $\boldsymbol{K}$ of Equation (2.17) :

$$\begin{aligned}
\boldsymbol{\nabla}_{\boldsymbol{x}}\times\left[G(\boldsymbol{x},\boldsymbol{y})\boldsymbol{n}(\boldsymbol{y})\times\Delta_{\mathscr{S}_B}\boldsymbol{u}(\boldsymbol{y})\right]&=\boldsymbol{\nabla}_{\boldsymbol{x}}\,G(\boldsymbol{x},\boldsymbol{y})\times\left(\boldsymbol{n}(\boldsymbol{y})\times\Delta_{\mathscr{S}_B}\boldsymbol{u}(\boldsymbol{y})\right)\\
&=\boldsymbol{K}(\boldsymbol{x},\boldsymbol{y})\times\left(\boldsymbol{n}(\boldsymbol{y})\times\Delta_{\mathscr{S}_B}\boldsymbol{u}(\boldsymbol{y})\right)
\end{aligned} \tag{2.25}$$

We obtain for term ③ :

$$\boldsymbol{\nabla}_{\boldsymbol{x}}\times\left[\int_{\boldsymbol{y}\in\mathscr{S}_B} G(\boldsymbol{x},\boldsymbol{y})\boldsymbol{n}(\boldsymbol{y})\times\boldsymbol{u}(\boldsymbol{y})dy\right]=\int_{\boldsymbol{y}\in\mathscr{S}_B}\boldsymbol{K}(\boldsymbol{x},\boldsymbol{y})\times\left(\boldsymbol{n}(\boldsymbol{y})\times\Delta_{\mathscr{S}_B}\boldsymbol{u}(\boldsymbol{y})\right)dy \tag{2.26}$$

In order to make one last refinement to this formulation, we can assume that the flow $\boldsymbol{u}$ is irrotational outisde of the wake, as prescribed by Equation (2.10). The velocity $\boldsymbol{u}$ on the body surface $\mathscr{S}_B$ can be expressed through its entire potential noted once again φ :

$$\forall\boldsymbol{x}\in\mathscr{S}_B,\ \boldsymbol{u}(\boldsymbol{x})\simeq\boldsymbol{\nabla}_{\boldsymbol{x}}\,\varphi(\boldsymbol{x})+\boldsymbol{u}_{\boldsymbol{\infty}}\ . \tag{2.27}$$

The velocity jump along the body surface can then be written as :

$$\begin{aligned}\Delta_{\mathscr{S}_B}\boldsymbol{u}(\boldsymbol{x}) &= \Delta_{\mathscr{S}_B}\left(\boldsymbol{\nabla}_{\boldsymbol{x}}\,\varphi(\boldsymbol{x})\right)\\ &= \boldsymbol{\nabla}_{\boldsymbol{x}}\left(\Delta_{\mathscr{S}_B}\varphi(\boldsymbol{x})\right)\\ &= \boldsymbol{\nabla}_{\boldsymbol{x}}\,\mu(\boldsymbol{x})\ ,\end{aligned} \tag{2.28}$$

defining μ on $\mathscr{S}_B$ as the scalar quantity $\mu = \Delta_{\mathscr{S}_B}\varphi$. With this substitution, the expression for term ③ of Equation (2.26) becomes :

$$\boldsymbol{\nabla}_{\boldsymbol{x}}\times\left[\int_{\boldsymbol{y}\in\mathscr{S}_B} G(\boldsymbol{x},\boldsymbol{y})\boldsymbol{n}(\boldsymbol{y})\times\boldsymbol{u}(\boldsymbol{y})d\boldsymbol{y}\right] = \int_{\boldsymbol{y}\in\mathscr{S}_B}\boldsymbol{K}(\boldsymbol{x},\boldsymbol{y})\times\left(\boldsymbol{n}(\boldsymbol{y})\times\boldsymbol{\nabla}_{\boldsymbol{y}}\,\mu(\boldsymbol{y})\right)d\boldsymbol{y} \tag{2.29}$$

With additional mathematical developments, this formulation can become :

$$\begin{aligned}\boldsymbol{\nabla}_{\boldsymbol{x}}\times\left[\int_{\boldsymbol{y}\in\mathscr{S}_B} G(\boldsymbol{x},\boldsymbol{y})\boldsymbol{n}(\boldsymbol{y})\times\boldsymbol{u}(\boldsymbol{y})d\boldsymbol{y}\right] &= \int_{\boldsymbol{y}\in\mathscr{S}_B}\boldsymbol{K}(\boldsymbol{x},\boldsymbol{y})\times\left(\boldsymbol{n}(\boldsymbol{y})\times\boldsymbol{\nabla}_{\boldsymbol{y}}\,\mu(\boldsymbol{y})\right)d\boldsymbol{y}\\ &= \boldsymbol{\nabla}_{\boldsymbol{x}}\left[\int_{\boldsymbol{y}\in\mathscr{S}_B}\boldsymbol{K}(\boldsymbol{x},\boldsymbol{y})\cdot\left(\mu(\boldsymbol{y})\boldsymbol{n}(\boldsymbol{y})\right)d\boldsymbol{y}\right]\end{aligned} \tag{2.30}$$

We can identify this formulation as the velocity induced by a dipole singularity distribution of intensity $\boldsymbol{\gamma} = \mu\boldsymbol{n}$ on $\mathscr{S}_B$, which can also be described as a normal dipole distribution of intensity μ.

Final velocity formulation

By assembling the reorganizations of terms ① ② and ③ of the intial velocity formulation of Equation(2.13), given by the expressions (2.18) (2.21) and (2.30) respectively, we obtain the velocity decomposition :

$$\begin{aligned}\boldsymbol{u}(\boldsymbol{x}) = &\underbrace{-\int_{\boldsymbol{y}\in\mathscr{V}_F}\boldsymbol{K}(\boldsymbol{x},\boldsymbol{y})\times\boldsymbol{\omega}(\boldsymbol{y})d\boldsymbol{y}}_{①} + \underbrace{\boldsymbol{\nabla}_{\boldsymbol{x}}\left[\int_{\boldsymbol{y}\in\mathscr{S}_B} G(\boldsymbol{x},\boldsymbol{y})\boldsymbol{n}(\boldsymbol{y})\cdot\boldsymbol{u}_B d\boldsymbol{y}\right]}_{②}\\ &\underbrace{-\boldsymbol{\nabla}_{\boldsymbol{x}}\left[\int_{\boldsymbol{y}\in\mathscr{S}_B}\boldsymbol{K}(\boldsymbol{x},\boldsymbol{y})\cdot\left(\mu(\boldsymbol{y})\boldsymbol{n}(\boldsymbol{y})\right)d\boldsymbol{y}\right]}_{③}\end{aligned} \tag{2.31}$$

2.2.5 Treatment of velocity contributions

As evoked in the developments leading to the velocity formulation of Equation (2.31), each term of this decomposition can be identified as a particular type of contribution. We can now reiterate and expand on the significance and resolution of each of these terms.

① The first term :

$$-\int_{\boldsymbol{y}\in\mathscr{V}_F}\boldsymbol{K}(\boldsymbol{x},\boldsymbol{y})\times\boldsymbol{\omega}(\boldsymbol{y})d\boldsymbol{y} \tag{2.32}$$

describes the rotational velocity in the flow, as presented in Paragraph 1.2.2 of the previous Chapter. Its treatment will remain unchanged : discretization into vorticity carrying fluid particles emitted from the solid body mesh trailing edges.

② The second term :

$$\boldsymbol{\nabla}_{\boldsymbol{x}}\left[\int_{\boldsymbol{y}\in\mathscr{S}_B} G(\boldsymbol{x},\boldsymbol{y})\left(\boldsymbol{n}(\boldsymbol{y})\cdot\boldsymbol{u}_B(\boldsymbol{y})\right)d\boldsymbol{y}\right] \tag{2.33}$$

is the velocity deriving from the potential

$$\int_{\boldsymbol{y}\in\mathscr{S}_B} G(\boldsymbol{x},\boldsymbol{y})\left(\boldsymbol{n}(\boldsymbol{y})\cdot\boldsymbol{u}_B(\boldsymbol{y})\right)dy = \int_{\boldsymbol{y}\in\mathscr{S}_B} G(\boldsymbol{x},\boldsymbol{y})\sigma(\boldsymbol{y})dy\ , \tag{2.34}$$

which we can recognize as the potential generated by a source distribution of intensity $\sigma(\boldsymbol{y}) = \boldsymbol{n}(\boldsymbol{y})\cdot\boldsymbol{u}_B(\boldsymbol{y})$, a known quantity the body surface $\mathscr{S}_B$. Its treatment and discretization will be described in Paragraph 2.4.2.

③ The third term :

$$-\boldsymbol{\nabla}_{\boldsymbol{x}}\left[\int_{\boldsymbol{y}\in\mathscr{S}_B}\boldsymbol{K}(\boldsymbol{x},\boldsymbol{y})\cdot(\mu(\boldsymbol{y})\boldsymbol{n}(\boldsymbol{y}))dy\right] \tag{2.35}$$

is the velocity deriving from the potential

$$-\int_{\boldsymbol{y}\in\mathscr{S}_B}\boldsymbol{K}(\boldsymbol{x},\boldsymbol{y})\cdot(\mu(\boldsymbol{y})\boldsymbol{n}(\boldsymbol{y}))dy\ , \tag{2.36}$$

which we can recognize as the potential generated by a normal dipole distribution of intensity $\boldsymbol{\gamma}(\boldsymbol{y}) = \mu(\boldsymbol{y})\boldsymbol{n}(\boldsymbol{y})$, where $\mu(\boldsymbol{y})$ is an unknown quantity on the body surface $\mathscr{S}_B$. This component will be treated as described in Paragraph 1.2.3 of the previous Chapter : the solution for the value of the dipole intensity μ on each discretized mesh face is given by the resolution of a linear system ensuring the verification of the impermeability condition (2.11).

2.3 Fluid particle emission

Once the velocity contributions have been established, the emission of fluid particles at the now two-sided trailing edge of the mesh must be adapted to take into account the new configuration. The theoretical framework for the choices made here remains as exposed previously in Paragraph 1.2.4. We will touch more rapidly onto Bernoulli's relation supporting the emission model before moving onto the process of incorporating contributions from both intrados and extrados mesh faces attached to each blade trailing edge segment.

Figure 2.4 will show a schematic representation of this situation, with the letters e and i denoting quantities associated to the extrados and intrados sides of the turbine blade respectively, and $(\boldsymbol{n},\boldsymbol{s},\boldsymbol{t})$ a localised frame associated to each trailing edge segment.

2.3.1 Bernoulli relation

Bernoulli's relation for an unsteady potential irrotational flow is used once again, applied this time not to the two side of a zero-thickness mesh face but rather to the two faces $\mathscr{S}^e$ and $\mathscr{S}^i$ situated on the intrados and extrados sides of a common trailing edge.

Once again, the conclusion is reached that the newly created fluid particles shed from the normal dipole distribution μ on the solid body surface are introduced into the flow with the initial average velocity $\boldsymbol{u}^{\boldsymbol{\varphi}}_{\boldsymbol{m}} = \dfrac{\boldsymbol{u}^{\boldsymbol{\varphi}e} + \boldsymbol{u}^{\boldsymbol{\varphi}i}}{2}$.

2.3.2 Kutta condition

Let us consider a dummy mesh face $\mathscr{S}'_k$ shed along each segment of the trailing edge, in the wake of each pair of intrados and extrados trailing edge mesh faces $\mathscr{S}^e_k$ and $\mathscr{S}^i_k$. The dipole intensity μ'_k shed onto this dummy face is calculated based on the dipole intensities μ^e_k and μ^i_k attached to the faces $\mathscr{S}^e_k$ and $\mathscr{S}^i_k$. Recalling that a dipole intensity μ can be

equated to a jump in potential $\Delta\varphi$, and using the notations shown in Figure 2.4 for all sets of faces k along the trailing edges :

$$\mu_k^e = \varphi_+^e - \varphi_-^e \ , \tag{2.37}$$
$$\mu_k^i = \varphi_+^i - \varphi_-^i \ , \tag{2.38}$$
$$\mu_k = \varphi_+ - \varphi_- \ . \tag{2.39}$$

What's more, as the two trailing edge faces are collapsed into this single infintely thin dummy face at the trailing edge point, it can also be assumed that :

$$\mu_k = \varphi_+^e - \varphi_+^i \ , \tag{2.40}$$

or alternately :

$$\varphi_+ = \varphi_+^e \text{ and } \varphi_- = \varphi_+^i \ . \tag{2.41}$$

Finally, the potentials joined on the inside of the mesh are also assumed to be equal :

$$\varphi_-^e = \varphi_-^i \ . \tag{2.42}$$

We now obtain :

$$\mu_k = \varphi_+ - \varphi_- \tag{2.43}$$
$$= \varphi_+^e - \varphi_+^i \tag{2.44}$$
$$= (\varphi_+^e - \varphi_-^e) - (\varphi_+^i - \varphi_-^e) \tag{2.45}$$
$$= (\varphi_+^e - \varphi_-^e) - (\varphi_+^i - \varphi_-^i) \ . \tag{2.46}$$
$$= \mu_k^e - \mu_k^i \tag{2.47}$$

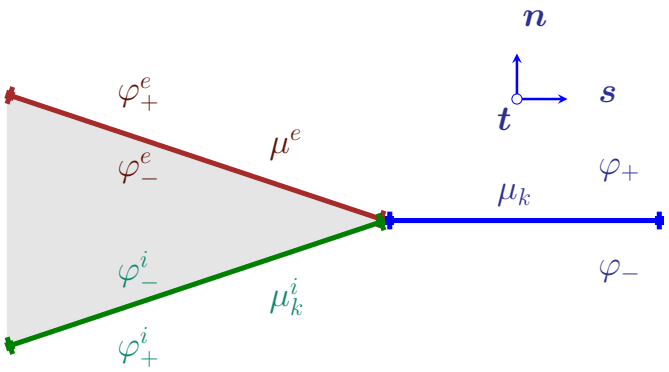

Figure *2.4: Schematic representation of a thick blade trailing edge : side view of the extrados and intrados faces along the trailing edge, and the dummy face following the trailing edge at the onset of the wake.*

Once we have established the intensity μ_k of the dipole shed onto each section of the wake, we can then convert this dipole intensity on a dummy wake face into an equivalent vorticity carrying particle.

2.3.3 Fluid particle equivalent to the shed dipole

Using the notations shown in Figure 2.5, we now have access to value of the dipole intensity μ_k shed onto each dummy wake mesh face $\mathscr{S}'_k$ along the trailing edge. According

to the reasoning beginning with Equation (1.46) of Paragraph 1.2.4, we can deduce from these dipole intensities the vortical weight $\boldsymbol{\Omega}'_k$ of the equivalent fluid particle to each dummy face $\mathscr{S}'_k$ as given by Equation (1.58) :

$$\boldsymbol{\Omega}'_{\boldsymbol{k}} = \int_{\mathscr{S}'_k} \boldsymbol{n}(\boldsymbol{y}) \times (\boldsymbol{\nabla}_{\boldsymbol{y}}\, \mu(\boldsymbol{y}))\, dy \tag{2.48}$$

$$\simeq [\mu_k(t) - \mu_k(t - dt)]\, dl\boldsymbol{t} + \frac{\mu_{k+1} - \mu_{k-1}}{2} |\boldsymbol{u}^{\boldsymbol{\varphi}}_{\boldsymbol{m}k}| dt\boldsymbol{s} \tag{2.49}$$

Using relation (2.47), the value of the intensity μ_k is given by the dipole intensities μ^e_k and μ^i_k attached to the extrados and intrados emission faces :

$$\boldsymbol{\Omega}'_k = \left[\left(\mu^e_k(t) - \mu^i_k(t)\right) - \left(\mu^e_k(t - \delta t) - \mu^i_k(t - \delta t)\right)\right] dl\boldsymbol{t} + \frac{(\mu^e_{k+1} - \mu^i_{k+1}) - (\mu^e_{k-1} - \mu^i_{k-1})}{2} |\boldsymbol{u}^{\boldsymbol{\varphi}}_{\boldsymbol{m}k}| dt\boldsymbol{s}\ , \tag{2.50}$$

which can if desired be reordered into :

$$\boldsymbol{\Omega}'_k = \left[(\mu^e_k(t) - \mu^e_k(t - \delta t)) - \left(\mu^i_k(t) - \mu^i_k(t - \delta t)\right)\right] dl\boldsymbol{t} + \left(\frac{\mu^e_{k+1} - \mu^e_{k-1}}{2} - \frac{\mu^i_{k+1} - \mu^i_{k-1}}{2}\right) |\boldsymbol{u}^{\boldsymbol{\varphi}}_{\boldsymbol{m}k}| dt\boldsymbol{s}\ . \tag{2.51}$$

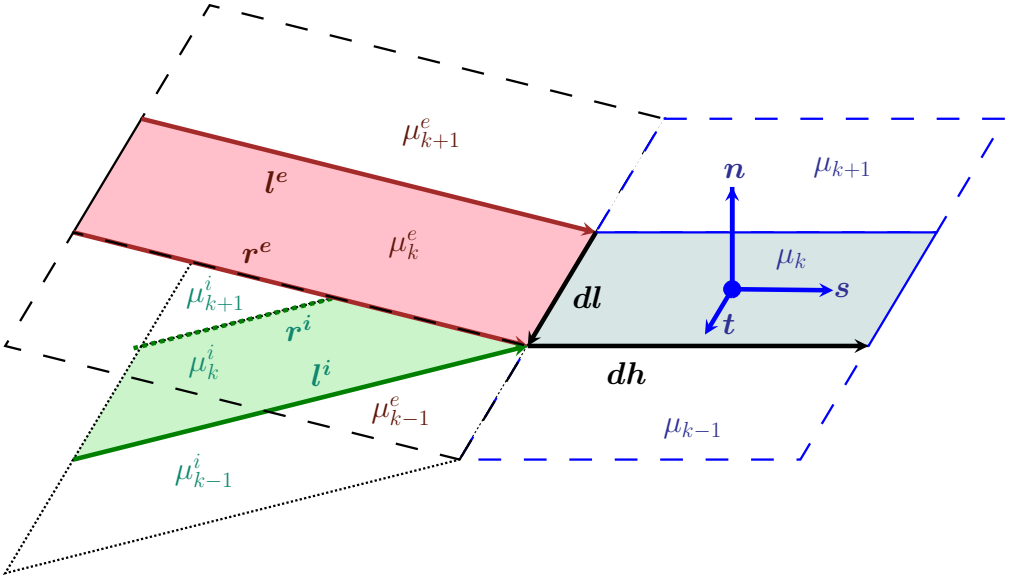

Figure 2.5: *Schematic representation of a thick blade trailing edge : extrados and intrados faces along the trailing edge, with their left and right hand neighbor faces, and the dummy faces following the trailing edge at the onset of the wake.*

2.3.4 Properties of the new particle

The longitudinal direction of the dummy wake face $\mathscr{S}'_k$ is the direction of the emission velocity :

$$\boldsymbol{s} = \frac{\boldsymbol{u}^{\boldsymbol{\varphi}}_{\boldsymbol{m}k}}{|\boldsymbol{u}^{\boldsymbol{\varphi}}_{\boldsymbol{m}k}|}\ . \tag{2.52}$$

At the first iteration of the simulation code, when the emission velocity has yet to be established, we consider instead the average direction of the trailing edge faces :

$$\boldsymbol{s} = \frac{1}{4}\left(\frac{\boldsymbol{r}^e}{|\boldsymbol{r}^e|} + \frac{\boldsymbol{l}^e}{|\boldsymbol{l}^e|} + \frac{\boldsymbol{r}^i}{|\boldsymbol{r}^i|} + \frac{\boldsymbol{l}^i}{|\boldsymbol{l}^i|}\right)\ , \tag{2.53}$$

using the notations shown in Figure 2.5. The tangential direction of $\mathscr{S}'_k$ is given by the mesh segment it is attached to :

$$\boldsymbol{t} = \frac{\boldsymbol{dl}}{|\boldsymbol{dl}|} \, . \tag{2.54}$$

The normal to $\mathscr{S}'_k$ can then be deduced :

$$\boldsymbol{n} = \boldsymbol{t} \times \boldsymbol{s} \, . \tag{2.55}$$

The dummy face $\mathscr{S}'_k$ is rectangular in shape, of sizes $dl = |\boldsymbol{dl}|$ and as the new particles are emitted with the initial velocity $\boldsymbol{u}^{\varphi}_{\boldsymbol{m}}$:

$$|\boldsymbol{dh}| = dh = \left|\boldsymbol{u}^{\varphi}_{\boldsymbol{m}}\right| dt \, . \tag{2.56}$$

The new equivalent fluid particle is positioned at the center of this rectangle, as defined in the previous Chapter by Equation (1.57). The volume of the equivalent particle also remains as given by Equation (1.60) :

$$V_k \simeq dl \left|\boldsymbol{u}^{\varphi}_{\boldsymbol{m}}\right| \delta t \, \epsilon \, , \tag{2.57}$$

where ϵ denotes once again the regularisation parameter of the simulation.

Combined with the remaining elements of the simulation code already described in the previous Chapter, this concludes the description of the alternative velocity decomposition and fluid particle emission process adapted to a fully rendered turbine mesh configuration. The next hurdle lies in the computation of efforts, as the previous method yielded unsatisfactory results and no longer applies given the addition of an extra velocity contribution on the mesh.

2.4 Velocity potential computations

Bernoulli's relation gives the value of the pressure distribution on the mesh based on the value of the velocity potential, as given by Equation (1.39). However the Vortex Particle Method uses a velocity decomposition, and does not allow for any direct or simple access to its potential. Therefore, additional calculations are required in order to obtain the velocity potential on the mesh.

The first possibility for computing the velocity potential on the mesh would be to consider a potential decomposition mirroring the velocity decomposition of Equation (2.31). The two surface integral terms ② and ③ are clearly formulated as already deriving directly from velocity potentials induced by source and dipole distributions respectively. The potentials induced by source or dipole distributions are well known quantities and used in many potential codes. The calculation and numerical computation of such potential contributions is covered in detail by Bousquet [53]. However the difficulty of this option lies with the last term ③, which unlike the others does not derive directly from a velocity potential. While it might be possible to retrace the velocity potential induced by vorticity carrying particles, this subject is much less common in the literature and would require further theoretical developments and possibly significant additions to the simulation code.

A second and far simpler possibility for the computation of the velocity potential is given in the recent work of Ogami [86]. By "integrating" the complete velocity on the obstacle mesh, he is able to obtain an approximation of its potential at the cost of a matrix resolution. As to our knowledge this method has not yet been picked up outside of the works of Ogami, we have taken the steps to validate its accuracy for the use we

are looking to make of it. To this end, we will be considering the simplified and ideal situation of a sphere in a purely potential flow. This eliminates the need for velocity contributions pertaining to vorticity, allowing for yet another velocity formulation using only source singularity contributions. The potential computed from this complete velocity using Ogami's approximation can then be compared to the potential induced by a source distribution as given by Bousquet [53], as well as the analytical reference of the velocity potential on the surface of a sphere in a potential flow.

Once this method for the computation of potential has proven itself to be satisfactory, we can then move on to the computation of efforts, which we aim to apply to the full velocity and turbine blade configuration.

2.4.1 Velocity potential induced by a source distribution

Before moving on to Ogami's new method for the computation of the velocity potential, we begin by describing the more common reference of the potential induced by a source singularity distribution of intensity σ on an obstacle surface $\mathscr{S}_B$, as given by Bousquet [53]. This source potential calculation will be used as a comparison point later on in the validation of Ogami's approach. Incidentally, this is the potential from which is derived the source velocity contribution of term ② from Equation (2.31), as mentioned in Paragraph 2.2.5.

The velocity potential φ_σ induced by a source distribution σ on a regular bounded surface $\mathscr{S}_B$ is given by :

$$\varphi_\sigma(\boldsymbol{x}) = \int_{\boldsymbol{y}\in\mathscr{S}_B} G(\boldsymbol{x},\boldsymbol{y})\sigma(\boldsymbol{y})dy + C \ , \tag{2.58}$$

known up to the constant C.

For the sake of discretization, the value of σ is considered as a constant σ_j on each of the N_f faces $\mathscr{S}_j$ making up the surface $\mathscr{S}_B$. Through some geometrical manipulations, we can then obtain the discrete formulation :

$$\varphi_\sigma(\boldsymbol{x}) = \frac{1}{4\pi}\sum_{j=1}^{N_f} \sigma_j \alpha_j(\boldsymbol{x}) + C \ . \tag{2.59}$$

α_j are coefficients computed from the geometry of the mesh faces, given by :

$$\alpha_j(\boldsymbol{x}) \simeq \sum_{i=1}^{4} \left[w_{i,j}\Lambda_{i,j} + h_j(\arctan(\beta_{i,j}) + \arctan(\gamma_{i,j}))\right] \tag{2.60}$$

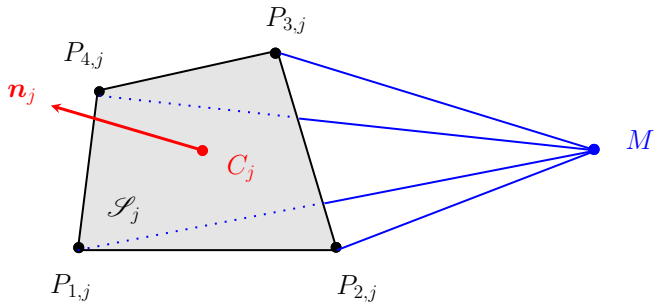

Figure 2.6: *Schematic representation of a quadrangular mesh face $\mathscr{S}_j$ of normal $\boldsymbol{n}_j$ and center C_j and the quantities necessary for the computation of the velocity potential at the evalutaion point M of coordinates $\boldsymbol{x}$.*

where using the notations shown on Figure 2.6 :

$$h_j = |\boldsymbol{n}_j \cdot \boldsymbol{C_j M}| \tag{2.61}$$
$$l_{i,j} = P_{i,j}P_{i+1,j} \tag{2.62}$$
$$\boldsymbol{r}_{i,j} = \boldsymbol{P_{i,j}M} \tag{2.63}$$
$$\boldsymbol{t}_{i,j} = \frac{\boldsymbol{P_{i,j}P_{i+1,j}}}{l_{i,j}} \tag{2.64}$$
$$r_{i,j} = |\boldsymbol{r}_{i,j}| \tag{2.65}$$
$$a_{i,j} = \boldsymbol{r}_{i,j} \cdot \boldsymbol{t}_{i,j} \tag{2.66}$$
$$b_{i,j} = \boldsymbol{r}_{i+1,j} \cdot \boldsymbol{t}_{i,j} \tag{2.67}$$
$$w_{i,j} = (\boldsymbol{t}_{i,j} \times \boldsymbol{n}_j) \cdot \boldsymbol{r}_{i,j} \tag{2.68}$$
$$d_{i,j} = h_j^2 + w_{i,j}^2 \tag{2.69}$$
$$\beta_{i,j} = \frac{-w_{i,j}a_{i,j}}{d_{i,j} + h_j r_{i,j}} \tag{2.70}$$
$$\gamma_{i,j} = \frac{w_{i,j}b_{i,j}}{d_{i,j} + h_j r_{i+1,j}} \tag{2.71}$$
$$\Lambda_{i,j} = \log \frac{r_{i,j} + r_{i+1,j} + l_{i,j}}{r_{i,j} + r_{i+1,j} - l_{i,j}} \tag{2.72}$$

The determination of only remaining unknown source singularity intensities σ_j will be covered in the next Paragraph.

2.4.2 Velocity induced by a source distribution

This forumlation follows naturally from the velocity potential computation, and will become relevant later on in the process of validation of Ogami's method through the computation of a potential flow. Thus we continue with the description of the velocity contribution induced by a source singularity distribution of intensity σ on an obstacle surface $\mathscr{S}_B$, as given by Bousquet [53]. Incidentally, a version of this formulation is also used in order to compute the source singularity term ② of Equation (2.31).

The velocity $\boldsymbol{u}_\sigma$ induced by a source distribution σ on a regular bounded surface $\mathscr{S}_B$ is given by :

$$\boldsymbol{u}_\sigma(\boldsymbol{x}) = \boldsymbol{\nabla}_{\boldsymbol{x}} \left[\int_{\boldsymbol{y} \in \mathscr{S}_B} G(\boldsymbol{x}, \boldsymbol{y}) \sigma(\boldsymbol{y}) dy \right] . \tag{2.73}$$

If once again the value of σ is assumed to be a constant σ_j on each individual mesh face $\mathscr{S}_j$, the velocity induced by this source distribution can be approximated as :

$$\boldsymbol{u}_\sigma(\boldsymbol{x}) = \frac{1}{4\pi}\sum_{j=1}^{N_f}\sigma_j \boldsymbol{v}_j(\boldsymbol{x}) \,, \tag{2.74}$$

with :

$$\boldsymbol{v}_j(\boldsymbol{y}) = \sum_{i=1}^{4}\left(\boldsymbol{\nu}_{i,j}\Lambda_{i,j} + \boldsymbol{n}_j \mathrm{Sgn}_j\left[\arctan\alpha_{i,j} + \arctan\beta_{i,j}\right]\right) \,, \tag{2.75}$$

where using once again the notations of Figure 2.6 :

$$h_j = |\boldsymbol{n}_j \cdot \boldsymbol{C_j M}| \tag{2.76}$$
$$l_{i,j} = |P_{i,j}P_{i+1,j}| \tag{2.77}$$
$$\boldsymbol{t}_{i,j} = \frac{\boldsymbol{P_{i,j}P_{i+1,j}}}{l_{i,j}} \tag{2.78}$$
$$\boldsymbol{\nu}_{i,j} = \boldsymbol{t}_{i,j} \times \boldsymbol{n}_j \tag{2.79}$$
$$a_{i,j} = \boldsymbol{r}_{i,j} \cdot \boldsymbol{t}_{i,j} \tag{2.80}$$
$$\omega_{i,j} = \boldsymbol{\nu}_{i,j} \cdot \boldsymbol{r}_{i,j} \tag{2.81}$$
$$\alpha_{i,j} = \frac{-\omega_{i,j}a_{i,j}}{d_{i,j}^2 + h_j r_{i,j}} \tag{2.82}$$
$$\mathrm{Sgn}_j = \text{ sign of } (\boldsymbol{n}_j \cdot \boldsymbol{C_j M}) \ \ (= \pm 1) \tag{2.83}$$
$$\boldsymbol{r}_{i,j} = \boldsymbol{P_{i,j}M} \tag{2.84}$$
$$r_{i,j} = |\boldsymbol{r}_{i,j}| \tag{2.85}$$
$$b_{i,j} = \boldsymbol{r}_{i+1,j} \cdot \boldsymbol{t}_{i,j} \tag{2.86}$$
$$d_{i,j}^2 = h_j^2 + \omega_{i,j}^2 \tag{2.87}$$
$$\beta_{i,j} = \frac{\omega_{i,j}b_{i,j}}{d_{i,j}^2 + h_j r_{i+1,j}} \tag{2.88}$$
$$\Lambda_{i,j} = \log\frac{r_{i,j} + r_{i+1,j} + l_{i,j}}{r_{i,j} + r_{i+1,j} - l_{i,j}} \tag{2.89}$$

Two different perspectives remain for the last unknown element of the source intensities σ_j. When using the full velocity decomposition of Equation (2.31), we have seen in Paragraph 2.2.5 that the value of the source distribution σ arises naturally as the predetermined quantity $\sigma(\boldsymbol{y}) = \boldsymbol{n}(\boldsymbol{y}) \cdot \boldsymbol{u}_B(\boldsymbol{y})$ on $\mathscr{S}_B$, i.e. :

$$\sigma_j = \boldsymbol{n}_j \cdot \boldsymbol{u}_B(C_j) \,. \tag{2.90}$$

However when using a source velocity $\boldsymbol{u}_\sigma$ as sole form of velocity contribution outside of the upstream velocity $\boldsymbol{u}_\infty$, the source intensities σ_j must instead be calibrated so as to ensure the verification of the slip condition on the body surface $\mathscr{S}_B$. This condition leads to the formulation of a linear system much akin to that described in Paragraph 1.2.3 for the determination of dipole intensities μ (see Equations (1.35)-(1.38)). The resolution of this linear system gives the values of the discrete source intensities σ_j to be used in the source velocity formulation of Equation (2.74).

2.4.3 Ogami's integral approach

Ogami [86] proposes a method of calculating the potential φ of the complete velocity $\boldsymbol{u}$ on the body surface, independently from the specifics of the velocity computation. The potential is calculated after determining the distribution of surface velocity vectors induced by the surface singularities, the fluid particles, and any other relevant contribution. This is accomplished by "integrating" the velocity directly on the body mesh surface. By definition, the velocity field $\boldsymbol{u}$ and its potential φ are related by the equation :

$$\boldsymbol{u} = \boldsymbol{\nabla}\varphi \ . \tag{2.91}$$

Therefore the potential between two points A and B on the body surface is given by :

$$\varphi_{AB} = \int_A^B \boldsymbol{u} \cdot \boldsymbol{dr} \ . \tag{2.92}$$

The value of this integral is independent of the choice of route between A and B.

This relation is applied using as points A and B the centers C_k and C_{k+1} of each pair of neighboring mesh faces $\mathscr{S}_k$ and $\mathscr{S}_{k+1}$, as shown in Figure 2.7. With M_k the middle point of the common edge separating $\mathscr{S}_k$ and $\mathscr{S}_{k+1}$, we note $\boldsymbol{dr}_k = \boldsymbol{C_k M_k}$ and $\boldsymbol{dr}_{k+1} = \boldsymbol{M_k C_{k+1}}$. Given $\boldsymbol{u}_k = \boldsymbol{u}(C_k)$ and $\boldsymbol{u}_{k'} = \boldsymbol{u}(C_{k'})$ the velocity vectors at the centers of the respective mesh faces, the relation (2.92) can be approximated as :

$$\varphi_{k+1} - \varphi_k \simeq \boldsymbol{u}_k \cdot \boldsymbol{dr}_k + \boldsymbol{u}_{k+1} \cdot \boldsymbol{dr}_{k+1} \ , \tag{2.93}$$

where φ_k and φ_{k+1} denote the velocity potentials at the face centers C_k and C_{k+1}.

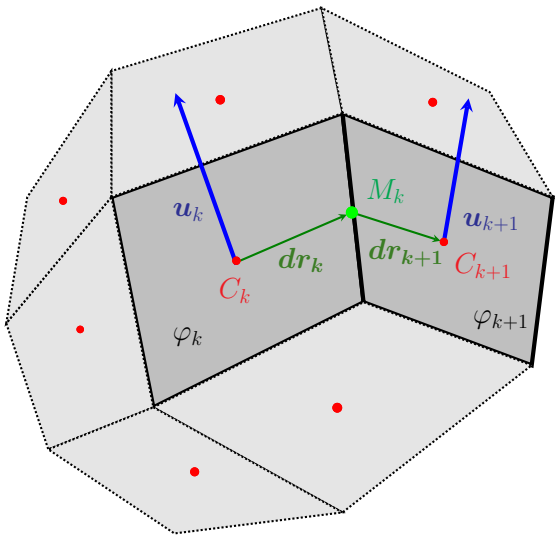

FIGURE 2.7: *Schematic representation of the configuration of neighboring mesh faces used for Ogami's potential computation [86].*

Equation (2.93) is applied to all pairs of neighboring faces on the body surface mesh. If all mesh faces are quadrangular, this will gives us $\dfrac{4N_f}{2} = 2N_f$ relations. These relations can be gathered into a set of simultaneous equations for the unknowns potentials :

$$AX = B \ , \tag{2.94}$$

where the matrix A of size $2N_f \times N_f$ could be for instance :

$$A = \begin{pmatrix} -1 & 1 & 0 & & & \cdots & & 0 \\ -1 & 0 & 1 & 0 & & \cdots & & 0 \\ 0 & -1 & 0 & 1 & 0 & \cdots & & 0 \\ & & & & \vdots & & & \\ 0 & & & \cdots & & 0 & -1 & 1 \end{pmatrix} , \tag{2.95}$$

with the positions of the -1 and 1 on each line depending on the numbering and structure of the mesh faces ; X is the vector formed by the unknowns :

$$X = (\varphi_k)_{k=1}^{N_f} , \tag{2.96}$$

and the right hand side vector B is given by :

$$B = (\boldsymbol{u}_k \cdot \boldsymbol{dr}_k + \boldsymbol{u}_{k+1} \cdot \boldsymbol{dr}_{k+1}) . \tag{2.97}$$

It must be noted that the inversion of the rectangular matrix A require some additional effort compared to the square matrices treated elsewhere in the simulation code. For the time being, this resolution is treated via the `dgelsd` matrix resolution routine of the Fortran90 library Lapack, which computes the minimum norm solution to a linear least squares problem using the singular value decomposition of a rectangular matrix.

2.4.4 Centered alternative

Expanding on this concept, we can then consider further spacing out the face centers used as reference points for the potential calculation. Instead of considering one mesh face and its immediate neighbor, we will now be considering the trio of one quadrangular mesh face and two of its neighbors on opposite sides, as shown in Figure 2.8. As each quadrangular mesh face has 2 pairs of opposing neighbors, the number of equations will remain $2N_f$. We have chosen to refer to this alternative as a "centered" scheme.

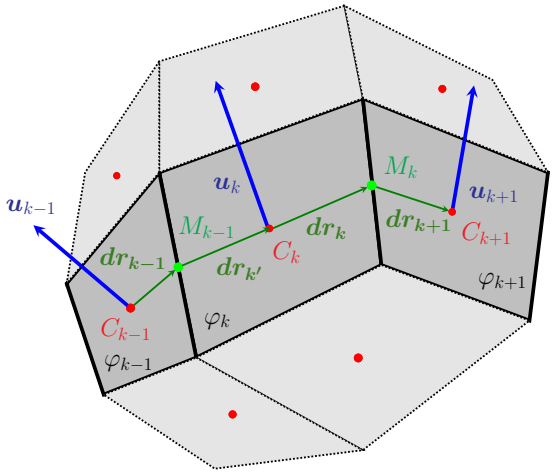

Figure *2.8: Schematic representation of the configuration of neighboring mesh faces used for the alternative potential computation.*

Using the notation shown in Figure 2.8, we now have :

$$\begin{aligned}\varphi_{k+1} - \varphi_{k-1} &= \boldsymbol{u}_{k-1} \cdot \boldsymbol{dr}_{k-1} + \boldsymbol{u}_k \cdot \boldsymbol{dr}_{k'} + \boldsymbol{u}_k \cdot \boldsymbol{dr}_k + \boldsymbol{u}_{k+1} \cdot \boldsymbol{dr}_{k+1} \\ &= \boldsymbol{u}_{k-1} \cdot \boldsymbol{dr}_{k-1} + \boldsymbol{u}_k \cdot (\boldsymbol{dr}_{k'} + \boldsymbol{dr}_k) + \boldsymbol{u}_{k+1} \cdot \boldsymbol{dr}_{k+1} \ .\end{aligned} \tag{2.98}$$

This relation can be expressed similarly to the previous one in the form of a multiplication by a $2N_f \times N_f$ rectangular matrix and subsequently solved for the values of the potentials $(\varphi_k)_{k=1}^{N_f}$.

2.4.5 Calibration of the constant

The previous methods give a solution for the values of the velocity potential on the mesh, up to a constant. This constant is of significant importance, as its value is different each time a new system is solved at each time step of the simulation. This prevents the calculation of the time derivative of the potential needed for the estimation of the pressure as detailed in the next paragraph.

Therefore, an additional step must be included in order to ensure that the potential distribution on the mesh is consistent with a null value of the potential perturbation at "infinity", in order to respect the principle of dissipation at infinity of the disruption caused by the obstacle. In practice, a point is chosen in the flow "far" from the mesh where the value of the perturbation potential is imposed as zero. Thus, the value of the velocity potential at this distant point P is given by the sole potential of the upstream flow velocity $\boldsymbol{U_\infty}$:

$$\varphi_P = \boldsymbol{U_\infty} \cdot \boldsymbol{P} \ . \tag{2.99}$$

A single face of the solid body mesh is chosen as an arbitrary reference point. Let C denote the center of this mesh face. With the value of the velocity potential φ_P at the distant point P being a known quantity, as given by Equation (2.99), the value that the potential φ_C must take at point C can be determined by the relation :

$$\varphi_C - \varphi_P = \int_P^C \boldsymbol{u} \cdot \boldsymbol{dr} \ . \tag{2.100}$$

In order to discretize this relation, the line $\boldsymbol{r} = \boldsymbol{PC}$ joining these two points is divided into N segments $\boldsymbol{X_k X_{k+1}}$, where $X_0 = P$, $X_N = C$, and the number of segments is chosen so that their length $dr = X_k X_{k+1}$ matches as closely as possible the spacial discretization parameter dh : $N = E\left(\frac{PC}{dh}\right)$ and $dr = \frac{PC}{N}$. Figure 2.9 shows a schematic representation of this configuration.

Let φ_k denote the value of the velocity potential and $\boldsymbol{u}^k$ the value of the velocity at each point X_k. The potentials at consecutive points are linked by the relation :

$$\varphi_{k+1} - \varphi_k = \int_{X_k}^{X_{k+1}} \boldsymbol{u} \cdot \boldsymbol{dr} \tag{2.101}$$

$$\simeq \frac{\boldsymbol{u}_k + \boldsymbol{u}_{k+1}}{2} \cdot \boldsymbol{dr} \tag{2.102}$$

$$\Rightarrow \varphi_{k+1} \simeq \varphi_k + \frac{\boldsymbol{u}_k + \boldsymbol{u}_{k+1}}{2} \cdot \boldsymbol{dr} \ . \tag{2.103}$$

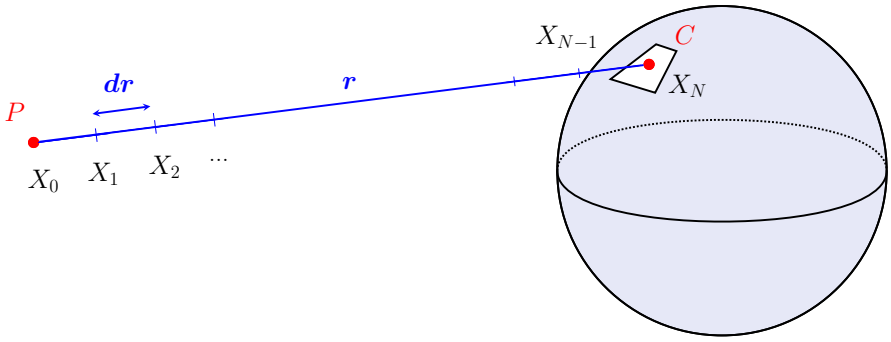

Figure 2.9: *Schematic representation of the calculation of the potential constant to add to the potential distribution on the solid body mesh.*

Finally, we obtain :

$$\varphi_C = \varphi_N \tag{2.104}$$

$$\simeq \varphi_0 + \sum_{k=0}^{N-1} \frac{\boldsymbol{u}_k + \boldsymbol{u}_{k+1}}{2} \cdot \boldsymbol{dr} \tag{2.105}$$

$$= \boldsymbol{U}_\infty \cdot \boldsymbol{P} + \left(\frac{\boldsymbol{u}_0 + \boldsymbol{u}_N}{2} + \sum_{k=1}^{N-1} \boldsymbol{u}_k \right) \cdot \boldsymbol{dr} \ . \tag{2.106}$$

The difference between this velocity potential φ_C calculated to ensure its dissipation at infinity and the value of the potential at the center of this mesh face previously obtained by the resolution of the linear system as prescribed by Ogami gives the value of the constant to be subtracted from the potential previously calculated on each face of the mesh.

2.4.6 Validation on a sphere mesh

These methods are validated on the simple test case of a sphere in an incoming flow. The sphere is fixed and unmoving, and chosen to have a radius of $R = 1$. It is represented by a regular quandrangular mesh, of varying refinements. The surrounding flow has a set velocity of $U_\infty = 1\ m/s$ in the direction of the x axis.

The aim of this test is to validate the implementation of the additional source induced velocity and of the velocity potential, both newly added into the simulation code. In this simple potential flow configuration, no vorticity is shed from the sphere mesh. Therefore there are no rotational component given by fluid particles and no dipole induced potential velocity component to consider. Thus for the sake of this validation only, the velocity field is reduced to the sole contributions of the upstream velocity $\boldsymbol{u}_\infty$ and the source induced potential velocity $\boldsymbol{u}_\sigma$:

$$\boldsymbol{u} = \boldsymbol{u}_\infty + \boldsymbol{u}_\sigma \ . \tag{2.107}$$

In this case, the source intensities $(\sigma_j)_{j=1}^{N_f}$ must no longer be taken as the prescribed values given by Equation (2.90), but rather computed as the unknowns in a system ensuring the validation of the impermeability condition, as evoked in Paragraph 2.4.2.

Figure 2.10 shows this configuration of the resulting flow, confirming the correct verification of the impermeability condition on the sphere mesh.

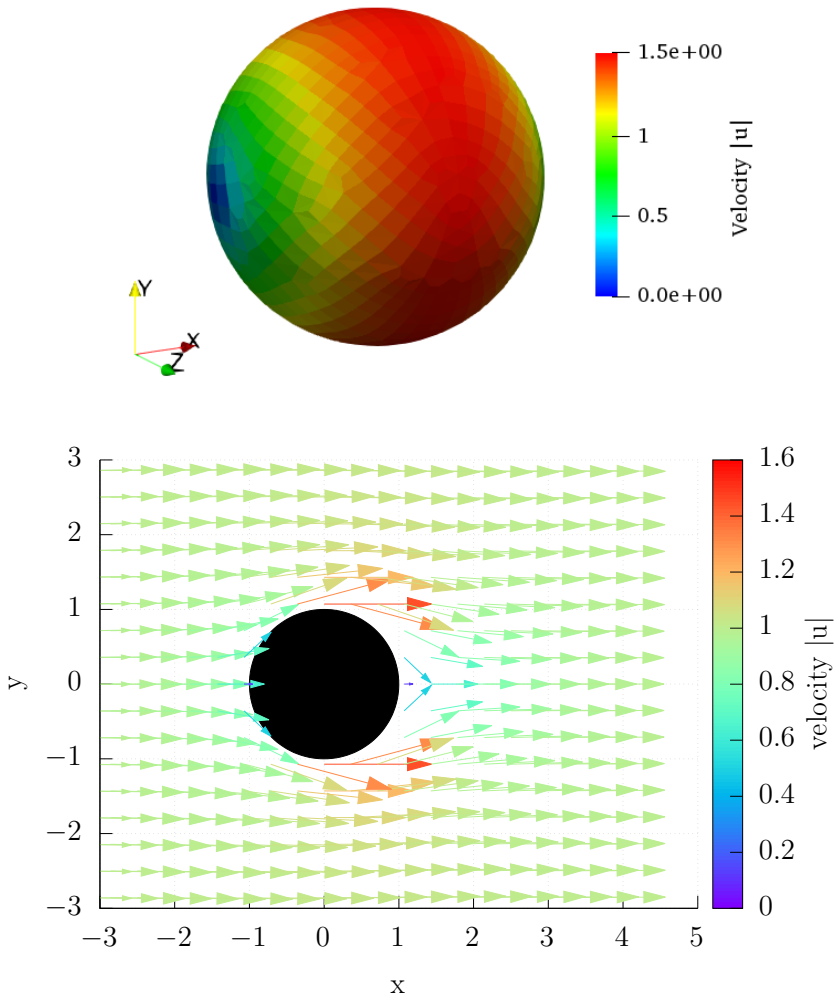

Figure ***2.10:*** *Demonstration of the velocity field resulting of an obstacle sphere in a potential flow, displayed on a section of the surrounding flow and at the centers of the sphere mesh faces.*

Analytical references

Let us consider a sphere of radius R, centered at the origin of the coordinate system, in an incoming flow of velocity $\boldsymbol{U}_\infty = (U_\infty, 0, 0)$ in the direction of the x axis. The potential φ at any point $\boldsymbol{x}$ of coordinates (x, y, z) on the surface of the sphere is given by :

$$\varphi(\boldsymbol{x}) = U_\infty x \left(1 + \frac{1}{2}\frac{R^3}{r^3}\right) + cst \ , \tag{2.108}$$

with $r = |\boldsymbol{x}|$ the distance between the point $\boldsymbol{x}$ and the center of the sphere (see [62]).

The velocity field deriving from this potential is given by $\boldsymbol{U} = (U_x, U_y, U_z)$ with :

$$U_x = U_\infty \left(1 + \frac{R^3}{2r^3} - \frac{3}{2}x^2\frac{R^3}{r^5}\right) \ , \tag{2.109}$$

$$U_y = -\,U_\infty xy\frac{3}{2}\frac{R^3}{r^5} \ , \tag{2.110}$$

$$U_z = -\,U_\infty xz\frac{3}{2}\frac{R^3}{r^5} \ . \tag{2.111}$$

Validation of the velocity potential calculation

We now have at our disposal three methods of calculating the velocity potential on this simple test case :

1. By integrating the velocity between neighboring faces and solving the resulting linear system as shown by Ogami [86]. This method is declined into a decentered integration strictly as performed by Ogami (see Paragraph 2.4.3) or a centered version using faces further removed as a basis for the velocity integration (see Paragraph 2.4.4).
2. By adding the velocity potentials corresponding components making up the velocity : the upstream velocity potential and the potential induced by the distribution of sources, which can be calculated as given by Bousquet [53] based on the values of the source singularities and the geometry of the corresponding mesh faces (see Paragraph 2.4.1).
3. The analytical value of the velocity potential available for this specific configuration (see Paragraph 2.4.6).

In order to validate the source distribution as well as the first two methods of potential calculation, they are compared to each other and to the analytical reference. In this paragraph, the potential computed using these methods will be noted as φ^O for the Ogami, φ^B the Bousquet, and φ^A for the analytical reference.

As the velocity potential can only be calculated to within a constant at the center of each mesh face $\mathscr{S}_i$, these comparisons must take into account the fact that this additive constant will differ from one method to another. For the sake of each comparison, these constants must be computed so as to minimise the distance between the two versions considered.

Let the distance between two points $f = (f_i)_{i=1}^N$ and $g = (g_i)_{i=1}^N$ be defined as :

$$d(f, g) = \sum_{i=1}^{N} (f_i - g_i)^2 \ . \tag{2.112}$$

We must find a constant C so as to minimize the adapted distance :

$$d_C(f,g) = \sum_{i=1}^{N} (f_i - g_i + C)^2 \tag{2.113}$$

We search for an extremum of this function $d_C(f,g)$:

$$\frac{\partial d_C(f,g)}{\partial C} = \sum_{i=1}^{N} \frac{\partial (f_i - g_i + C)^2}{\partial C} = 2\sum_{i=1}^{N} (f_i - g_i + C) = 2N(\overline{f} - \overline{g} + C) \; , \tag{2.114}$$

where $\overline{f} = \frac{1}{N}\sum_{i=1}^{N} f_i$ denotes the average value of f and $\overline{g}$ the average value of g. The above expression reaches its minimum for :

$$C = \overline{g} - \overline{f} \; . \tag{2.115}$$

By applying this result for instance to the potentials φ^O and φ^A at the center of each mesh face i, we have an expression for the minimal distance which will be considered as the error committed on the Ogami based potential calculation :

$$d_C(\varphi^O, \varphi^A) = \sum_{i=1}^{N} \left((\phi_i^O - \overline{\varphi^O}) - (\varphi_i^A - \overline{\varphi^A}) \right)^2 \; . \tag{2.116}$$

The corresponding L_2 error relative to the analytical potential φ^A is given by :

$$Err_{L2}(\varphi^O, \varphi^A) = \sqrt{\frac{d_C(\varphi^O, \varphi^A)}{\sum_{i=1}^{N} (\varphi_i^A - \overline{\varphi^A})^2}} \times 100\% \; . \tag{2.117}$$

Figure 2.11 shows the values of these errors on sphere meshes of increasing refinement and number of faces N. Both Ogami and Bousquet method potentials show a clear convergence of the error compared to the analytical reference as well as between each other with the mesh refinement, all within similar ranges. However the errors committed on the potential calculation do appear to be slightly higher when using the centered version of Ogami's potential integration compared to the decentered version. Bousquet's method leads to better results on the coarsest meshes, while Ogami's decentered version is clearly favored for greater mesh refinements.

In Ogami's article [86], four data points are given representing the L_1 error of his decentered potential computation relative to the upstream velocity U_∞. The L_1 error is recomputed for all cases for comparison with this reference. It is calculated as given by Ogami, adding an account for the constant minimalizing the distance between methods, with for instance :

$$Err_{L1}(\varphi^O, \varphi^A) = \frac{1}{NU_\infty} \sum_{i=1}^{N} \left| (\phi_i^O - \overline{\varphi^O}) - (\varphi_i^A - \overline{\varphi^A}) \right| \times 100\% \; . \tag{2.118}$$

Figure 2.12 shows these errors compared to those given by Ogami. While the errors appear to be of the same general magnitude, they are all more important than those obtained by Ogami. This can be attributed in part to the irregularity of the quadrangle mesh used in these computations compared to Ogami's perfectly regular triangle meshes.

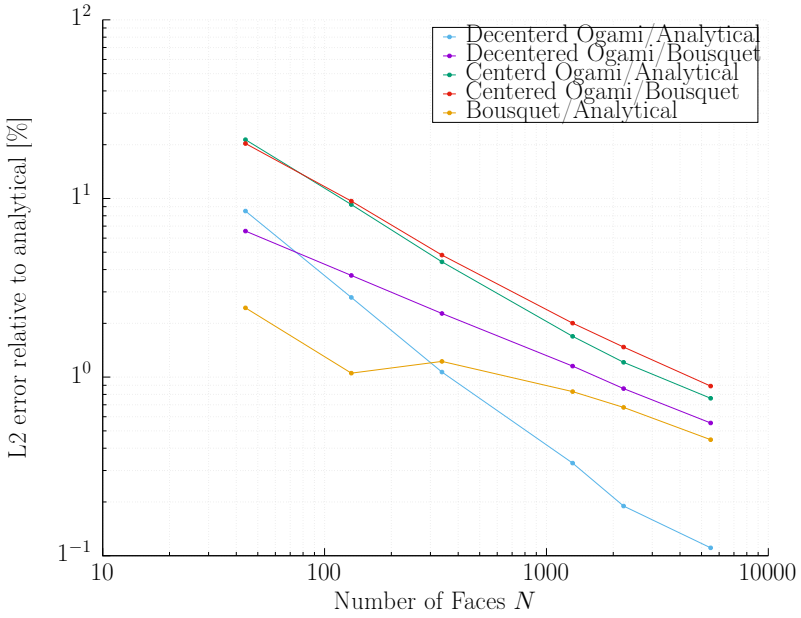

Figure 2.11: *L_2 errors between different version of potential calculations on increasingly refined sphere meshes, relative to the analytical potential.*

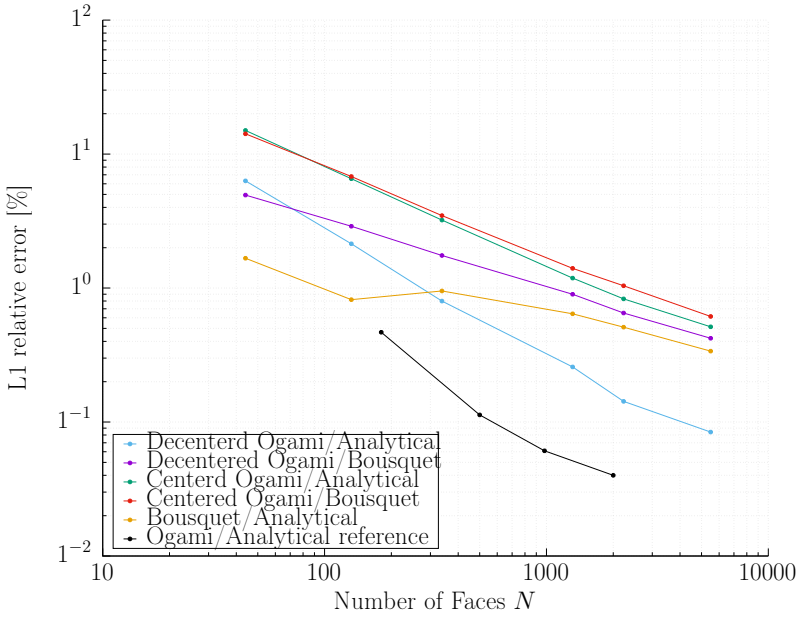

Figure 2.12: *L_1 errors between different version of potential calculations on increasingly refined sphere meshes, relative to upstream velocity U_∞, compared to the results given by Ogami [86].*

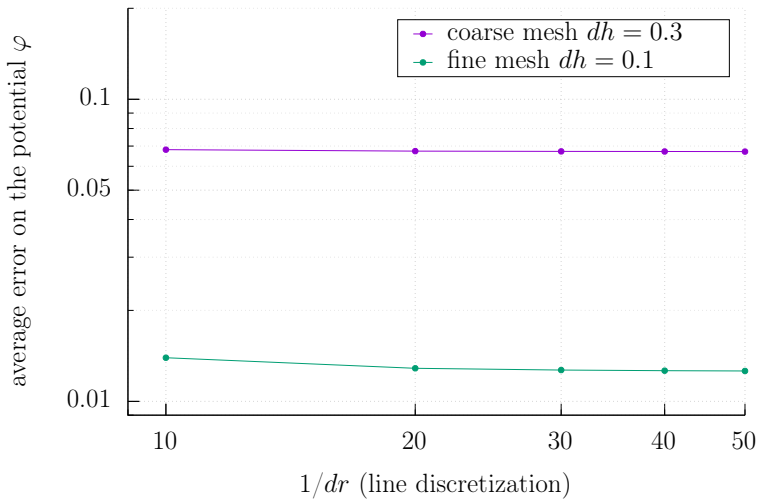

Figure 2.13: *Average error on the potential on the mesh faces for various discretisations of the line along which the potential calibration constant is integrated.*

Validation of the potential calibration constant calculation

Figure 2.14 shows that the error committed on the potential, progressively increasing with the distance to the initial upstream reference point, is a direct consequence of the error committed on the velocity as a result of the discretization, as shown in Figure 2.13.

This concludes the validation of the computation of the velocity potential using Ogami's method on this simplified test configuration, including the addition of the computation of the additive constant which is not mentioned in his article.

2.5 Pressure and force computations

2.5.1 Approximation of the pressure force on the solid body mesh

Pressure calculation

Once the value of the potential φ_k is known on each face k of the solid body mesh, the pressure p_k can be computed using Bernoulli's relation :

$$p_k = -\rho \left(\frac{\partial \varphi_k}{\partial t} + \frac{1}{2} |\boldsymbol{u_k}|^2 \right) \tag{2.119}$$

where $\boldsymbol{u_k}$ is the complete velocity taken at the center of the face k.

The time derivative $\frac{\partial \varphi}{\partial t}$ is approximated on each face k by the uncentered difference :

$$\frac{\partial \varphi_k}{\partial t} = \frac{\varphi_{k|t=t+\Delta t} - \varphi_{k|t=t}}{\Delta t} \tag{2.120}$$

Later on another centered alternative might be considered

$$\frac{\partial \varphi_k}{\partial t} = \frac{\varphi_{k|t=t+\Delta t} - \varphi_{k|t=t-\Delta t}}{2\Delta t} \tag{2.121}$$

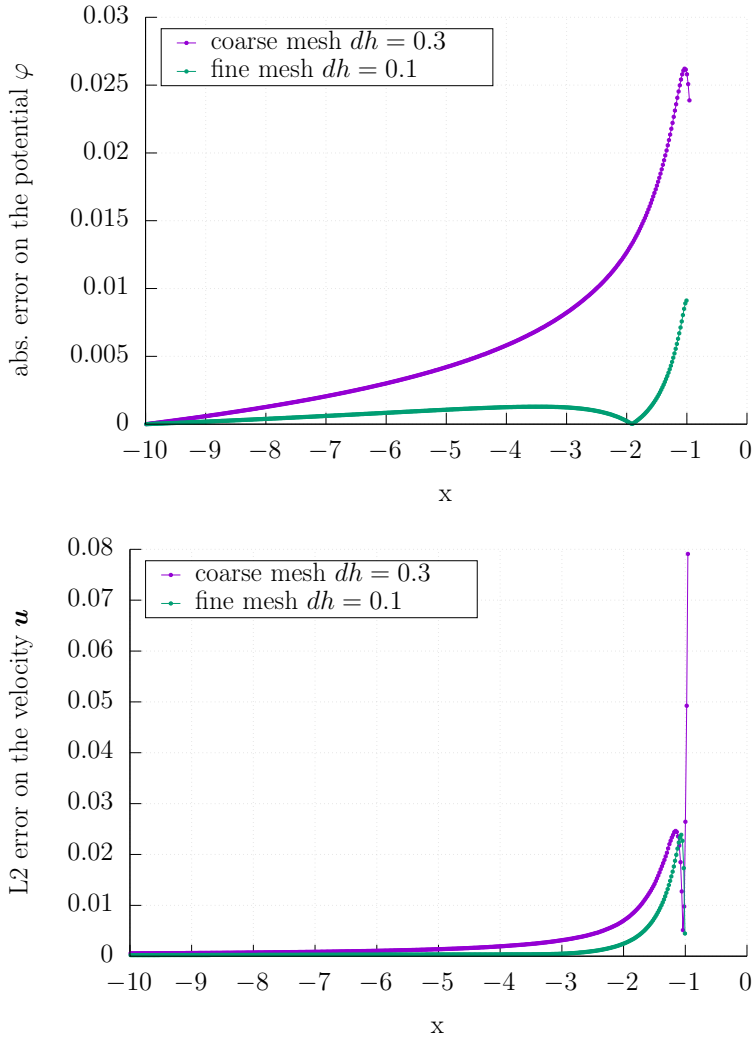

Figure ***2.14:*** *Error committed on the potential and velocity along the integration segment.*

Force calculation

The pressure force $\boldsymbol{F_k}$ applied to the face k of the mesh is obtained by integrating the pressure :

$$\boldsymbol{F_k} = -p_k \boldsymbol{n_k} \Delta_{\mathscr{S}_k} \ , \tag{2.122}$$

with $\Delta_{\mathscr{S}_k}$ the area of the face k.

The pressure force $\boldsymbol{F}$ exerted on the entirety of the solid body then becomes :

$$\boldsymbol{F} = \sum_{k=1}^{N_f} \boldsymbol{F_k} = -\sum_{k=1}^{N_f} p_k \boldsymbol{n_k} \Delta_{S_k} \ . \tag{2.123}$$

2.5.2 Validation of the force calculation on the sphere mesh

In order to validate the implementation of the pressure force calculation, we aim to reproduce the computations on a sphere mesh realized by Ogami [86].

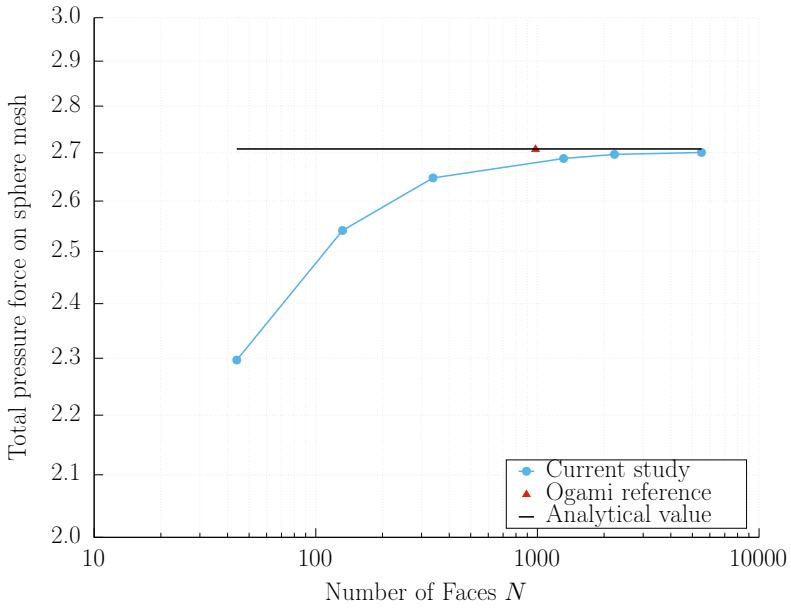

Figure ***2.15:*** *Value of the total pressure force on the accelerated sphere mesh using increasingly refined meshes, compared to the analytical value and the result obtained by Ogami.*

Sphere mesh accelerated through fluid at rest

Consider a sphere accelerated backwards in the direction of the axis $-x$, in a fluid at rest.

Noting $\frac{dU_{\text{sphere}}}{dt}$ the acceleration of the sphere, we expect on its cumulated surface a pressure force of :

$$F = \frac{2}{3}\pi\rho R^3 \frac{dU_{\text{sphere}}}{dt} \ , \tag{2.124}$$

which is equivalent to the added mass for an accelaration $\frac{dU_{\text{sphère}}}{dt} = 1\ m/s^2$. (see [87]).

In order to compare results, we match the parameters used by Ogami :

— density of the fluid : $\rho = 1.293\ kg/m^3$.

— radius of the sphere : $R = 1\ m$.

— acceleration of the sphere (for Ogami in the direction of y) : $\frac{dU_{\text{sphere}}}{dt} = 1\ m/s^2$.

— timestep : $dt = 0.001\ s$.

— 3 iterations, i.e. computation time $t = 0.003\ s$.

Figure 2.15 confirms the convergence of the result towards the analytical value of the pressure force. It can however be noted that we do not reach the value obtained by Ogami even with the higher mesh refinements. This can be explained by the difference in mesh structures. Ogami uses a triangle mesh, which in addition to being perfectly regular and symmetrical also requires less conditions given the lower number of neighbors for each mesh face. The present study uses quandrangular faces, which leads to a less symmetrical and structured mesh and a higher number of conditions for equal numbers of faces. These added conditions and irregularities could contribute slightly more errors on the end result compared to Ogami's computation. It does still remain clear that all approximation errors decrease the higher the number of mesh faces.

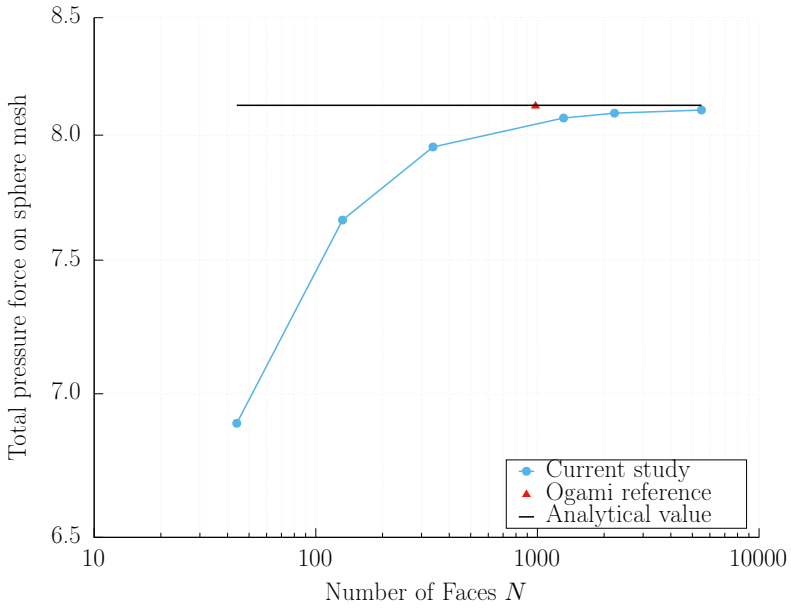

Figure ***2.16:*** *Value of the total pressure force on the unmoving sphere mesh in an accelerated flow, using increasingly refined meshes, compared to the analytical value and the result obtained by Ogami.*

Fixed sphere in accelerated fluid

When the sphere is once again unmoving an the surrounded flow is accelerated by $\frac{\partial U_\infty}{\partial t} = 1$, the pressure force will be :

$$F = 2\pi\rho R^3 \frac{dU_\infty}{dt} \ , \tag{2.125}$$

using all other same parameters as previously (see once again Batchelor's book [62] for reference).

Figure 2.16 shows once again a satisfying convergence towards the expected analytical value, with the same slight discrepancy compared to Ogami's stated result due to the less structured quadrangular mesh used in the present study.

This concludes the validation of the pressure force computation by Ogami's method, using Bernoulli's relation with a potential computed by surface integration of the velocity.

2.6 Conclusion

The aim of the part of the work described within this Chapter was to ascertain and implement the formalism best suited for a better computation of efforts on a fully-rendered turbine representation. After many unsuccessful attempts, we believe to have found a suitable method. While the velocity decomposition using both source and dipole singularity contributions is more commonly used in potential codes, we have made sure to thoroughly justify its derivation in terms of velocity. The emission of fluid particles within this new framework remains near-identical to that already used for the thin blade profile.

To this framework, we have added a recent element of greater interest in the form of a new and simple method for computing the velocity potential and from then on the pressure force. We have attempted to further expand on this aspect of Ogami's proposed

method, by looking into centered scheme alternatives and the computation of the additive potential constant. We have also looked to provide additional material for the validation of the potential and force computations on the same simple test case proposed in his article [86] : namely more detailed comparisons to analytical and source related potential values, as well as confirming a convergence based on mesh refinement.

Once both the velocity decomposition and the computation of efforts have been thus validated, the next step would consist in combining these elements on the target turbine blade. We aimed to present as a demonstration of this method the simulation of a simple turbine blade including its vortical wake and the pressure coefficient around its section consistent with the abundant literature on established airfoils. However we have been met with some hurdles within the simulation code, which we hope to overcome shortly. Nevertheless, the methods exposed here remain of considerable interest, and given their independent validations, are assured to yield compelling results.

Part II

Simulation of ambient turbulence

Chapter 3

Stochastic representation using the Synthetic Eddy Method

This Chapter is replicated from an article published in *Applied Mathematical Modelling* [88]. The initial Section present in this publication has been removed, as it described once more the Vortex Particle Method and its treatment of diffusion, already covered in Chapter 1. The following Sections provide a detailed analysis of the use of the Synthetic Eddy Method in order to account for ambient turbulence, newly implemented into the simulation code.

3.1 Introduction

This Chapter deals with the simulation of ambient turbulence in the framework of the Lagrangian Vortex. Simulation of turbulence is among the most active current research topics as many problems remain unresolved, even with the increase of computational capacities. RANS (Reynolds Average Navier-Stokes), and its unsteady version U-RANS, LES (Large Eddy Simulation) and DNS (Direct Numerical Simulation) are the most frequent approaches to this problem in the Eulerian framework. DNS does not assume any model and therefore is the most reliable method, but its CPU time costs are incredibly high. For the present engineering applications, LES is one of the most popular implementations as it allows the computation of relatively complex and large configurations within a reasonable CPU time. Sagaut [70] presents a review of the different procedures commonly used for Large Eddy Simulation. This LES approach is also possible in the Lagrangian framework : some researchers [71, 89, 90] have already carried out LES computations using the Lagrangian Vortex Method. In their last configuration, Mansfield *et al.* [71] computed a 3D vortex ring collision. Although these computations assessed the influence of turbulence, no ambient turbulence could be taken into account with this approach.

However, in many industrial applications, the ambient turbulence intensity in the upstream flow plays a determining role. This is especially the case in the fields of wind or tidal energy, the latter of which is considered in the present document. Velocity fluctuations induced by ambient turbulence have an impact not only on the performances of an individual turbine, but also on the shape and length of its wake. This is of utmost importance in the design of turbine arrays, when considering the effect of a row of upstream turbines on the power output of any turbines positioned downstream. Experimental studies in potential tidal sites show that this turbulence intensity can range from approximately 3% to 20% [26, 78]. This percentage is calculated from the diagonal components of the Reynolds shear stress tensor and represents a characteristic percentage of the fluctuating velocity

component with respect to the averaged incoming velocity field. Such non-negligible variations in inflow conditions must be taken into account when attempting to replicate numerically the true operating conditions of a tidal turbine.

Therefore, various methods have been developed to emulate the ambient turbulence in the context of Eulerian simulations, through the use of boundary conditions. The Synthetic Eddy Method (SEM) proposed by Jarrin *et al.* [39,91] was initially formulated within this context : its original purpose is to generate inflow conditions for the Eulerian simulation of turbulent flows. Jarrin *et al.* [39] defined a set of turbulent structures to represent a desired fluctuating velocity field at the inlet of their computational domain. This approach was already used by several authors such as Afgan *et al.* [92], or Ahmed *et al.* [5]. As for marine current turbine simulations, Togneri *et al.* [2,93] investigated a similar Synthetic Eddy Method in order to generate synthetic turbulent inflow conditions for their BEMT software. Others use the TurbSim generator from NREL [94] which generates the desired turbulent inflow conditions from a spectral representation of turbulence. For instance, Churchfield *et al.* [21] used TurbSim to generate inflow conditions for their tidal turbine farm computations. Togneri *et al.* [4,95] compare the SEM and spectral based turbulent inflow generation methods in order to investigate fluctuations in loads on the turbine, using their BEMT code. Lastly, Mann's algorithm [96] is another similar approach based on spectral representation of turbulence. Chatelain *et al.* [42,97] used this algorithm to generate a turbulent inflows for wind turbines simulations. The numerical method used by Chatelain *et al.* [42,97] is a particle-mesh method relying on an Eulerian mesh at some steps of the numerical scheme, which allows turbulent flow states to be used as inflow boundary conditions. All these cited approaches share the complication of their difficulty to maintain the chosen inflow ambient turbulence intensity level throughout the whole flow domain. As mentioned by Jarrin *et al.* [39,91], the ambient turbulence intensity usually decreases as the flow progresses, and the desired input level is generally not recovered in the area of interest of the computational domain.

None of these above mentioned methods can be applied as such to a pure Lagrangian Vortex framework, and the adaptation of one of them is the topic of this work. Our numerical model represents the vortical flow field by means of a set of Lagrangian Vortex particles and the velocity field is obtained via the Biot & Savart equation. This Chapter presents an adaptation of the initial SEM method of Jarrin *et al.* which maintains the turbulence intensity level over the entire flow domain, ensured by the advection of turbulent structures with no stretching or diffusion. This can be of major importance for the simulation of wind or tidal turbine farms, to ensure that turbines perceive similar levels of turbulent intensity throughout the entire farm area and all the way downstream to the last row of turbines. Additionally the method presented here can function together with both of the most common treatments of diffusion in Lagrangian Vortex methods, namely the Particle Strength Exchange (PSE) [68,69,98] and the Diffusion Velocity Method (DVM) [74]. These methods can integrate turbulent diffusion models, such as Large Eddy Simulation [71,75,89,90], to better represent all turbulent length scales.

The adapted SEM is presented and analysed on a simple study case. Finally the combination of adapted SEM and Vortex methods is applied to the simulation of a simplified marine current turbine in varying turbulent conditions.

3.1.1 Synthetic Eddy Method for simulating ambient turbulence

The aim of this study is to account for ambient turbulence in the fluid, with any given turbulence parameters and at any point in the study space. The Synthetic Eddy Method formulated by Jarrin *et al.* [39,91] allows the generation of an input flow with

any given turbulent intensity I_∞ and anisotropic ratio (σ_u :σ_v :σ_w). Within Jarrin's initial formulation, these turbulence conditions are only verified at the inlet of the fluid domain. In the present study, this method is adapted in order to cover the entirety of a given study space. The ambient turbulence intensity percentage I_∞ quantifies the velocity fluctuations in a three-dimensional flow (u_∞, v_∞, w_∞) as the following :

$$I_\infty = 100\sqrt{\frac{\frac{1}{3}\left[\sigma^2(u_\infty)+\sigma^2(v_\infty)+\sigma^2(w_\infty)\right]}{\bar{u}_\infty^2+\bar{v}_\infty^2+\bar{w}_\infty^2}} \tag{3.1}$$

In the Synthetic Eddy Method proposed by Jarrin, ambient turbulence in the upstream flow is accounted for by modifying the upstream velocity component $\boldsymbol{u}^\infty$. This upstream velocity is rewritten via the Reynolds decomposition :

$$\boldsymbol{u}^\infty(\boldsymbol{x}) = \overline{\boldsymbol{u}^\infty} + \tilde{\boldsymbol{u}}(\boldsymbol{x}) \tag{3.2}$$

where $\overline{\boldsymbol{u}^\infty}$ is the mean velocity of the flow and $\tilde{\boldsymbol{u}}$ a perturbation term encompassing the fluctuations due to ambient turbulence. The perturbation term $\tilde{\boldsymbol{u}}$ is calculated as the influence of N "turbulent structures", also called "eddies", randomly positioned throughout a three-dimensional study space of volume $\tilde{V}$. Each "turbulent structure" k is characterized by its position $\boldsymbol{x}^k$ and its intensity $\boldsymbol{c}^k$, defined in the following paragraphs. The perturbation induced by N turbulent structures is computed as the sum of the influences of each structure k :

$$\tilde{\boldsymbol{u}}(\boldsymbol{x}) = \sum_{k=1}^{N} \tilde{\boldsymbol{u}}^k(\boldsymbol{x}), \tag{3.3}$$

with $\boldsymbol{x}$ a point of the fluid domain and $\tilde{\boldsymbol{u}}^k$ the perturbation velocity induced by a single turbulent structure k. This individual perturbation velocity is expressed as :

$$\tilde{\boldsymbol{u}}^k(\boldsymbol{x}) = \sqrt{\frac{\tilde{V}}{N}}\boldsymbol{c}^k F_{\boldsymbol{\lambda}}(\boldsymbol{x}-\boldsymbol{x}^k) \quad \forall k \in [\![1,N]\!], \tag{3.4}$$

where $F_{\boldsymbol{\lambda}}$ is a shape function, discussed further below. As for the intensity $\boldsymbol{c}^k$, its three components are defined as :

$$c_i^k = \sum_{j=1}^{3} a_{i,j}\epsilon_{i,j}^k \quad \forall i \in \{1,2,3\}, \quad \forall k \in [\![1,N]\!]. \tag{3.5}$$

All instances of $\epsilon_{i,j}^k$ are random sign variables of values of 1 or -1, representing the random aspect of turbulence. The terms $a_{i,j}$ are the elements of the Cholesky decomposition matrix A of the Reynolds Stress Tensor $\overline{\overline{\boldsymbol{R}}}$:

$$\overline{\overline{\boldsymbol{R}}} = \begin{pmatrix} R_{1,1} & R_{1,2} & R_{1,3} \\ R_{2,1} & R_{2,2} & R_{2,3} \\ R_{3,1} & R_{3,2} & R_{3,3} \end{pmatrix} = \overline{\overline{\boldsymbol{A}}}\,\overline{\overline{\boldsymbol{A}}}^T \quad \text{with} \quad \overline{\overline{\boldsymbol{A}}} = \left(a_{i,j}\right) \tag{3.6}$$

Through Equations (3.5) and (3.6), the link between the intensities $\boldsymbol{c}^k$ of the turbulent structures and the Reynolds Stress Tensor $\overline{\overline{\boldsymbol{R}}}$ ensures the generation of a velocity field that statistically replicates any given turbulence intensity I_∞ and any given anisotropic ratio (σ_u :σ_v :σ_w) [39, 99]. Indeed the three components of the anisotropic ratio (σ_u :σ_v :σ_w) are given by the square roots of the diagonal components of the Reynolds Stress Tensor

$\overline{\overline{\boldsymbol{R}}}$. Moreover the turbulent intensity I_∞ can be rewritten as a function of the trace of the Reynolds Stress Tensor $\overline{\overline{\boldsymbol{R}}}$:

$$\begin{aligned} I_\infty &= 100\sqrt{\frac{1/3\left[\sigma^2(u_\infty)+\sigma^2(v_\infty)+\sigma^2(w_\infty)\right]}{\bar{u}_\infty^2+\bar{v}_\infty^2+\bar{w}_\infty^2}} \\ &= \frac{100}{|\boldsymbol{u}^\infty|}\sqrt{\frac{R_{1,1}+R_{2,2}+R_{3,3}}{3}} \\ &= \frac{100}{|\boldsymbol{u}^\infty|}\sqrt{\frac{\mathbf{tr}\left(\overline{\overline{\boldsymbol{R}}}\right)}{3}} \end{aligned} \tag{3.7}$$

This last Equation (3.7) ensures that the turbulent field will have the desired turbulent intensity I_∞ and anisotropic ratio (σ_u :σ_v :σ_w).

The shape function $F_{\boldsymbol{\lambda}}$ appearing in Equation (3.4) is defined as prescribed by Jarrin *et al.* :

$$F_{\boldsymbol{\lambda}}(\boldsymbol{y}) = \prod_{i=1}^{3} f_{\lambda_i}(y_i). \tag{3.8}$$

$\boldsymbol{\lambda}$ determines the size of the area of influence of each turbulent structure k. This size could be interpreted naively as a turbulent length scale (such as the Taylor or Kolmogorov length scales), but its implementation is not as straightforward. The structure sizes $\boldsymbol{\lambda}$ are a user-defined parameter which can be chosen based on characteristics of the turbulent flow which is to be reproduced. Additional information on the choice of the parameter $\boldsymbol{\lambda}$ can be found in the following Sub-Section 3.2.2. The fact the $\boldsymbol{\lambda}$ is defined as a vector allows the area of influence to have different sizes λ_i in each direction i. Each individual turbulent structure k could also have its own vector size $\boldsymbol{\lambda}_k$, as will also be discussed in the following Sections. The sub-function f_λ used in the evaluation of the shape function $F_{\boldsymbol{\lambda}}$ must meet certain requirements in order to ensure that the ambient turbulence is generated with the chosen characteristics :

$$\underset{y}{\operatorname{argmax}}(f_\lambda(y)) = 0, \tag{3.9a}$$

$$f_\lambda(y) = f_\lambda(-y), \tag{3.9b}$$

$$\int_{-\lambda}^{\lambda} f_\lambda^2(y)dy = 1. \tag{3.9c}$$

These three Equations (3.9a), (3.9b) and (3.9c) are of crucial importance to the proper functioning of the numerical model.

For the preliminary results presented in Section 3.2, a basic shape function $F_{\boldsymbol{\lambda}}$ given by Jarrin *et al.* is used. Its sub-function f_λ is a tent function, here a triangular function centered around zero with a base of 2λ :

$$f_\lambda(y) = \begin{cases} \sqrt{\frac{3}{2\lambda^3}}(\lambda - |y|) & \text{if} \quad |y| < \lambda \\ 0 & \text{otherwise.} \end{cases} \tag{3.10}$$

This basic tent function belongs to the C^0-class functions : it is continuous but its first derivative presents large discontinuities. In the framework of Lagrangian Vortex computations, such discontinuities in the velocity derivatives can be problematic, more specifically for the evaluation of the stretching term S as presented in Paragraph 1.3.1. Following the conditions cited in Equations (3.9a) (3.9b) and (3.9c), smoother alternative shape functions f_λ can be defined. Three examples of class C^1 or more are considered :

— A sinusoidal shape function :

$$f_\lambda(y) = \begin{cases} \frac{1}{\sqrt{3\lambda}} \left(\cos(\frac{\pi}{\lambda} y) + 1 \right) & \text{if } -\lambda \leq y \leq \lambda \\ 0 & \text{otherwise} \end{cases} \tag{3.11}$$

— A polynomial shape function :

$$f_\lambda(y) = \begin{cases} \sqrt{\frac{315}{256\lambda}} \left(\frac{y^4}{\lambda^4} - \frac{2y^2}{\lambda^2} + 1 \right) & \text{if } -\lambda \leq y \leq \lambda \\ 0 & \text{otherwise} \end{cases} \tag{3.12}$$

— A Gaussian shape function :

$$f_\lambda(y) = \begin{cases} c(\lambda) \left(1 - \frac{\exp(1)\ y^2}{\lambda^2} \exp\left(-\frac{y^2}{\lambda^2} \right) \right) & \text{if } -\lambda \leq y \leq \lambda \\ 0 & \text{otherwise} \end{cases} \tag{3.13}$$

where $c\ (\lambda) = \dfrac{1}{\sqrt{L\ (\frac{25}{8} + \frac{3\ \exp(2)\ \sqrt{\pi} * \mathrm{erf}(\sqrt{2})}{16\sqrt{2}} - \exp(1)\ \sqrt{\pi} * \mathrm{erf}(1)\ )}}$.

Figure 3.1a depicts the four kernels for $\lambda = 1$, and Figure 3.1b the Gaussian kernel for different values of λ.

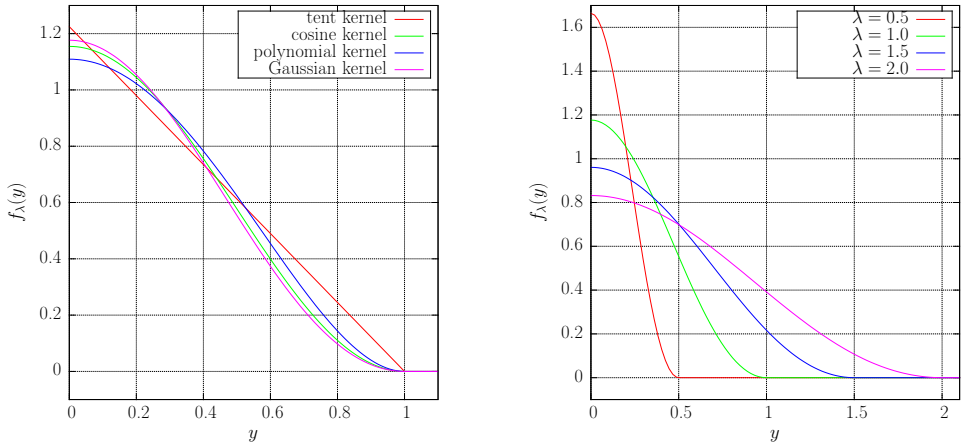

(a) Shape functions f_λ **(b)** Different sizes λ

Figure 3.1: *The four different kernels for $\lambda = 1$ and the Gaussian kernel for different sizes λ of turbulent structures.*

Lastly, the theory of turbulent scales dictates that every turbulent flow contains a wide range of magnitudes of turbulent behavior. Despite its purely mathematical nature, the purpose of this model remains to best represent the true physical phenomenon of turbulent agitation. Thus a standard deviation of the size of turbulent structures, denoted $\sigma(\lambda)$, is added as a parameter of the model. At deviation zero, all turbulent structures k have the same size $\boldsymbol{\lambda}$. A non-zero value of deviation results in a term $\sigma(\lambda)$ being added into the size of each turbulent structure (independantly in each direction $i = 1, 2, 3$), generating turbulent structures ranging in size. The added term $\sigma(\lambda)$ is computed so as to ensure that these sizes are normally distributed around a certain average value : $\lambda \sim \mathcal{N}\ (\lambda,\ \sigma^2(\lambda)\ )$, as illustrated in Figure 3.2. The standard deviation $\sigma(\lambda)$ is expressed as a percentage of

the variable λ, for instance : $\sigma(\lambda) = 10\% = 0.1\ \lambda$. In all cases, this results in a more or less wide spread of turbulent structure sizes, centered around the average given by the initially prescribed values of $\boldsymbol{\lambda}$.

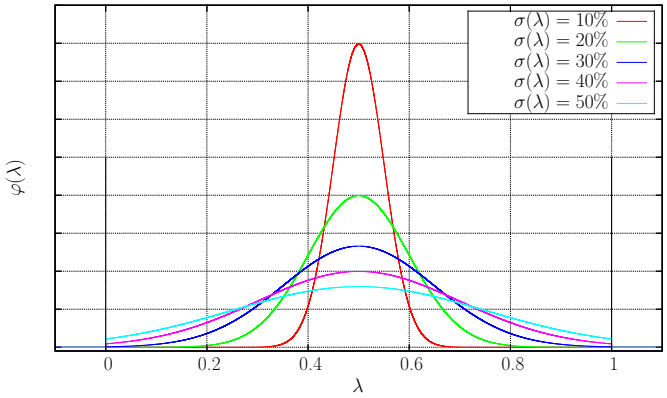

Figure 3.2: *Normal distributions centred around* $\lambda = 0.5$.

If the normal law is not limited, λ could potentially reach negative values, which has no physical meaning. With a heightened value of the standard deviation, it could also lead to the generation of structures of abnormally large size. To solve this problem, boundaries are introduced to the values that λ can take within the prescribed standard deviation. A lower boundary ensures that the size of the turbulent structures can only be positive, while an upper boundary restricts these sizes to under twice the prescribed average value. If the randomly generated size does not meet these criteria, i.e if $\lambda \notin]0 : 2\lambda]$, it is not taken into account and a new structure size is generated. This upper boundary was selected so that the average size of all structures remains substantially equal to the prescribed value λ.

3.1.2 Integration of the Synthetic Eddy Method into the Vortex method

The Vortex Particle Method is an unsteady Lagrangian method in an unbounded domain, where the fluid domain is considered to be infinite. However as mentioned previously, the Synthetic Eddy Method requires the definition of a set volume $\tilde{V}$ containing all the turbulent structures, defined as the volume of a box-shaped space $\tilde{E}$. A second space E_S is considered within $\tilde{E}$ as the actual area of interest inside which the ambient turbulence is desired. In order to obtain statistically correct velocity fluctuations all over the study space E_S, enough buffering space must be left over between $\tilde{E}$ and E_S to ensure the uniformity of the fluctuations all over the area of interest. This can be written as the following conditions :

$$\min\left(x_i \in \tilde{E}\right) \leq \min\left(x_i \in E_S\right) - 2\lambda_i \quad \forall i \in \{1,2,3\}, \tag{3.14a}$$

$$\max\left(x_i \in \tilde{E}\right) \geq \max\left(x_i \in E_S\right) + 2\lambda_i \quad \forall i \in \{1,2,3\} \tag{3.14b}$$

with $\boldsymbol{x}$ a position vector and $\boldsymbol{\lambda} = \lambda_i\,(i = 1,3)$ the size vector of the turbulent structures, as illustrated in Figure 3.3. From this point onwards, in all subsequent Figures the flow direction is represented from the left to the right. The upstream velocity field $\overline{\boldsymbol{u}^{\infty}}$ is shown in the direction of the flow and applied throughout the entire domain E_S.

N turbulent structures k are generated within the chosen space $\tilde{E}$, at random initial positions and of sizes distributed around the average vector size $\boldsymbol{\lambda}$, as discussed in the previous Paragraph. The saturation level of turbulent structures is described by a filling

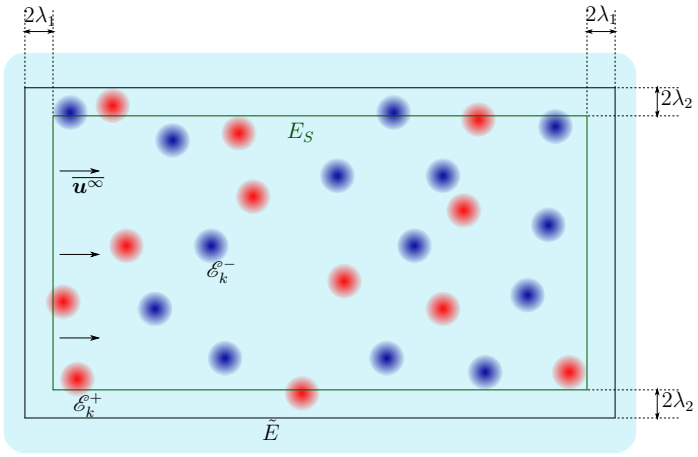

Figure ***3.3:*** *Schematic view of the integration of the Synthetic-Eddy-Method into the Vortex method*

ratio R_f :

$$R_f = \sum_{k=1}^{N} \frac{V_k}{\tilde{V}} \tag{3.15}$$

where V_k is the volume of the area of influence of the structure k (i.e., $V_k = \frac{4}{3}\pi\lambda_1\lambda_2\lambda_3$).

The algorithmic procedure of the SEM progresses as such : each turbulent structure k is characterized at the moment of its generation by an intensity $\boldsymbol{c}^k$ calculated using Equation (3.5), and a random value $\epsilon_{i,j}^k$ with equal probabilities of being 1 or -1. After their initialization, the turbulent structures are advected with the flow as the simulation proceeds. If during the course of the simulation a turbulent structure is advected outside of the boundaries of the space $\tilde{E}$, it is deleted, and replaced by a newly generated structure at the inlet of the space, *i.e.* the leftmost boundary of the schematic representation of Figure 3.3.

Different strategies can be considered for the advection of turbulent structures, with varying levels of coupling and complexity. First of all, the structures can be advected either with the constant average upstream velocity $\overline{\boldsymbol{u}^\infty}$ or with the complete flow velocity $\boldsymbol{u}$. However, if the structures were to be advected with the flow velocity $\boldsymbol{u}$, several questions would arise. As the validity of the Synthetic Eddy Method relies on the randomness of the locations of the turbulent structures, it is unclear whether this property would remain valid if the turbulent structures were advected with a non uniform velocity. Additional tests would need to be carried out in order to ensure that the Reynolds Stress Tensor is still satisfyingly replicated.

Secondly, the added turbulent velocity term $\tilde{\boldsymbol{u}}(\boldsymbol{x})$ could be included in the computation of the stretching and diffusive terms of the Navier-Stokes equation (first and second terms of the right side of Equation (1.4), explicited in Section 1.3). In this preliminary study, the simplest options are selected : advecting the turbulent structures with the constant velocity $\overline{\boldsymbol{u}^\infty}$, and omitting their influence in the calculation of stretching and diffusive terms of the Navier-Stokes equation.

3.2 Numerical reconstruction of turbulent velocity fields

In order to study the turbulent flows generated by the Synthetic Eddy Method and the influence of its various parameters, numerically generated flows are investigated with

basic inflow conditions. Throughout this Section, unless stated otherwise the mean inflow velocity is chosen as $|\boldsymbol{U}^{\infty}| = 1\ m/s$, and the anisotropic ratio as $(\sigma_u : \sigma_v : \sigma_w) = (1 : 0.75 : 0.56)$ based on the observations of Milne *et al.* [26]. For ease of notation, when the average turbulent structure size vector $\boldsymbol{\lambda}$ has the same value in each direction $i = 1, 2, 3$, this size will be referred to as the single value λ (i.e. $\lambda_1 = \lambda_2 = \lambda_3 = \lambda$ or $\boldsymbol{\lambda} = (\lambda, \lambda, \lambda)$).

3.2.1 Analysis of the velocity fields

Figure 3.4 shows examples of turbulent flow fields generated with the Synthetic-Eddy-Method for different values of turbulent intensity I_{∞}. At first glance, these flows appear to be very realistic, with the disruptions to the flow field increasing with the value of the turbulent intensity. The size of the turbulent structures, set to $\lambda = 1$, is not immediately apparent. Figure 3.5 shows the influence of this size parameter, for a fixed value of the turbulent intensity and no variance on the structure sizes. When the turbulent structures are small, each structure can be clearly identified ; whereas when the sizes increase, individual structure shapes are lost in the overlap. Figure 3.6 shows the influence of anisotropy in the set value of turbulent structure sizes $\boldsymbol{\lambda}$, with no variance allowed. The outlined turbulent structures clearly take on a more elongated oval shape as prescribed by their dimensions. Figure 3.7 shows the influence of the variation $\sigma(\lambda)$ allowed around the prescribed average turbulent structure sizes $\boldsymbol{\lambda}$. For higher variations $\sigma(\lambda)$, the shapes of the turbulent structures become increasingly eclectic and diverse, as these variations are independent in each dimension.

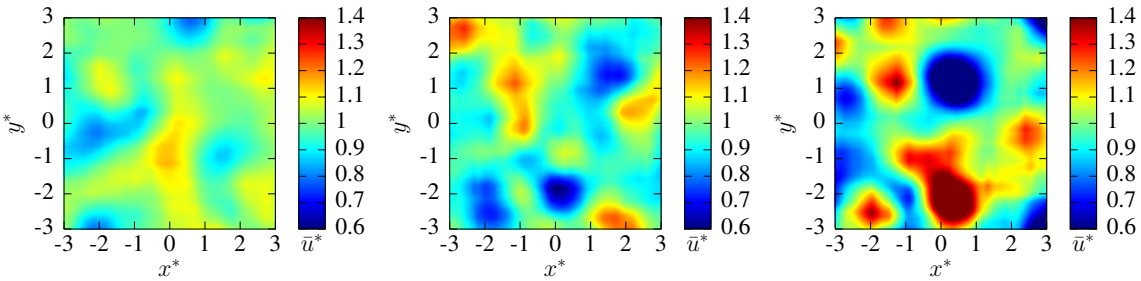

(a) $I_{\infty} = 5\%$ **(b)** $I_{\infty} = 10\%$ **(c)** $I_{\infty} = 15\%$

Figure ***3.4:*** *Examples of velocity fields provided by the Syntehtic Eddy model for* $N = 1000$ *structures of fixed size* $\lambda = 1$ *(*$R_f = 19.4$*) and different values of* I_{∞}*. Slice at* $z = 0$ *of the 3D reconstructed velocity field of size* $6 \times 6 \times 6$*.*

Beyond controlling the appearance of the turbulent velocity fields, the main function of the Synthetic Eddy Method is its ability to reproduce any given Reynolds Stress Tensor. This ensures the correct representation of any given turbulence intensity I_{∞} and anisotropic ratio $(\sigma_u : \sigma_v : \sigma_w)$, as their direct link to the Reynolds Stress Tensor is made clear in Equation (3.7). It is important to verify the accuracy of this reproduction. In order to simplify this verification, one unique quantity is examined : the Turbulent Kinetic Energy (TKE) K as defined by the following Equation :

$$K = \frac{1}{2}(\sigma_u^2 + \sigma_v^2 + \sigma_w^2). \tag{3.16}$$

The value of K is calculated based on the velocity time series recorded at a single point in a turbulent flow, as it would be in the context of an experimental study. To this end, a turbulent space $\tilde{E}$ is built around the sampling point. Turbulent structures evolve within

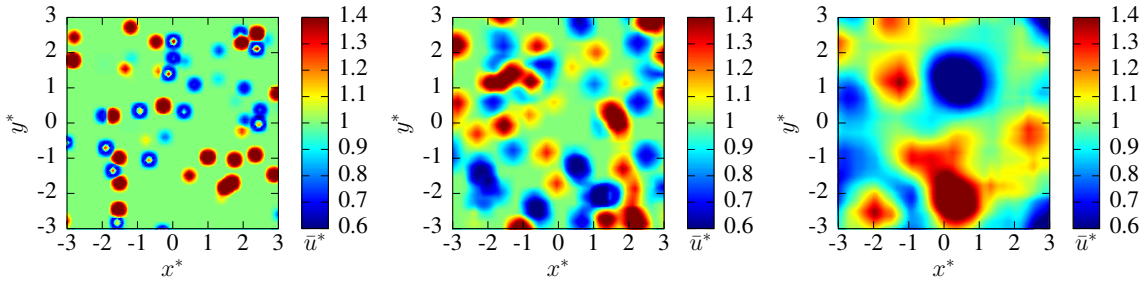

(a) $\boldsymbol{\lambda} = (0.25, 0.25, 0.25)$ **(b)** $\boldsymbol{\lambda} = (0.5, 0.5, 0.5)$ **(c)** $\boldsymbol{\lambda} = (1.0, 1.0, 1.0)$

Figure 3.5: *Example of velocity fields provided by the Synthetic Eddy model for* $I_\infty = 15\%$, $N = 1000$ *structures and different structure sizes (*$R_f = 0.3$, 2.4 *and* 19.4 *respectively). Slice at* $z = 0$ *of the 3D reconstructed velocity field of size* $6 \times 6 \times 6$.

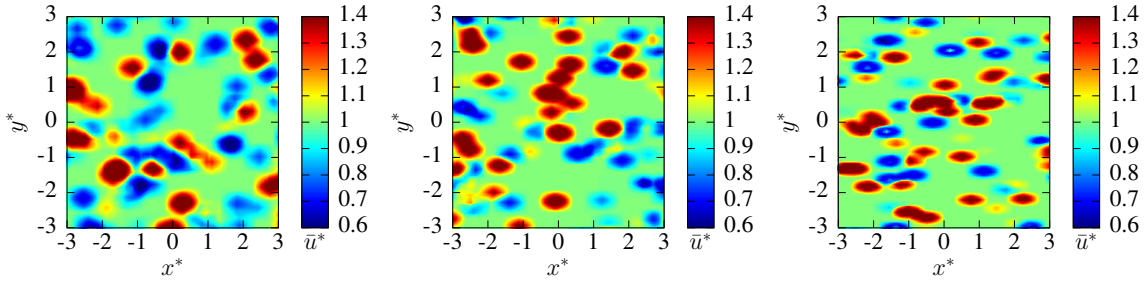

(a) $\boldsymbol{\lambda} = (0.5, 0.4, 0.5)$ **(b)** $\boldsymbol{\lambda} = (0.5, 0.3, 0.5)$ **(c)** $\boldsymbol{\lambda} = (0.5, 0.2, 0.5)$

Figure 3.6: *Example of velocity field provided by the ambient turbulence model for* $I_\infty = 15\%$, $N = 1000$ *structures and different structure sizes (*$R_f = 1.9$, 1.5 *and* 1.0 *respectively). Slice at* $z = 0$ *of the 3D reconstructed velocity field of size* $6 \times 6 \times 6$.

this space, advected with the prescribed upstream velocity of $|\boldsymbol{U}^\infty| = 1\ m/s$. Various parameters are tested, such as the size of turbulent structures $\boldsymbol{\lambda}$, the variation on the size of the turbulent structures $\sigma(\lambda)$, and the filling ratio R_f as defined in Equation (3.15).

Each time series is generated over a simulated period of 12 hours, with a sampling interval of $dt = 0.1$ seconds. Figure 3.8 shows examples of the time series obtained in the "best" and "worse" case scenarios. In the "worse" case, the value of K appears to stabilise eventually at a lower value compared to the target value of 1.35×10^{-3}. As a stochastic method, the SEM is designed so as to ensure an eventual convergence towards this theoretical value. However this convergence is very slow, as there is no evidence of it after 12 hours of simulated time. In this case the filling ratio R_f is low, and since the structures are of larger size λ this means that they are fewer in number. Fewer structures leads to less regeneration of turbulent structures exiting the study space, which causes a slower convergence of the statistical method. Furthermore with the low filling ratio, the sampling point is likely to not be covered by any turbulent structures for a significant part of the time, which explains the lower initial value of K. In the "best" case scenario, the value of K converges and stabilises rapidly at the target value. Due to the probabilistic nature of the Synthetic Eddy Method, these examples of results are not strictly reproducible when repeating the test with the same sets of parameters, but the general tendencies remain.

In order to obtain an accurate representation of the value of K to be expected, 50 time series are computed for each set of parameters. The average and maximal errors on the value of K out of the 50 trials are measured for each set of parameters. Figure 3.9

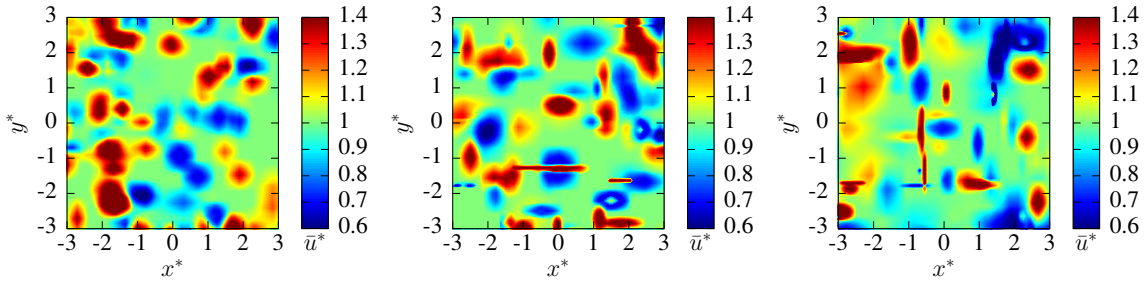

(a) $\sigma(\lambda) = 25\%$ **(b)** $\sigma(\lambda) = 50\%$ **(c)** $\sigma(\lambda) = 100\%$

Figure 3.7: *Example of velocity field provided by the ambient turbulence model for* $I_\infty = 15\%$, $N = 1000$ *structures of average sizes* $\lambda = 0.5$ *and increasing variations allowed around this average* ($R_f = 2.4$). *Slice at* $z = 0$ *of the 3D reconstructed velocity field of size* $6 \times 6 \times 6$.

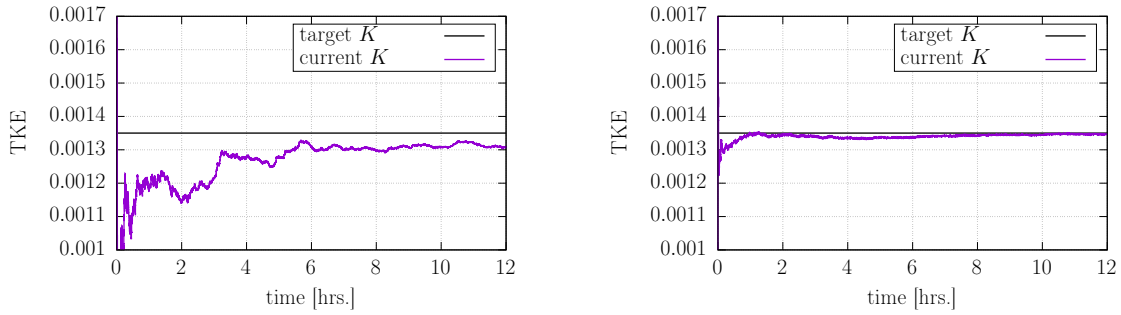

(a) $\lambda = 1$, $R_f = 0.5$ **(b)** $\lambda = 0.25$, $R_f = 10$

Figure 3.8: *Time series of the current values of the TKE* K *computed at a single point over 12 hours of simulated time, for the low turbulence intensity* $I_\infty = 3\%$. *On the left : an example of very slow convergence, with few turbulent structures of large size* λ. *On the right : an example of fast convergence, with a high saturation* R_f *of structures of small size* λ.

shows the average and maximal errors on the reconstructed TKE for different values of the turbulent structure sizes $\boldsymbol{\lambda}$ and filling ratios R_f. For all structure sizes $\boldsymbol{\lambda}$, the average error on the TKE is at its lowest value for the higher filling ratios R_f. Additionally, the relative position of each average error curve shows that the error on the TKE is lower for smaller structure sizes $\boldsymbol{\lambda}$. Figure 3.10 shows the same average and maximal errors on the TKE for different structure sizes $\boldsymbol{\lambda}$, plotted now over a variance $\sigma(\lambda)$ allowed around the average sizes $\boldsymbol{\lambda}$. This graph shows a slight increase in the value of the errors for higher variances $\sigma(\lambda)$. The difference between the curves corresponding to different average sizes $\boldsymbol{\lambda}$ is no longer evident. The blurring of these differences could be explained by the introduction of size variation $\sigma(\lambda)$, meaning that turbulent structures are no longer all of the exact same size $\boldsymbol{\lambda}$ for each curve. In both Figures, the higher and lower turbulent intensity levels show the same general tendencies. The values of the error committed on the TKE are higher for the higher turbulence intensity value $I_\infty = 15\%$. However the value of the TKE is also increased with the higher turbulence intensity, which means that the relative error committed is still comparable.

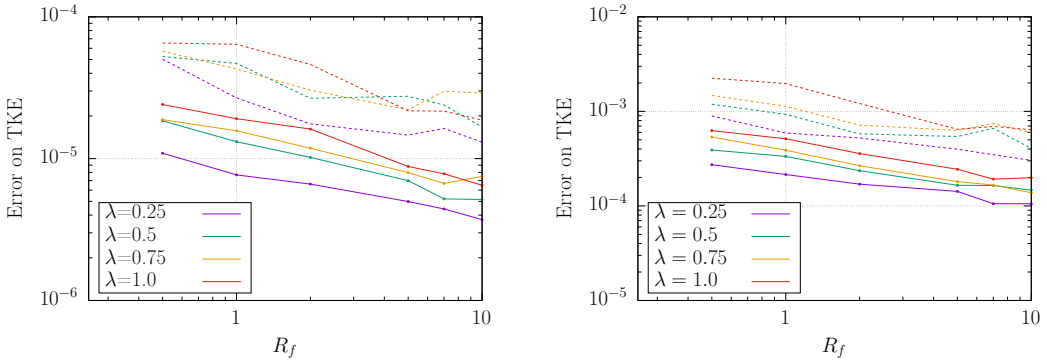

(a) $I_\infty = 3\%$ **(b)** $I_\infty = 15\%$

Figure ***3.9:*** *Average error (full lines) and maximal error (dashed lines) on the value of the TKE K plotted against the filling ratio R_f, for various size of turbulent structures $\boldsymbol{\lambda}$. For both the cases of low turbulence intensity (a) and high turbulence intensity (b) : $\sigma(\lambda) = 0\%$, and the sub-function f_λ uses the Gaussian kernel.*

These tests show that for all sets of parameters, the error committed on the value of the TKE is always satisfyingly low compared to the expected values. However it can be concluded that the Reynolds Stress Tensor is more accurately reproduced when using a high number of turbulent structures of small size $\boldsymbol{\lambda}$. Introducing variation on the sizes of the turbulent structures also slightly disrupts its components.

3.2.2 Physical properties of the flow

In order to pursue the analysis of numerical flows generated by the Synthetic Eddy Method, velocity spectra can also be considered, as is done by Medina [100]. In the following paragraphs, two characteristic physical behaviors of the turbulent flow are analysed. Firstly the time-averaged instantaneous power spectral density (PSD) of the velocity field in the Fourier space illustrates the principle of energy decay in a turbulent flow. Secondly the integral length scale of the flow, also called Taylor macroscale, gives a representation of the size of the generated turbulent structures.

As described in the previous Section, the synthetic turbulence generation method is based on a stochastic algorithm. The statistical properties of turbulent kinetic energy can be described by energy distribution spectra, commonly represented in a logarithmic scale over the wavenumber of the turbulent structures. The concept of energy cascade, as formulated in the work of Richardson and Kolomogorov (see Batchelor [101]), is that kinetic energy enters the turbulent flow at the largest scales to then be transferred to smaller scales, until it is dissipated at the smallest scales by viscous effects. Figure 3.11 illustrates this principle.

The purpose of this study is not to measure the kinetic energy along the wavenumber, but rather to paint a picture of the global behaviour of the kinetic energy in the numerically generated turbulent flow. We focus here on the velocity fluctuations at a single central point in the flow, caused by the presence of N generated turbulent structures, as shown in Figure 3.12. As expected, the axial velocity variation $u^\sigma(t)$ at this point cycles through unpredictable values in an irregular fashion. These variations are caused by turbulent structures passing successively over the measuring point. Each passing structure causes a velocity fluctuation, the amplitude of which depends on the intensity of the turbulent

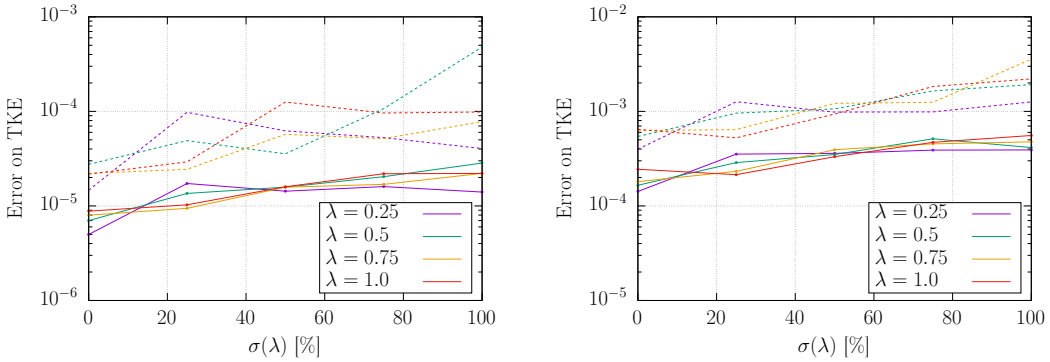

(a) $I_\infty = 3\%$ **(b)** $I_\infty = 15\%$

Figure 3.10: *Average error (full lines) and maximal error (dashed lines) on the value of the TKE K plotted against the variance $\sigma(\lambda)$ allowed around average turbulent structure sizes $\boldsymbol{\lambda}$, for various size of turbulent structures $\boldsymbol{\lambda}$. In all cases : $I_\infty = 3\%$, $R_f = 5$, and the sub-function f_λ uses the Gaussian kernel.*

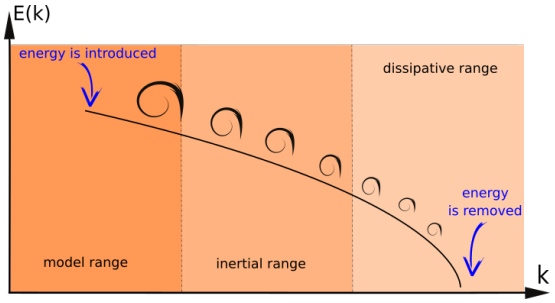

Figure 3.11: *Diagram of the principle of energetic decay $E(k)$ along the wavenumber k*

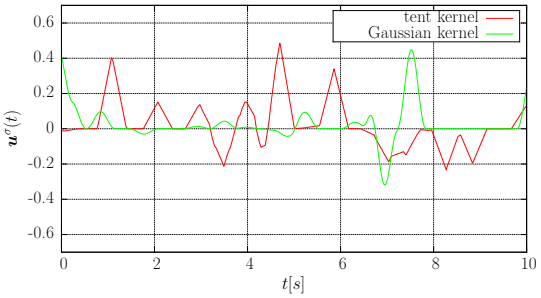

Figure 3.12: *Temporal measurements of velocity fluctuations $u^\sigma(t)$ at one point, for different kernel functions f_λ (with $I_\infty = 15\%$, $\lambda = 0.25$, $\sigma(\lambda) = 25\%$, $R_f = 1$).*

structure and the distance to its center. Distinctive occurrences of the triangle and Gaussian kernels can be identified, indicating the passage of individual turbulent structures close to the measuring point. These temporal records are used to calculate the spectrum, based on the variations in the driving axis of the flow. Figure 3.13 shows the power spectral density for fixed sizes of turbulent structures (i.e. $\sigma(\lambda) = 0\%$), for the four sub-functions f_λ.

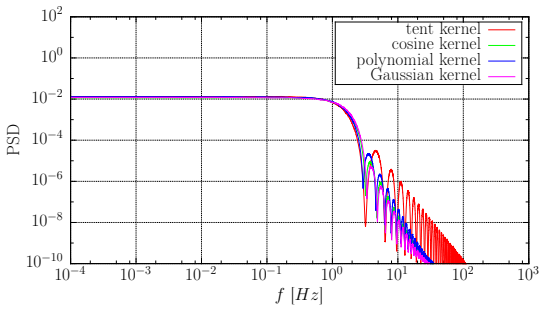

Figure ***3.13:*** *Power Spectral Distribution :* $\lambda = 0.25$, $\sigma(\lambda) = 0\%$

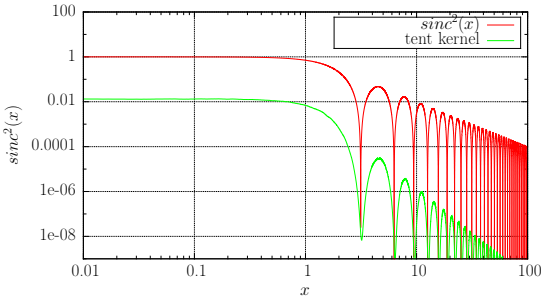

Figure ***3.14:*** *Comparison between* $\mathrm{sinc}^2(x)$ *and the same PSD obtained with the tent kernel*

Although the choice of sub-function alters the pattern of the spectrum, the four curves decrease in similar ways. Additionally, it must be noted that the random nature of the stochastic model can cause each of these curves to slightly vary with repeated simulations. While this figure shows the evidence of a general energy decay, this decay is not linear, but disrupted by recurring "bumps". These "bumps" can be explained by the nature of the Fourier transform used to compute the PSD. In the simplest case of the triangular kernel, the Fourier transform of a triangle function is a well-known result :

$$\Delta(f) = \mathscr{F}\ (T_{riangle}(t)) = \mathrm{sinc}^2(f). \tag{3.17}$$

As a sum of triangle functions of identical width λ, the velocity signal is transformed into a sum of proportional square cardinal sinus functions. Figure 3.14 verifies the alignment of the square cardinal sinus function with the calculated PSD.

When the standard deviation $\sigma(\lambda)$ on the size of turbulent structures is nonzero, the flow is filled with a range of structures of different sizes. This affects the energy decay represented by the PSD, as shown in Figure 3.15. The Fourier transform of the new velocity signal becomes a sum of "bumpy" elements which do not align, leading to a smoother and more realistic curve. This PSD appears to converge with respect to the variation $\sigma(\lambda)$ as of $\sigma(\lambda) = 75\%$, towards a quasi-linear energy decay. The quality of the PSD curves obtained with sufficient variation on the size of the turbulent structures is further validated by comparison with experimental spectra provided by Medina *et al.* [102]. While the correspondence between numerical and experimental data is not complete, the similarities between these curves is sufficient to conclude that the SEM is capable of accurately representing the energy behaviour of a real turbulent flow. At this point, it is worth remembering that the smaller the variation $\sigma(\lambda)$, the better the convergence of the numerical TKE towards the target value (see Fig. 3.10 above). Therefore, for further applications, a trade-off will have to be made when weighing the importance of both these elements in the choice of the parameter $\sigma(\lambda)$.

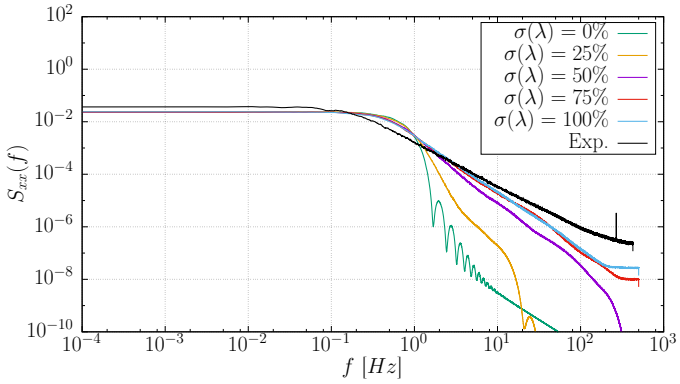

Figure ***3.15:*** *Influence of $\sigma(\lambda)$ on the spectral representation for a Gaussian kernel ($\lambda = 0.5$ and $R_f = 2$) and comparison with experimental data provided by Medina* et al. *[102] (for $I_\infty = 15\%$ and $U_\infty = 0.8\ m/s$).*

True physical turbulent motions occur over a wide range of time and length scales, with the largest scales accounting for the largest transports of momentum and energy. As a second physical analysis of the numerically generated turbulent flows, we attempt to liken the spatial scale of the turbulent behavior to the prescribed sizes λ of the turbulent structures. There are many possible methods to measure the scales of turbulent behavior in a given flow. Among these measures, the Taylor macroscale $\mathscr{L}$ gives an estimate of the characteristic size of turbulent eddies. $\mathscr{L}$ is calculated using the autocorrelation method based once again on the fluid velocity measured at a single point over a period of time :

$$\mathscr{L} = \overline{u} \int_0^\infty R(\tau)\mathrm{d}\tau, \tag{3.18}$$

with $R(\tau)$ the autocorrelation function. In the present case of a statistically stationary process, the autocorrelation is defined as a function of the time lag τ :

$$R(\tau) = \langle u(t)\ u(t+\tau) \rangle \tag{3.19}$$

The value of the autocorrelation begins at 1 and then decays with increasing time lag τ,

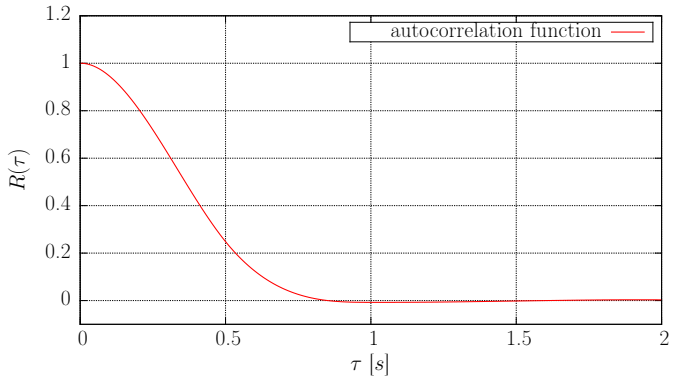

Figure ***3.16:*** *Sample plot of an autocorrelation function $R(\tau)$ calculated with the numerically generated velocity field*

as shown in Figure 3.16. As the turbulent velocity fluctuations are randomly generated, the autocorrelation converges towards zero.

The characteristic length $\mathscr{L}$ of the flow is calculated for varying turbulent structure sizes λ, at first with no variance $\sigma(\lambda)$ allowed. The results displayed in Figure 3.17 show near-perfect linear relationships obtained between the prescribed sizes λ and the resulting turbulent spatial scales $\mathscr{L}$, for all types of kernel sub-functions f_λ. The turbulent scales $\mathscr{L}$

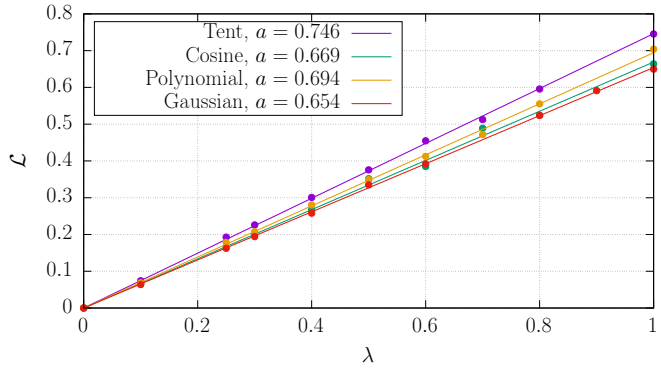

Figure 3.17: *Linear relation between $\mathscr{L}$ et λ using different kernel functions f_λ.*

are then recalculated with the introduction of variances $\sigma(\lambda)$ around the average structure sizes λ. Table 3.1 shows that this results in only small disruptions of the value of the scale $\mathscr{L}$. It can thus be assumed that with or without variation on the size λ of the turbulent structures, λ is proportional to the scale of the turbulent behavior in the generated flow.

$\sigma(\lambda)$ (%)	0	25	50	75	100
$\mathscr{L}$ $(\lambda = 0.25)$	0.163	0.163	0.162	0.162	0.169
$\mathscr{L}$ $(\lambda = 0.5)$	0.330	0.336	0.310	0.327	0.328
$\mathscr{L}$ $(\lambda = 0.75)$	0.496	0.478	0.474	0.486	0.518

Table 3.1: *Influence of the variation on the structure sizes $\sigma(\lambda)$ on the value of the Taylor macroscale $\mathscr{L}$ with $R_f = 1$ and the Gaussian kernel.*

3.3 Application to marine current turbine simulation

The properties of turbulent flows generated by the SEM have been thoroughly studied in the absence of turbines. As an illustrative application of the adapted SEM, two simplified turbine simulations are carried out with turbulent intensities I_∞ ranging from 0 to 15%. Though the results are qualitative, they demonstrate the influence of the ambient turbulence created using the adapted SEM throughout the surrounding flow. The aim of this trial is to reproduce the behavior observed in experimental studies, such as Mycek *et. al* [78].

These simulations are carried out with a simplified turbine model : only the three turbine blades are represented. The geometry and specifications of the turbine blades used in these simulations are those of the IFREMER-LOMC turbine model used in [78]. In these computations, in addition to the SEM module presented here, the diffusion model described in Paragraph 1.3.2 (PSE method using an LES formulation) is used to account for an eddy viscosity affecting the Lagrangian Vortex particles. 90 to 120 seconds of physical time are simulated, and velocity averages are post-treated over the last 50 to 80 seconds once the turbine wake is stabilised. The velocity component $\tilde{u}$ produced by the SEM, as

mentioned in Equation (3.2), is omitted from this post-treatment, in order to emulate the effect of a longer time average. With a longer time average, this fluctuating component would even itself out and have no influence on the averaged end result. In all cases, the average upstream velocity remains at $U_\infty = 1\ m/s$ and gravity was neglected. Two turbine rotation speeds are considered, characterized by Tip Speed Ratios $TSR = 2.5$ and $TSR = 3.67$ ($TSR = \frac{\Omega R}{U_\infty}$, with Ω the rotation speed and R the radius of the turbine).

The study space E_S in which the SEM is applied is extended to 1 turbine diameter upstream of the turbine center, 3 diameters above and below, and 12.5 diameters downstream. Experimental data for later comparison is only available up to the cutoff of 10 diameters downstream of the turbine. This allows the wake to be artificially dissipated later on, in order to maximize computational efficiency. The same basic set of SEM parameters is used to obtain the Figures presented hereafter : $\lambda = 0.5$, $\sigma(\lambda) = 0$, and $R_f = 1$.

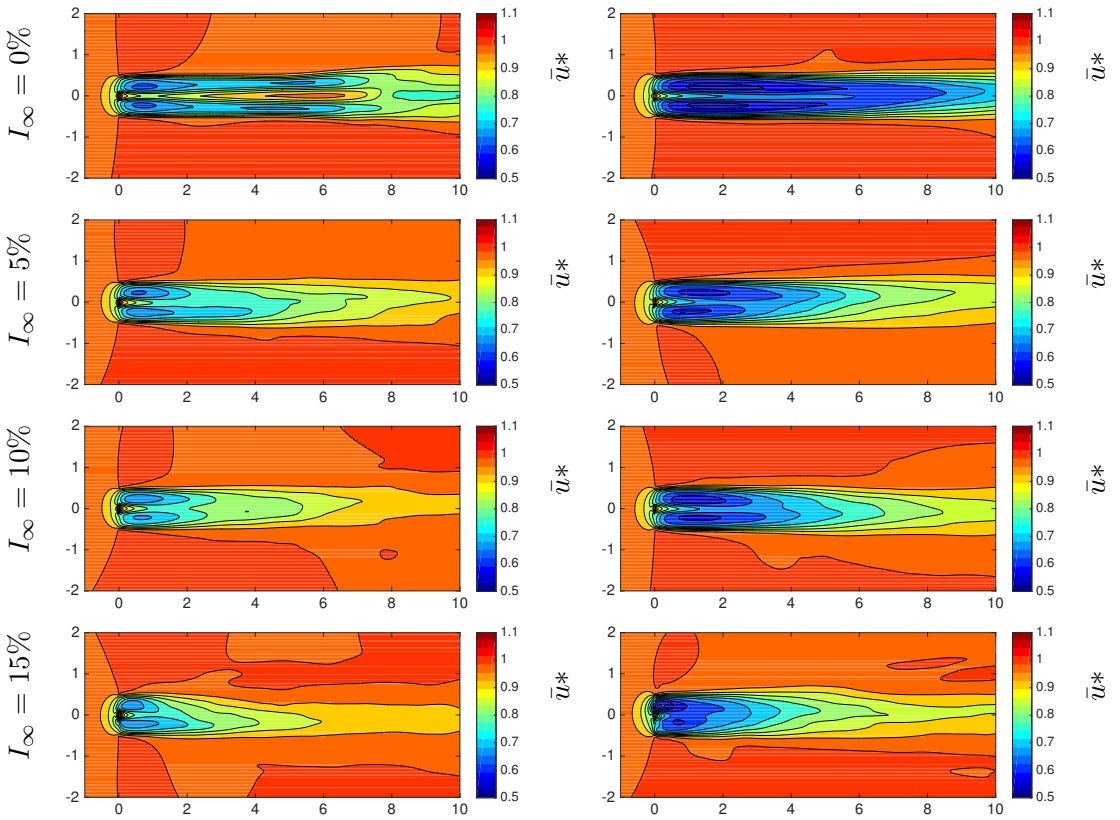

(a) $TSR = 2.5$ (b) $TSR = 3.67$

Figure ***3.18:*** *Velocity maps in the wake of a single turbine, averaged over a period of 50 to 80 seconds, for varying levels of turbulent intensity. The x and y axis were made dimensionless with respect to the turbine diameter D. $\bar{u}^*$ stands for the dimensionless velocity field and is defined as $|\bar{u}|/U_\infty$.*

Figure 3.18 shows dimensionless velocity maps of turbine wakes obtained in these conditions for varying turbulent intensities I_∞. Despite the evidence of the missing hub in the form of a heightened velocity at the center of the wake, satisfying tendencies can be observed. First of all, in the absence of ambient turbulence, the turbine wakes extend to approximately 10 diameters downstream of the rotor, which is the correct behaviour expected in low turbulence conditions [103]. Secondly, when using and progressively increa-

sing the ambient turbulence intensity generated by the SEM, the turbine wake becomes progressively shorter. This is further evidenced when considering the velocity deficits integrated in the wake of the turbine. By the relative positioning of the velocity deficit curves, Figure 3.19 confirms the ever faster wake recovery as the turbulent intensity is increased. For instance for the case of the lower rotation speed $TSR = 2.5$, the velocity in the wake of the turbine reaches the ratio of 0.9 times the upstream velocity U_∞ at approximately 3.5 diameters downstream of the turbine with the highest turbulence intensity $I_\infty = 15\%$, 7.5 and 5 respectively for turbulence intensities of $I_\infty = 10\%$ and 5%, a value which is not reached within the study space with no turbulence intensity. Computational times were increased by 100 to 200% when using the SEM ambient turbulence generation module with the aforementioned parameters, with respect to the basic case run using no ambient turbulence $I_\infty = 0\%$. For base computational times of approximately 10 hours with 252 cores, the additional CPU cost of this development is not considered to be critical considering the advantages it procures. And a better integration, especially with respect to load balance in the parallel MPI framework, is much probably possible that may drastically diminish this increase.

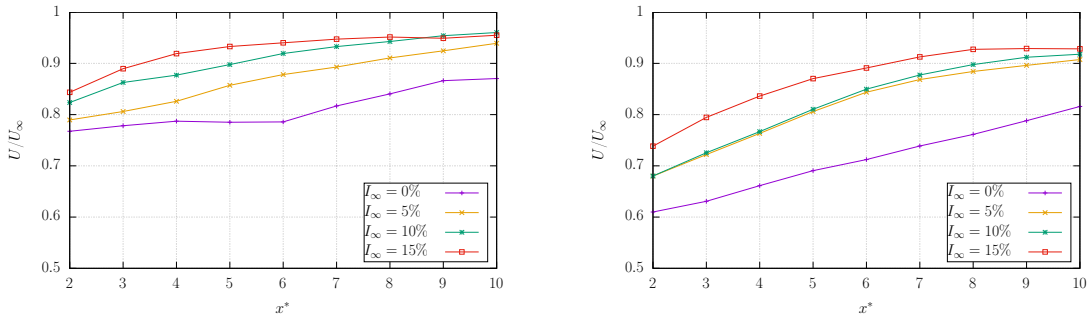

(a) $TSR = 2.5$ **(b)** $TSR = 3.67$

Figure ***3.19:*** *Velocity integrated in the wake of a single turbine, on a disc of the same width as the turbine and at given distances downstream of its centre. These curves are produced using the numerical wake velocities shown in map form in the previous Figure.*

The Synthetic Eddy Method thus proves its compatibility with the full marine turbine Vortex simulation software. In addition to its ability to reproduce physical properties of experimental flows, it can also have the correct influence on the wake of the turbine, in the form of the shortening of its wake, also observed in experimental studies conducted at IFREMER [78]. It must however be noted that some sets of turbulent parameters may lead to less satisfying results (not presented here) : large turbulent structures tend to not have sufficient mixing properties, while small structures may cause important and non physical velocity fluctuations, and a number of any size of turbulent structures can have a strong dissipative effect on the wake regardless of turbulence level.

3.4 Conclusions and Further work

The Synthetic Eddy Method (SEM) initially proposed by Jarrin *et al.* [39] [91] is successfully adapted to the Lagrangian Vortex framework. The present implementation gives satisfying results regarding the important role played by the ambient turbulence intensity in the behavior of turbine wakes. To the authors' knowledge, this work represents

one of the first attempts to account for ambient turbulence in a purely Lagrangian Vortex representation.

The present ambient turbulence model is able to generate a perturbed flow verifying any given turbulence intensity I_∞ and any anisotropic ratio (σ_u :σ_v :σ_w). The study of the Power Spectral Densities (PSD) shows that the introduction of a variation in the sizes of the turbulent structures smoothes the PSD curve of the perturbed flow. This allows for the reproduction of an energy cascade scheme close to experimental measures taken in real turbulent flows. Measuring the Taylor macroscale in the generated flows shows that the scale of the turbulent behavior depends exclusively on the prescribed turbulent structure sizes. For each considered kernel shape function, there exists a remarkable linear relationship between these two quantities.

As an application example, the compatibility of this method with a Vortex code for the simulation of turbine wakes is verified. The results show that for certain turbulence parameters, the qualitative influence of the turbulent intensity can be accurately reproduced : the turbine wake is dissipated sooner the higher its value.

A limitation of this present implementation of the Synthetic Eddy Method lies in the fact that the added perturbation term is not divergence-free. However for the turbulent intensities considered here, the error introduced in the flow poses no considerable issue. Further work is needed in order to reformulate the velocity perturbation term $\tilde{\boldsymbol{u}}$ in a way that is better compatible with the present Vortex formulation. The divergence-free alternative implementation of the SEM suggested by Poletto *et al.* [104] is under consideration in the pursuit of this study, as their rotational representation of the perturbation velocity could be better suited to the Lagrangian Vortex framework.

Another avenue of investigation lies in the degree of integration of the perturbation velocity $\tilde{\boldsymbol{u}}$ in the Lagrangian algorithm. In the present implementation, it is only added in the advection step but it could also be integrated into the stretching step or even the diffusion step when using the Diffusion Velocity Method (DVM). This increased integration could be valid for both Jarrin's initial formulation and Poletto's more recent version.

Even in the form of this initial investigation, this new implementation possesses the important advantage over its Eulerian counterparts of allowing the ambient turbulence level to be maintained throughout the entire computational domain, regardless of its size. This is of a crucial importance when considering an array of tidal turbines, to ensure that the same levels of upstream ambient turbulence are perceived by rows of turbines positioned anywhere in the array. This represents a significant step towards the final goal of computing an entire farm of turbines in any realistic operating conditions.

Chapter 4

Divergence free adaptation of the Synthetic Eddy Method

4.1 Introduction

As described in the previous Chapter, the Synthetic Eddy Method (SEM) uses randomly positioned eddies to generate a perturbation term $\tilde{\boldsymbol{u}}$ added to the upstream velocity term $\boldsymbol{u}_\infty$ as the fluctuationg part of its Reynolds decomposition (see Equation (3.2)). It is able to generate velocity fluctuations $\tilde{\boldsymbol{u}}$ guaranteed to reproduce any given Reynolds stress tensor, via the use of the coefficients of its Cholesky decomposition along with an appropriate shape function, as formulated in Equations (3.3) and (3.4).

In his PhD thesis [46], Poletto aims to create an alternative form for the velocity fluctuations of Equation (3.4) which in addition to the reproduction of the Reynolds stress tensor would also ensure a divergence free velocity field. His method, dubbed Divergence Free Synthetic Eddy Method (DFSEM), uses the same framework as the SEM : a collection of turbulent structures, initially randomly placed and then progressing throughout a given study space, each having an individual area of influence. However in this new DFSEM, the turbulent structures are reshaped and the perturbation velocity reformulated in order to ensure a divergence free velocity field respectful of the base incompressibility condition of Navier-Stokes' equations.

After an overview of the reasoning leading to Poletto's suggestion for a divergence free turbulent velocity formulation, this Chapter will detail the aforesaid formulation. As performed in the previous chapter for Jarrin's original SEM, the reproduction of various turbulent field characteristics with Poletto's DFSEM will be verified, as well as its behavior when interacting with the wake of turbine blades.

A more detailed account of the mathematical derivation of Poletto's formulation can be found in his PhD thesis [46].

4.2 Poletto's formulation

In this divergence free adaptation of the original SEM, the same basic framework is used as presented previously in the previous Chapter. A chosen number of turbulent structures are placed randomly within a given study space, advected with the average upstream velocity, and replaced at the inlet of the study space as the simulation progresses. Each of these turbulent structures generates a disruption to the velocity field in an area of influence surrounding its center. The particulars of this disruption are given by a formulation for

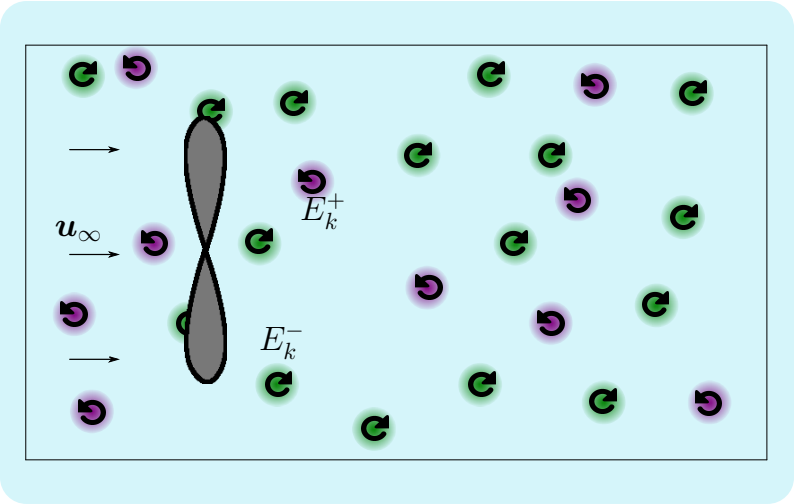

Figure *4.1: Schemtic representation of the turbulent structures immersed in the incoming flow.*

the perturbation velocity, now more closely related to a true "eddy" formulation than the SEM's velocity sources and sinks, and modulated by a shape function. Figure 4.1 shows the new representation of this situation. The combination of these elements is expected to verify the following conditions :

— must be divergence free.
— must ensure the reproduction of a given Reynolds Stress Tensor (which guarantees the reproduction of any prescribed turbulent intensity and anisotropic ratio).

This Section presents an overview of the reasoning followed by Poletto in order to obtain these elements, leading to the formulation for the DFSEM added turbulent perturbation velocity noted once again $\tilde{\boldsymbol{u}}$. For a better understanding of the somewhat delicate mathematical processes involved in this derivation, see Chapter 6 of Poletto's thesis [46].

4.2.1 From vorticity to velocity

Poletto's reformulation of the perturbation velocity is obtained by applying fluctuations similar to those used in the SEM framework to the vorticity field rather than the velocity. The vorticity field thus obtained can then be integrated into a divergence free velocity field (as suggested by Winckelmans and Leonard [60]). These vorticity fluctuations are given by :

$$\tilde{\boldsymbol{\omega}}(\boldsymbol{x}) = \sqrt{\frac{1}{N}} \sum_{k=1}^{N} \boldsymbol{c}^k F_\lambda(\boldsymbol{x} - \boldsymbol{x}^k) \,, \tag{4.1}$$

with N the number of turbulent structures k, λ the prescribed sizes of turbulent structures, and $\boldsymbol{c}^k$ and F_λ a structure intensity and an appropriate shape function which have yet to be defined in this context.

In order to obtain a divergence free velocity field $\tilde{\boldsymbol{u}}$ corresponding to this vorticity, we begin from the vector calculus identity :

$$\begin{aligned} \boldsymbol{\nabla} \times \tilde{\boldsymbol{\omega}} &= \boldsymbol{\nabla} \times (\boldsymbol{\nabla} \times \tilde{\boldsymbol{u}})) \\ &= \boldsymbol{\nabla}(\boldsymbol{\nabla} \cdot \tilde{\boldsymbol{u}}) - \Delta \tilde{\boldsymbol{u}} \,. \end{aligned} \tag{4.2}$$

Under the hypothesis of a divergence free velocity field $\boldsymbol{\nabla}\cdot\tilde{\boldsymbol{u}}=0$, this leads to the Poisson equation :

$$\Delta\tilde{\boldsymbol{u}} = -\boldsymbol{\nabla}\times\tilde{\boldsymbol{\omega}}\ , \tag{4.3}$$

of which a solution is given using the Biot Savart kernel :

$$\tilde{\boldsymbol{u}}(\boldsymbol{x}) = \int_{\boldsymbol{y}\in\mathbb{R}^3} \boldsymbol{K}(\boldsymbol{x},\boldsymbol{y})\times\tilde{\boldsymbol{\omega}}(\boldsymbol{y})dy \tag{4.4}$$

$$= \sqrt{\frac{1}{N}}\sum_{k=1}^{N}\int_{\boldsymbol{y}\in\mathbb{R}^3} \boldsymbol{K}(\boldsymbol{x},\boldsymbol{y})\times\left[\boldsymbol{c}^k F_\lambda(\boldsymbol{y}-\boldsymbol{x}^k)\right]dy \tag{4.5}$$

$$= \sqrt{\frac{1}{N}}\sum_{k=1}^{N}\left[\int_{\boldsymbol{y}\in\mathbb{R}^3} F_\lambda(\boldsymbol{y}-\boldsymbol{x}^k)\boldsymbol{K}(\boldsymbol{x},\boldsymbol{y})dy\right]\times\boldsymbol{c}^k\ . \tag{4.6}$$

when substituting the vorticity disruption $\tilde{\boldsymbol{\omega}}$ by its expression given in Equation (4.1). After grouping most of the integral part of the above expression into a single unknown quantity, Poletto rearranges this formulation to depend on a radial vector $\boldsymbol{r}^k = \frac{\boldsymbol{x}-\boldsymbol{x}^k}{\lambda}$ normalized by the structure size λ and $d^k = |r^k|$ the corresponding distance. After these rearrangements, the velocity disruption $\tilde{\boldsymbol{u}}$ of Equation (4.6) can be rewritten under the form :

$$\tilde{\boldsymbol{u}}(\boldsymbol{x}) = \sqrt{\frac{1}{N}}\sum_{k=1}^{N}\frac{Q_\lambda(\boldsymbol{r}^k)}{(d^k)^3}\boldsymbol{r}^k\times\boldsymbol{c}^k\ , \tag{4.7}$$

with Q_λ now the new unknown shape function. For each dimension $i=1,2,3$, the component $\tilde{u}_i$ of the velocity disruption is finally expressed as :

$$\tilde{u}_i(\boldsymbol{x}) = \sqrt{\frac{1}{N}}\sum_{k=1}^{N}\frac{q_\lambda(d^k)}{(d^k)^3}(\boldsymbol{r}^k\times\boldsymbol{c}^k)_i\ , \tag{4.8}$$

where $(\boldsymbol{r}^k\times\boldsymbol{c}^k)_i$ denotes the i-th component of the results of this cross product (or $\epsilon_{ijl}r_j^k c_l^k$ using the Levi-Civita notation), and q_λ is now the final purely scalar form of the shape function to be determined.

4.2.2 Shape function q_λ

Basic conditions

Within this context, the as yet undefined shape function q_λ must verify the following conditions :

1. First of all, turbulent velocity field $\tilde{\boldsymbol{u}}$ resulting from the three components described by Equation (4.8) must verify the incompressibility condition. The differentiation of these components shows that by using the same shape function q_λ for the three directions $i=1,2,3$ (or x, y and z) and depending only on the radial distances d^k, the resulting velocity field $\tilde{\boldsymbol{u}}$ is assured to be divergence free as long as it is continuous and differentiable.
2. Following this previous point, the shape function q_λ is required to make up for the singularity around 0 inherent to the expression of Equation (4.8) :

$$\lim_{\boldsymbol{x}\to\boldsymbol{x}^k}\frac{q_\lambda(d^k)}{(d^k)^3}\sim C(d^k)^n,\quad \text{with } C\neq 0 \text{ and } n\geq 0\ , \tag{4.9}$$

in order to prevent a singular behaviour around the center of each turbulent structure.

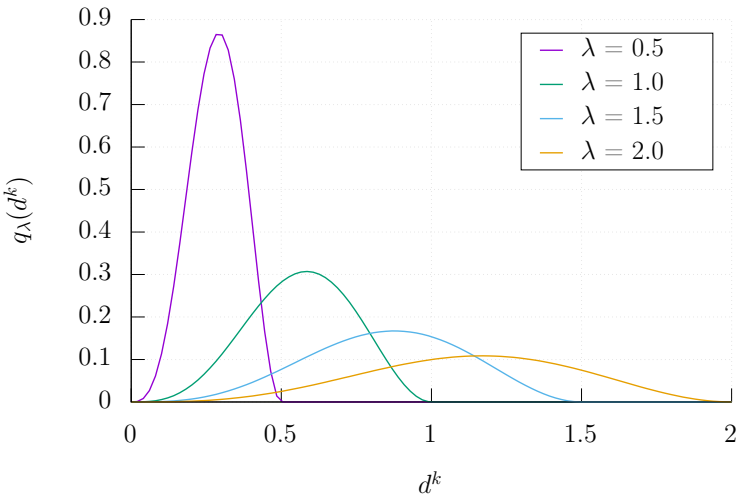

Figure 4.2: *Shape function q_λ as defined in Equation* (4.12)*, for a sample volume size $\tilde{V} = 1$ and varying turbulent structure sizes λ.*

3. Lastly, for the sake of ease and computational efficiency, the influence of each turbulent structure should be strictly limited to the radius given by its size λ, *i.e.* :

$$q_\lambda(d^k) = 0 \text{ for } |d^k| > 1 \ . \tag{4.10}$$

Reproduction of an isotropic Stress Tensor

Next, Poletto begins by searching for a shape function able to ensure that the entire perturbation velocity $\tilde{\boldsymbol{u}}$ is able to produce a diagonal and isotropic Reynolds Stress Tensor $\overline{\overline{\boldsymbol{R}}}$. This corresponds to the condition that if the average value of the turbulent structure intensities c^k is 1, the average value of the normal stress components $\tilde{u}_i\tilde{u}_i$ must be 1 as well. In verifying this proposition, Poletto obtains an additional condition on the function q_λ. He is then finally able to suggest one simple possible form for a suitable shape function :

$$q_\lambda(d^k) = B\left(\sin(\pi d^k)\right)^2 d^k \ , \tag{4.11}$$

with B a normalizing constant. While he states that the value of B must be $\sqrt{\frac{16\tilde{V}}{15\pi\lambda^3}}$, our tests of the reproduction of the Reynolds Tensor as well as a re-examination of his reasoning have shown that it is in fact only $\sqrt{\frac{\tilde{V}}{\pi\lambda^3}}$ (where $\tilde{V}$ indicates once more the volume of the chosen turbulent study space). The justification for this rectification is exposed in Appendix A, using the notations of Poletto's thesis. We obtain at last a possible shape function verifying all the required conditions :

$$q_\lambda(d^k) = \begin{cases} \sqrt{\dfrac{\tilde{V}}{\pi\lambda^3}}\left(\sin(\pi d^k)\right)^2 d^k \text{ for } |d^k| < 1, \\ 0 \text{ elsewhere.} \end{cases} \tag{4.12}$$

The shape of this antisymmetric function is shown in Figure 4.2.

Calibrating of structure intensities c^k

The shape function q_λ has now been formulated so as to ensure that the resulting velocity field $\tilde{\boldsymbol{u}}$ will result in a normalized isotropic Reynolds Stress Tensor $\overline{\overline{\boldsymbol{R}}}$. Anisotropy can then be introduced to this tensor using the last remaining unknown element of the turbulent structure intensities $\boldsymbol{c}^k$. The value of these intensities must be carefully chosen so that a specific desired Stress Tensor can be reproduced. The final solution obtained by Poletto establishes a relation between the eigenvalues ξ_i of the Reynolds Stress Tensor $\overline{\overline{\boldsymbol{R}}}$ and the average values which must be chosen for the components c_i^k of the intensity vectors $\boldsymbol{c}^k$, for $i = 1, 2, 3$:

$$(c_i^k)^2 = \left(\sum_{j=1}^{3} \xi_j\right) - 2\xi_i \ , \tag{4.13}$$

i.e.

$$c_i^k = \pm\sqrt{\left(\sum_{j=1}^{3} \xi_j\right) - 2\xi_i} \ . \tag{4.14}$$

For the case of a diagonal stress tensor matrix, its eigenvalues ξ_i are simply the normal stress values making up its diagonal components. However this formulation can also be used for the case of a non diagonal tensor matrix, as will be covered in the next paragraph.

It must be noted additionally that this last result imposes a mathematical restriction on the Reynolds Stress Tensors which can be used with this method, for the value under the square root to remain positive.

Non-diagonal Stress Tensor

With this addition, it has now been established that any suitably chosen diagonal Reynolds Stress Tensor can be accurately reproduced. In order to move on to the possibility of reproducing any stress tensor (provided that its eigenvalues remain suitable to the square root of Equation (4.14)), Poletto uses the trick of a change of referential.

Namely as a 3x3 symmetric matrix, it is always mathematically possible to find a reference system in which the Reynolds Stress Tensor $\overline{\overline{\boldsymbol{R}}}$ is diagonal. The average structure intensities $\boldsymbol{c}^k$ can be computed using its eigenvalues, as established in the previous Paragraph. It is then only a matter of applying the transformation from this local diagonal referential to the global referential, in order to ensure that the same shift will be translated to the resulting Reynolds Stress Tensor. This will have the effect of skewing the turbulent structures to the desired directions, with no other repercussions on the conditions on the velocity field.

In this case, the components $\tilde{u}_i$ of the turbulent velocity field can be readjusted from the formulation of Equation (4.8) to :

$$\tilde{u_i}(\boldsymbol{x}) = \sqrt{\frac{1}{N}} \sum_{k=1}^{N} \frac{q_\lambda(d^k)}{(d^k)^3} (\boldsymbol{r}^k \times \mathcal{R}(\boldsymbol{c}^k))_i \ , \tag{4.15}$$

with $\mathcal{R}$ the rotation corresponding to the transformation from the referential in which the Reynolds Tensor $\overline{\overline{\boldsymbol{R}}}$ is diagonal back into the global referential.

This end result gives the final elements for the implementation of the DFSEM. We have come to a formulation which could be considered as quasi-vortical for the fluctuating velocity $\tilde{\boldsymbol{u}}$, which is much closer to the Biot-Savart formulation serving as a basis for the Vortex Method compared to the sources and sinks and of the SEM.

4.3 Analysis of the generated velocity fields

While this formulation appears slightly more complex to the initial SEM, we have been able to implement it into our numerical software and obtain promising results. We are then able to perform the same analysis and validations as already presented in the previous Chapter when using the SEM turbulence generation.

4.3.1 Reproduction of the Reynolds Stress Tensor

A convergence analysis of the computed Turbulent Kinetic Energy (TKE) is performed depending on several numerical parameters, such as the size of the turbulent structures as well as the number of turbulent structures per volume unit, characterised by the filling ratio R_f. Due to the restrictions on the anisotropic ratio mentioned previously, a basic isotropic ratio is used for the computations using the DFSEM : $(1, 1, 1)$.

Based on the time series of the velocity computed at a single point for 6 hours of simulated time, the evolution of the current Turbulent Kinetic Energy (TKE) is validated, as well as its convergence towards the target value given by the user-prescribed Reynolds stress tensor. The time series shown in Figure 4.3 show the disparity of the quality and speed of this convergence depending on the choice of the parameters R_f and λ. While all sets of parameters show an eventual satisfying convergence towards the direction of the target value, this convergence appears to be faster when using the DFSEM compared to the SEM (as can be recalled from the corresponding Figure 3.8 of the previous Chapter), and for both methods the convergence is slower as well when using a small number of large sized turbulent structures compared to a high number of smaller structures.

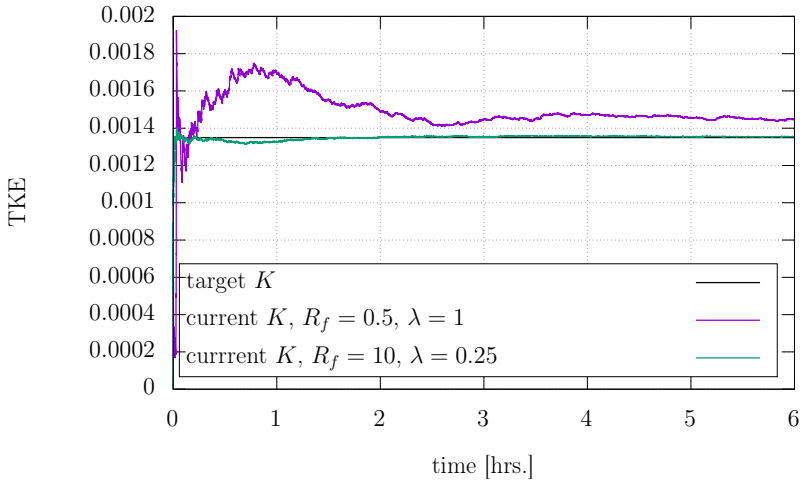

Figure *4.3: Example of the time series of the Turbulent Kinetic Energy in the "best" and "worst" convergence scenarios.*

In order to confirm the tendencies noted on the time series of the TKE, and given the random aspect of each individual simulation using both the SEM and DFSEM, 50 time series such as those presented in Figure 4.4 are performed for each set of parameters λ ranging from 0.25 to 1 as well as R_f ranging from 0.1 to 10. The maximal (dotted lines) and average (full lines) of the errors committed on the 50 final values of the TKE for each

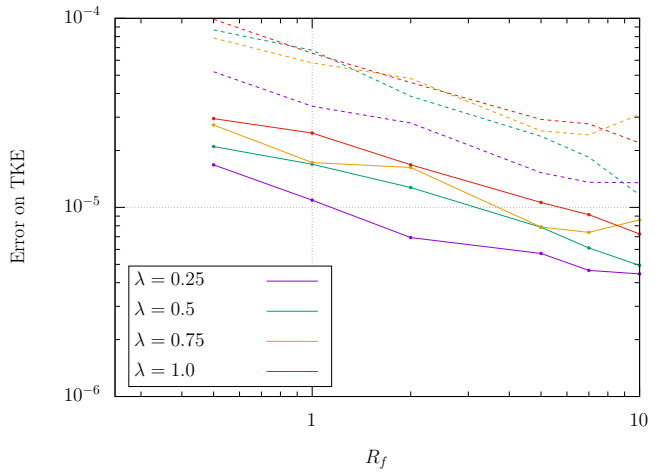

Figure *4.4: Maximal (dotted lines) and average (full lines) errors committed on the Turbulent Kinetic Energy depending on the size of the turbulent structures used (averaged using 50 sample times series of 6 hours each for each set of parameters).*

set of parameters are presented in Figure 4.4. The clear trends mentioned previously can thus be confirmed : as was the case for the SEM, the higher the filling ratio Rf and the smaller the length scale λ, the lower the error on the final TKE.

4.3.2 Physical properties of the generated flow

Power Spectral Density

The reconstructed velocity fields can now be further analysed by looking once again at the Power Spectral Density (PSD) spectra of Figure 4.5. Similarly to the procedure used during experimental trials, time series of the numerically produced velocities are recorded now for a duration of one hour of simulated time, and post-processed in order obtain the PSD spectra. As already observed for Jarrin's initial SEM formulation, the choice of a single value for the structure sizes λ leads to a poor reproduction of the desired Power Spectral Density. The same behaviour is now evidenced for the DFSEM version of Poletto. However the quality of these PSDs can be largely improved by the introduction of a statistical variation $\sigma(\lambda)$ on the size λ of the turbulent structures. The size of all turbulent structures are no longer all identical throughout the study space and simulation, but calculated using a normal distribution law centred around an average value still noted λ of standard deviation $\sigma(\lambda)$. In the present example, introducing a standard deviation $\sigma(\lambda) = 100\%$ around the average value $\lambda = 0.5$ signifies that the size of a turbulent structure k can now range from $\lambda^k = 0$ to $\lambda^k = 1$. Even though the PSD spectra are much improved with the introduction of heterogeneous structure sizes, the curves do not perfectly fit the experimentally measured values from Gaurier *et al.* [80] represented in black in Figure 4.5. This is most likely due to the fact that the turbulent structures sizes are evenly spread around the central value, which does not represent the physical phenomenon. A similar but asymmetrical normal distribution will soon be investigated in order to obtain more of the smaller sizes, which is expected to mathematically better reproduce the physical turbulent cascade. Additional improvements are expected with the use of this new spreading function.

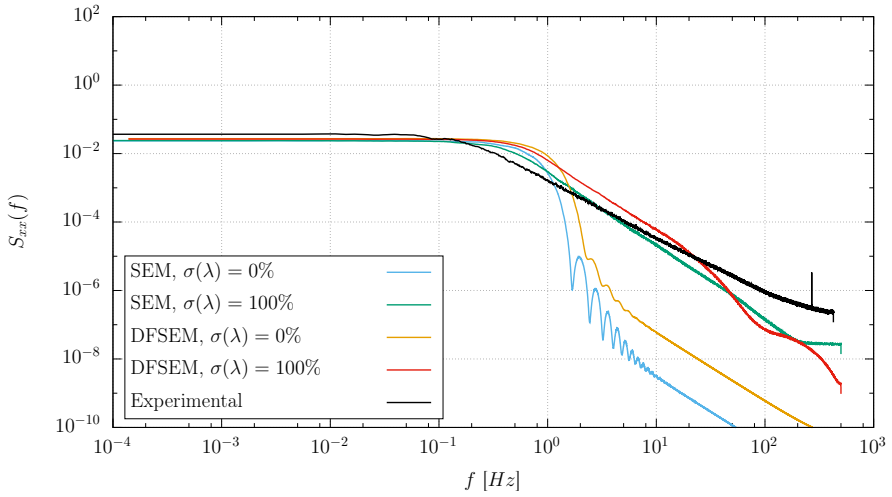

Figure 4.5: *Power Spectral Density (PSD) spectra,* $I_\infty = 15\%$, $U_\infty = 0.8\ m/s$, $\lambda = 0.5$.

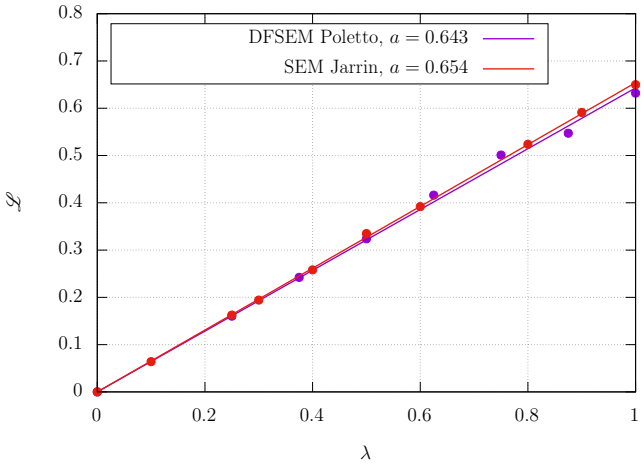

Figure 4.6: *Taylor macro-scale versus length scale* λ, $I_\infty = 15\%$, $U_\infty = 1.0\ m/s$, $\sigma(\lambda) = 0\%$, $R_f = 1$.

Turbulent length scale

A last physical turbulent characteristic is now analysed in the form of the Taylor macro-scale $\mathscr{L}$. The same numerical velocity time series as those used to compute the PSD curves are post-processed in order to evaluate this length scale of the turbulent behaviour in the generated flow. The auto-correlation function is evaluated and using the first zero-crossing together with Taylor's frozen hypothesis, the Taylor macro-scale $\mathscr{L}$ is finally obtained. For both the regular SEM and the recently developed DFSEM, near identical linear behaviours are obtained as shown in Figure 4.6 : $\mathscr{L} \approx 0.65\lambda$ for both Jarrin and Poletto's formulations. A similar analysis with different values of $\sigma(\lambda) \neq 0$ will also be necessary to have a full understanding of all the parameters used in both formulations.

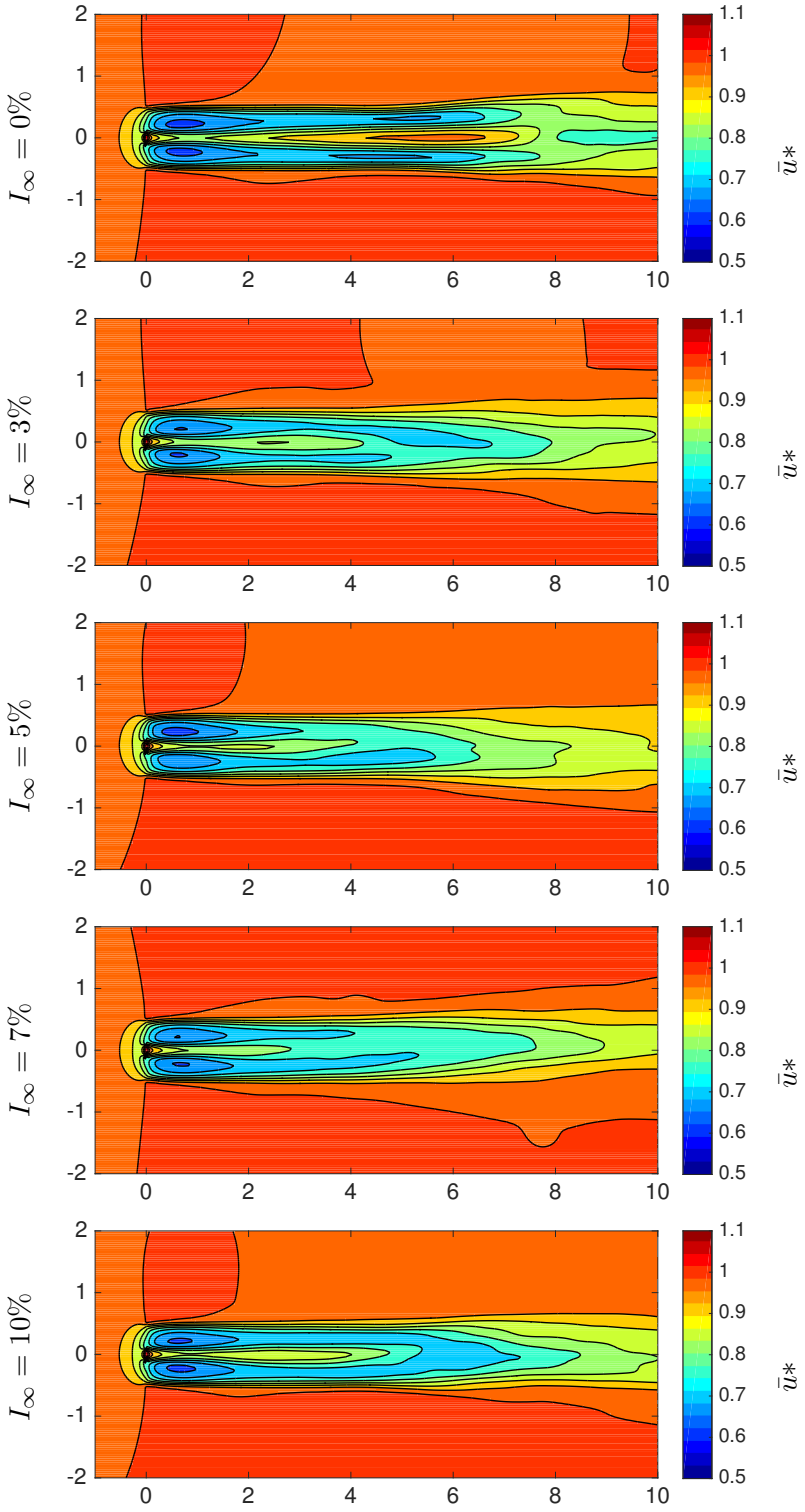

Figure 4.7: *Time-average of one turbine wake with various ambient turbulence intensities (with no hub and no mast) : Poletto's DFSEM turbulence filtered,* $TSR = 2.5$, $U_\infty = 1.0$, $R_f = 1$, $\lambda = 0.5$, $\sigma(\lambda) = 0\%$, $(\sigma_u : \sigma_v : \sigma_w) = (1.0 : 1.0 : 1.0)$.

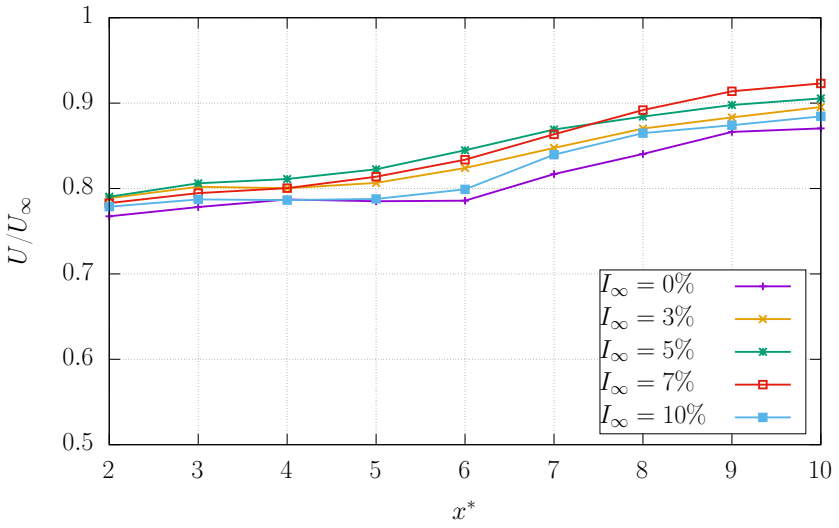

Figure 4.8: *Velocity ratio u/u_∞ integrated in the wakes of the turbine blades shown in Figure4.7, using varying levels of turbulence intensity I_∞ generated with Poletto's DFSEM.*

4.4 Computation of a turbine wake

Finally, computations of turbine wakes with varying ambient turbulence intensities ranging from $I_\infty = 0\%$ to $I_\infty = 10\%$ are presented in Figure 4.7. An isotropic turbulence is used once again for Poletto's DFSEM method, with a turbulent structure size of $\lambda = R/2$ and no variation ($\sigma(\lambda) = 0\%$). Additionally, as the fluctuating turbulence has by definition a zero average ($\langle u'_\infty \rangle = 0$), this component is once again removed during the post-processing of the time-averaged velocity maps, to emulate the effect of a much longer time average than the last 50 seconds of 90 second simulations used here. Only the blades are considered in these simulations, the nacelle and hub of the turbine being omitted at this stage. As a matter of reference, these computations are run in approximately 15 hours on 252 cores of the regional calculator CRIANN.

As the rotor hub and nacelle are not taken into account, a localised velocity increase can be observed downstream from the center of the turbine. However as further evidenced by the integrated velocity ratio curves of Figure 4.8, the DFSEM ambient turbulence level I_∞ does not appear to have the desired effect of shortening of the turbine wake, as was present in the SEM simulations (see the corresponding results of Figure3.19). The ordering of velocity ratios confirms that the longest wake is obtained without ambient turbulence, as evidenced by the yellow curve remaining the lowest. After this the curves representing increasing levels of ambient turbulence do not show any logical progression, with the blue curve representing the highest turbulence intensity being the second lowest for instance, and the others following close by in no discernible order.

Although the convergence of the TKE confirmed that we are able to accurately replicate the ambient turbulence intensity in the incoming flow, we do not yet appear to be able to obtain its expected influence on the turbine wakes. This remains to be investigated, and could be explained either by an as yet undetected implementation error or by the choice of parameters which have not been explored in great detail so far for this formulation. Still, from this preliminary investigation, this possibility of taking into account divergence free upstream ambient turbulence in the Lagrangian Vortex Blob formalism is already an interesting feature.

4.5 Preliminary conclusion on Poletto's formulation

We have pursued the study of computations of turbine wakes under the Lagrangian Vortex blob formalism with an added account for ambient turbulence. A major drawback of the initially considered version of Jarrin's Synthetic Eddy Method is that it is based on velocity sources and sinks that prevent the ensuing velocity fields from being divergence free. This feature is quite important as the Lagrangian Vortex blob formalism relies on a divergence free velocity field for the Biot-Savart equation. In practice, this initial formulation of Jarrin *et al.* did not show any major incompatibility when implemented in the code, at least for reasonable values of turbulence intensity.

In order to be fully consistent with the Lagrangian Vortex blob hypothesis, a more recent formulation of the Divergence Free Synthetic Eddy Method was implemented in the code. Both formulations appear to behave similarly in terms of reconstructed Power Spectral Densities and Taylor macro-scales from velocity records, although the more recent version of Poletto's DFSEM shows an improvement in terms of temporal convergence. Finally, numerical computations of turbine wakes with different levels of ambient turbulence are presented, which tend to indicate that Poletto's formulation of DFSEM seems to be less diffusive than Jarrin's regular SEM formulation, although it does not yet show the expected progression with increasing turbulence intensity levels. Even if more studies with several parameters variations are still needed to have a better understanding of this model, Poletto's DFSEM already shows some very interesting features for modelling ambient turbulence in a Lagrangian Vortex framework.

Chapter 5

Simulation of tidal turbines in a turbulent flow

5.1 Introduction

This Chapter is largely excerpt from a prospective paper aiming to highlight the simulations of wake-turbine interactions in realistic operation conditions, and how they can be performed using the VPM code combined with the turbulence generation methods described in the two previous Chapters.

The geometrical configuration considered here is the pre-commercial farm NEPTHYD that was granted to a subsidiary company of Engie by the French Ministry of Energy and Environment, via its agency ADEME, in December 2014 (see Figure 5.1). At this time, Engie had contracted with Alstom the manufacturing of four Oceade™, a three bladed turbine of 18 m diameter rated at 1.4 MW. Following the purchase of Alstom's energy activities by General Electric, the tidal activities of Alstom were rapidly stopped and this demonstration project did not become a reality. However, in the meantime, Engie had started the consenting process to the French authorities and some official documents were issued and made public. Therefore, the farm configuration (number of turbines, turbine positioning, etc.), velocity value, rotational speed, etc. were taken from the report issued by the Autorité Environnementale on the 6th of April 2016 [105]. Only the ambient turbulence values were reproduced from the paper of Sentchev *et al.* [29]. However, the interesting aspect of this configuration is that it is a real industrial pre-commercial farm configuration, very relevant for the scientific community as well as new industrial projects launched for instance by Hydroquest and Sabella.

Section 5.2 is dedicated to the validation of the SEM implementation, together with the influence of several of its physical and numerical parameters. Section 5.3 presents the computations performed on the NEPTHYD configuration with different ambient turbulence levels and length scales. It will also highlight wake-turbine interactions in the case of asymmetry in the flow, occuring when the tidal flow is not fully bi-directional as is most often the case.

5.2 Computation of a single tidal turbine

5.2.1 Numerical set-up and tested configurations

The tidal turbine modelled in this study has a diameter D of 18 m. The blades of Alstom's Oceade™ turbine are patented so we chose an open configuration, which cor-

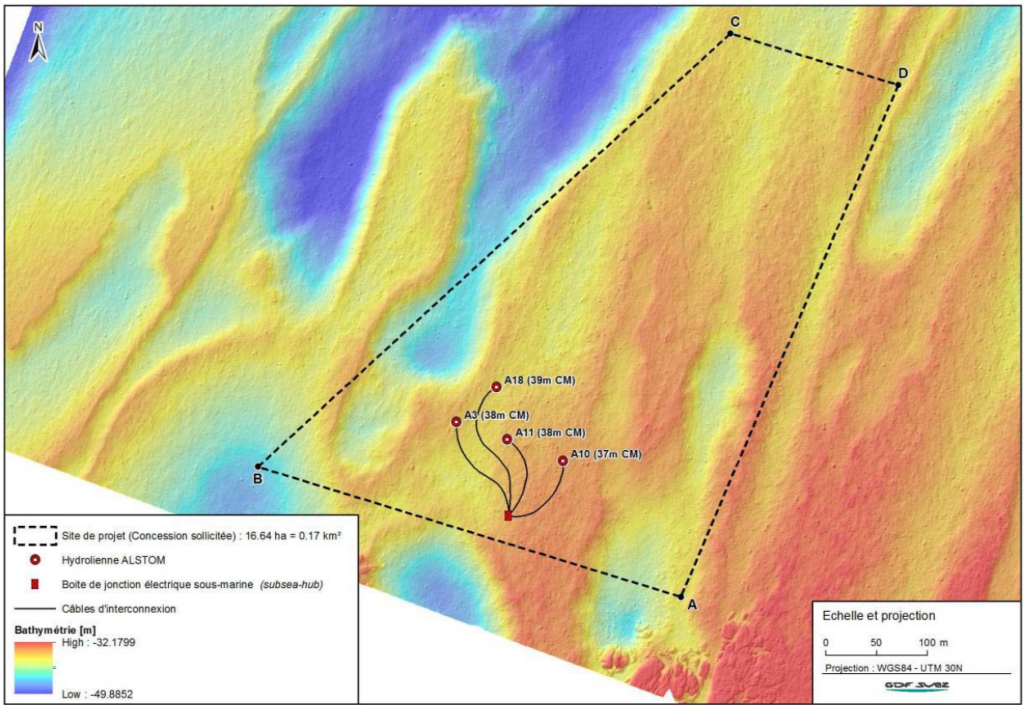

Figure 5.1: *Configuration of the NEPTHYD project : a four turbine pre-commercial farm developped by Engie in 2014 and meant to be equipped with Alstom's Oceade*^{TM} *turbine. The image is reproduced from the report [105] of the Autorité Environnementale, an agency of the French Ministry of Energy and Environment.*

responds to IFREMER's generic turbine. Experimental results obtained for the latter by Mycek *et al.* [78] will be used for comparison. More details about the numerical model and IFREMER's turbine can be found in [18]. As a reminder, within these simulations the mesh is still only made up of a zero-thickness surface mesh for the blades and possibly the turbine nacelle if used. The fluid is represented by Lagrangian vortex particles freely evolving throughout the computational domain following the Navier-Stokes equations. When using the SEM for the addition of ambient turbulence, a study space must be defined where the turbulent structures will be placed, as explained in Chapter 3. Here, the dimensions of this space are $L_x = 243\,\text{m} = 13.5\,D$ along the main flow direction, and $L_y = L_z = 108\,\text{m} = 6\,D$ along the horizontal and vertical directions. The blade surface meshes are defined as those presented in previous studies [18, 45, 88]. In the present work, 11 mesh elements are discretising the blade along the blade radius and 5 along the blade chord. A turbine is represented by 210 surface elements without the nacelle and 964 with the nacelle. The inter-particle spacing is set to $dh = 0.6$ m, similar to the surface mesh discretisation along the blade radius, with a smoothing parameter of $\epsilon = 1.5\,dh$. In all the following computations, the upstream incoming velocity is set to $U_\infty = 3.2$ m/s. The Tip Speed Ratio (defined as $\text{TSR} = \omega R/U_\infty$, where ω and R are the rotational speed and the turbine radius respectively) is set to 3.67 in Paragraphs 5.2.2 and 5.2.3 for comparison with the experimental results. In Section 5.2.4, the TSR is set to 4.1 in order to have the same rotational speed as the one used for the NEPTHYD configuration of Section 5.3. A time step of $dt = 0.044$ s is imposed owing to the CFL-like condition for vortex methods and the simulation time is set to 200 seconds. Finally, an isotropic turbulence is used and different turbulence intensities I_∞, structure sizes λ, standard deviations $\sigma(\lambda)$ and filling ratios R_f are considered. All the results presented here are time-averaged. As the

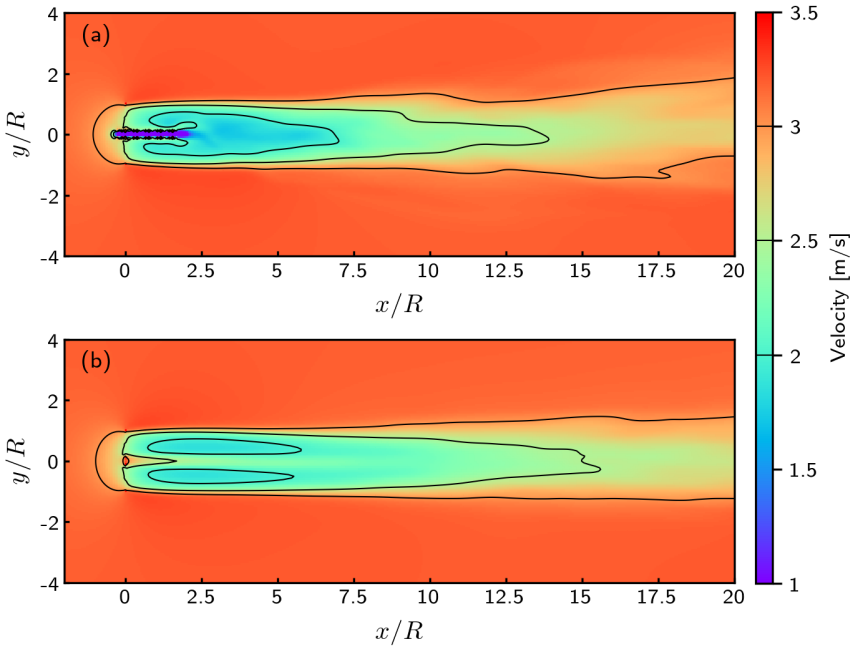

Figure 5.2: *Time-averaged wakes obtained for I_∞=1.5%, TSR=3.67, $\lambda = 4.5$ m, $\sigma(\lambda) =$ 0% and R_f=1. (a) with nacelle. (b) without nacelle.*

fluctuating turbulence has by definition a zero average ($\overline{\overline{\boldsymbol{u}}} = 0$), this component is once again removed during the post-processing of the time-averaged velocity maps, to emulate the effect of a much longer time average than the last 68 s (90 s to 103 s for Paragraph 5.2.4) of 200 s simulations used here.

5.2.2 Omission of the turbine nacelle

In the previous Chapter, it was noted that the use of the turbine nacelle (referred to previously as the cylindrical hub) could possibly generate some numerical instabilities. Even though these instabilities were not entirely resolved, the question of the inclusion of the turbine nacelle can still be posed. Looking at the numerically computed wake velocity fields presented in Figure 5.2 would make the answer tend towards the necessity of its inclusion. The near wake is really different and a much larger velocity deficit is experienced when using the nacelle. However, the global wake length is near-identical, even for this low ambient turbulence value of $I_\infty = 1.5\%$. Looking at the corresponding velocity profiles presented in Figure 5.3 comforts this analysis. The first two velocity profiles at $x/D = 1.2$ and $x/D = 2$ are very different depending on wether the nacelle is included or not. The presence of the nacelle markedly improves the result in comparison with the single turbine wake measurement done at laboratory scale with a similar ambient turbulence intensity and reproduced from [78]. However, for the four remaining velocity profiles depicted in Figure 5.3, the differences with and without the nacelle are not very significant. It could be argued that taking into account the nacelle would be an additional numerical complexity without a low benefit to the end quality of result, especially in the far wake. On top of that, the differences are here highlighted by the fact that the turbulence intensity I_∞ is very low, and the reported values are much higher in the Alderney Race as it will be presented in Section 5.3.

If we now compare the disc integrated velocity profiles normalised by the disc integrated

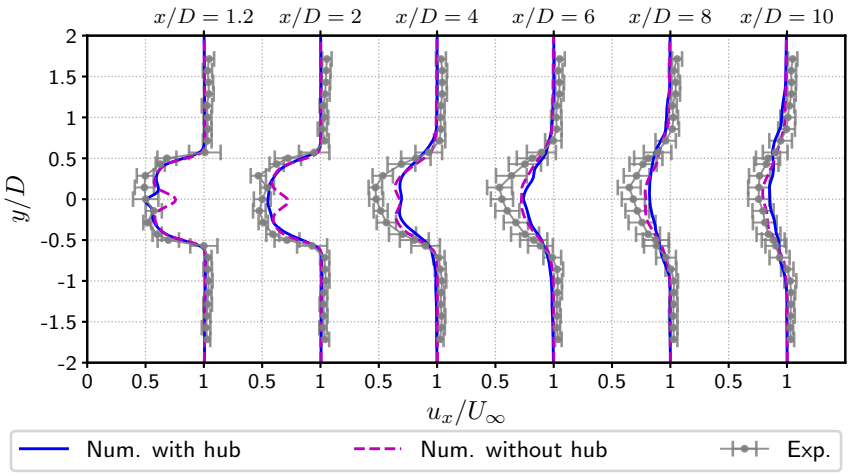

Figure 5.3: *Comparison of the experimental velocity profiles with the numerical results obtained with and without nacelle, for I_∞=1.5%, TSR=3.67, $\lambda = 4.5$ m, $\sigma(\lambda) = 0\%$ and R_f=1.*

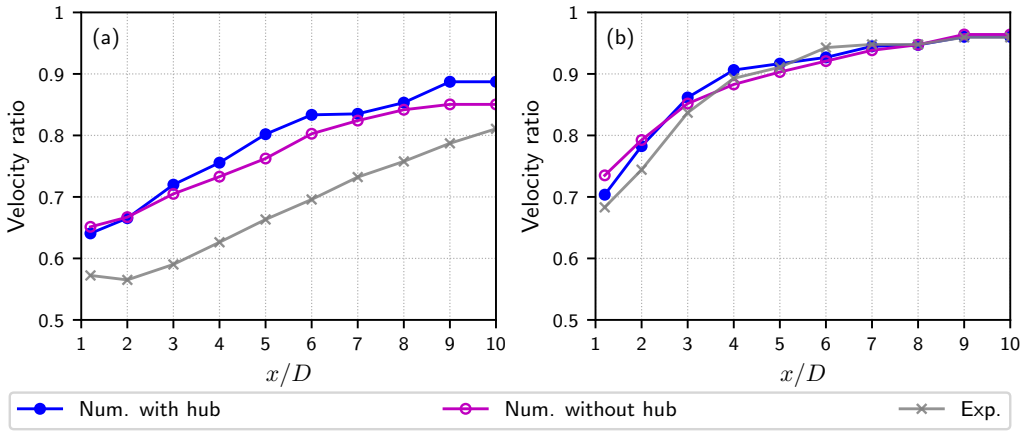

Figure 5.4: *Comparison of the experimental and numerical disc-averaged velocities (TSR=3.67, $\lambda = 4.5$ m, $\sigma(\lambda) = 0\%$ and R_f=1). (a) I_∞=1.5%. (b) I_∞=15%.*

value of U_∞ (see Figure 5.4), the procedure of wake integration being clearly presented in [78] for the experimental results, the differences are hardly visible. Moreover, both numerical curves with $I_\infty = 1.5\%$ are underestimating the experimental integrated velocity (see Fig. 5.4(a)), which is a problem already identified and possibly due to a too high numerical dissipation, especially visible at low ambient turbulence. However, for the higher ambient turbulence value of $I_\infty = 15\%$, the comparison of both numerical results and the experimental one depicted in Figure 5.4(b) are really encouraging us towards the simplest solution. Therefore, for the remainder of this Chapter, the turbine nacelle will not be taken into consideration as a matter of numerical simplification and speed-up.

5.2.3 Influence of the filling ratio R_f

This Paragraph focuses on the evaluation of the influence of the filling ratio R_f as presented in Chapter 3. Due to the nature of the SEM method as a stochastic representation of the ambient turbulent velocity field, a large number of turbulent structures and hence a high value of R_f is necessary to statistically represent the turbulent velocity field.

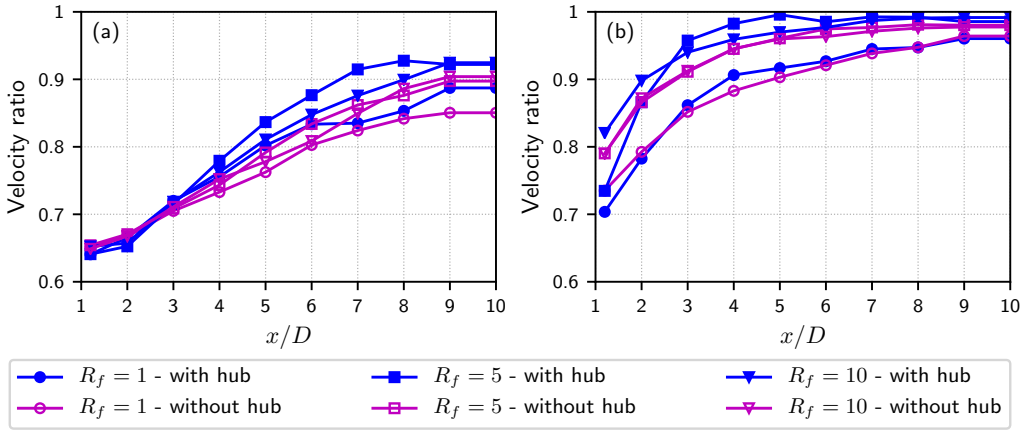

Figure 5.5: *Comparison of the numerical disc-averaged velocities obtained for three filling ratios R_f and two turbulence intensities (TSR=3.67, $\lambda = 4.5$ m, $\sigma = 0\%$). (a) I_∞=1.5%. (b) I_∞=15%.*

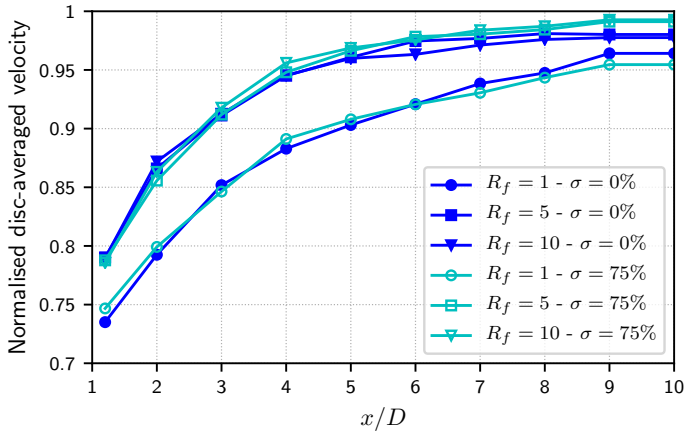

Figure 5.6: *Comparison of the numerical disc-averaged velocities obtained for three filling ratios R_f and two standard deviations $\sigma(\lambda)$ (TSR=3.67, $\lambda = 4.5$ m, I_∞=15%).*

The numerical assessment on this statistical convergence of the numerically obtained I_∞ presented in [88, 106] concluded that a R_f value higher than one is sufficient to have a statistical convergence, bearing in mind that the total number of structures should not be too low to have enough statistical representation. However, as the turbulent structure size λ is increasing to better represent the *in-situ* turbulence integral length scale $\mathscr{L}$, a higher value than one may be necessary to have enough structures to ensure the above mentioned statistical representation. In that respect, Figure 5.5 shows the disc-averaged velocity deficit for turbulence intensities of I_∞=1.5% in Fig. 5.5(a) and I_∞=15% in Figure 5.5(b). For the lower I_∞ value, the numerical disc-averaged velocity deficit was already too dissipative as indicated in Paragraph 5.2.2 (Figure 5.4(a)). A higher value of R_f is slightly intensifying the phenomenon of numerical dissipation, and even more for the far wake from $x/D \geq 5D$ in Figure 5.5(a). For I_∞=15%, the results with $R_f = 1$ are in accordance with the experimental results, as highlighted in Figure 5.4(b). However, an overestimation of the disc-averaged velocity is also visible for $R_f \geq 5$ as depicted in Figure 5.5(b). As the ambient turbulence value is higher and the turbulence structures are more numerous with $R_f > 1$, such a phenomenon is understandable and physically interpretable.

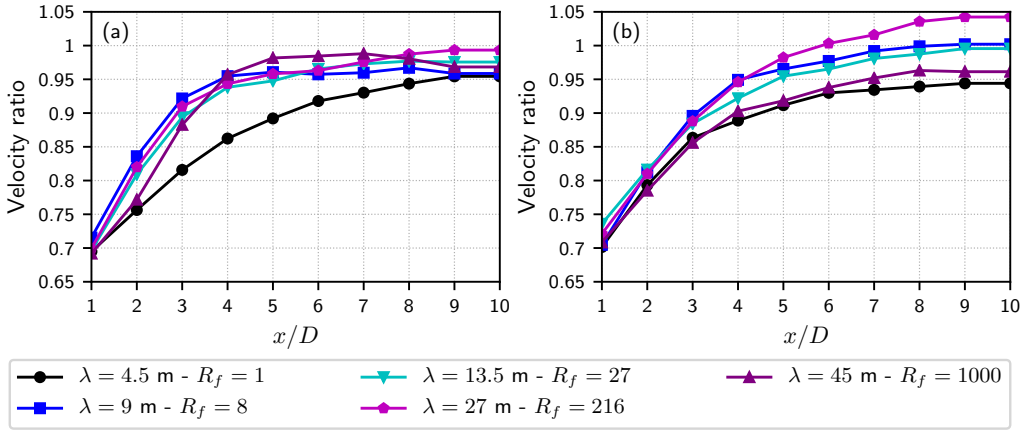

Figure 5.7: *Comparison of the numerical disc-averaged velocities obtained for TSR=4.1, I_∞=10% and several λ. (a) $\sigma(\lambda) = 0\%$. (b) $\sigma(\lambda) = 75\%$.*

The influence of the turbulent structure size variation, represented by the value of $\sigma(\lambda)$, does not change the tendency as one can observe from the data presented in Figure 5.6 for I_∞=15%. Choma Bex *et al.* [88, 106] reported that a higher value of $\sigma(\lambda)$ would improve the spectral representation of the turbulent kinetic energy cascade, a $-5/3$ slope being nearly obtained from $\sigma(\lambda) = 75\%$ and above. However, as shown in Figure 5.6, $\sigma(\lambda) = 75\%$ still really overestimates the dissipation of the experimental disc-averaged velocity deficit for the higher values of R_f. As a conclusion on that aspect, the value of $\sigma(\lambda)$ does not have an influence on the velocity deficit and the driving parameter is the filling ratio R_f, the experimental disc-averaged velocity deficit being accurately reproduced both for $\sigma(\lambda) = 75\%$ or $\sigma(\lambda) = 0\%$ with $R_f = 1$ and always over-dissipated with higher values of R_f.

5.2.4 Influence of the turbulent structure size λ

Lastly, the influence of the turbulent structure size λ, and hence the integral length scale $\mathscr{L}$, is presented in Figure 5.7. To better represent the physical turbulence characteristics of the Alderney Race as reported in the literature [29,31,33,34] for instance, higher values of λ were evaluated of physically represent the $\mathscr{L}$ values of a couple of decametres as measured in tidal sites. With $\lambda = 4.5$ m, $R_f = 1$ corresponds to $N = 7426$ turbulent structures. In order to have a sufficient statistical representation of the flow with higher values of $\mathscr{L}$ or λ, we chose to keep the same number of structures, which increases the value of the filling ratio R_f.Once again, an over-dissipation phenomenon is obtained for both $\sigma(\lambda) = 0\%$ and $\sigma(\lambda) = 75\%$ as shown in Figure 5.7. The case with $\sigma(\lambda) = 75\%$ is even noisier but tremendous turbulent structure sizes of up to 2λ can be regularly obtained in the flow field with $\sigma(\lambda) = 75\%$. This might not be so physical as the integral length scale is closer to the larger size encountered in the *in-situ* flow. Therefore, a new asymmetric law for the distribution of λ is under works to better represent the physical characteristics that are : a lower number of large structures and much more smaller structures possibly reproducing the real turbulent cascade structure distribution in homogeneous turbulence. This will be tested soon but, for the time being, the present implementation is still worth investigating on a real 4 tidal turbine farm configuration.

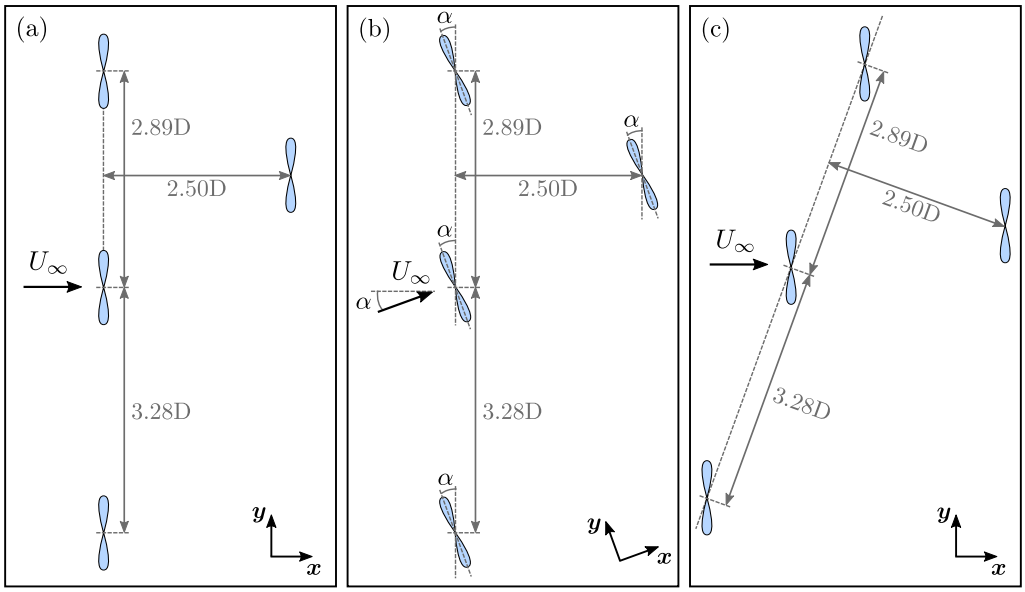

Figure 5.8: *Four tidal turbine array configurations : (a) initial configuration (straight flow), (b) configuration with a yawed flow, (c) configuration with a yawed flow used for the simulation.*

5.3 Four tidal turbine array : the NeptHyd layout

5.3.1 Description of the selected configuration : the NEPTHYD project.

As mentioned in the introduction, the NEPTHYD pre-commercial farm was meant to be made up of four of Alstom's Oceade™3-bladed 18 m diameter turbines, with geometrical characteristics and blade profiles inspired by those of the former TGL turbine. This same TGL geometry also served as a basis for the open-geometry turbine of IFREMER since the first work of Maganga *et al.* [107]. This open-geometry model (defined in [18]) is used in this work, as indicated in the previous Section. According to the report of the Autorité Environnementale [105], the optimal production current velocity for the Oceade™ turbine is higher than 3.1 m/s, which is why we chose an upstream velocity U_∞ of 3.2 m/s. The TSR was set as 4.1, which corresponds to the optimal rotational speed of the device (see Table 1 of [105]). Following the projected configuration shown in Figure 5.1, the four turbines are positioned at approximately the same depth of 38 ± 1 m. In order to simplify this configuration, and as the bathymetry cannot be taken into account in the present approach, all turbines are set to the same vertical position.

The schematic representations of Figure 5.8 show the turbine layout and spacing within the computed domain. As shown in Figure 5.1, the first front row of three turbines is perpendicular to a direction inclined at an angle of 20° from the north. This specific direction corresponds to the main flood and ebb direction at this position of the Alderney Race. Therefore, the incoming velocity vector is exactly perpendicular to the three upstream turbines as presented in Figure 5.8(a). Keeping in mind that tidal flows are not always bi-directional, for instance Maslov *et al.* [108] reported approximately 15° and 35° in two sites of Brittany, an inclination of this velocity vector is indicated in Figure 5.8(b) with an angle α. In the Alderney Race, tidal angular asymmetry can vary to a great degree. However, as the turbines are equipped with a yaw mechanism, they can rotate to align with the new flow direction. Therefore, and in the present configuration of Figure 5.8(b), inter-

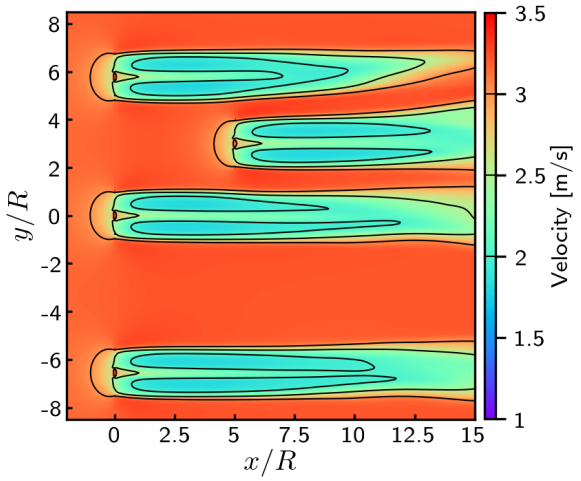

Figure 5.9: *Time-averaged wakes obtained without ambient turbulence for TSR=4.1.*

action will be highly enhanced between the middle upstream turbine and the downstream one. The higher the angle of the tidal asymmetry, the more intense the interaction will be. Such configurations will be tested with several tidal angular asymmetry angles, namely 5°, 10°, 15° and 20°. These results will be presented in Paragraph 5.3.3. To facilitate the flow representation for the simulations in Paragraph 5.3.3, the configuration of Figure 5.8(b) will be rotated by the angle α so that the incoming velocity vector always aligns with the x-axis, as depicted in Figure 5.8(c). The turbine layout is not modified, the turbines are only yawed to align with the incoming velocity direction. However, before studying enhanced wake-turbine interaction, the influence of the ambient turbulence characteristics will be evaluated in Paragraph 5.3.2.

5.3.2 Initial configuration

For the sake of comparison, Figure 5.9 shows the flow around the four turbines in the configuration of Figure 5.8(a) without ambient turbulence. For this computation, wake induced turbulence and dissipation are accounted for unsing only the LES model based on the Particle Strength Exchange (PSE) method implemented in the code [18]. The SEM contribution is switched off imposing an absolute constant incoming velocity $U_\infty = 3.2\,m/s$. From Figure 5.9, it can be seen that there is hardly any interaction between the turbines except for a slight wake deflection of the two upstream upper turbines. Besides, the wake extension is very long and exceeds the $12.5\,D$ length presented in this figure. This proves the conservation property of the code even on long distances.

The account for ambient turbulence will drastically modify the flow pattern. From the ample literature existing on the turbulence characterisation of the Alderney Race, only the ambient turbulence values reproduced from the paper of Sentchev *et al.* [29] is tested and presented here. Depending on the ebb or flood conditions and for a distance from bottom of 16 m (which is close to the hub height), two ambient turbulence intensities are encountered : $I_\infty = 10\%$ and $I_\infty = 14\%$. The corresponding integral length scales $\mathscr{L}$ are 26.6 m and 30.0 m respectively. As these values are close, we considered the highest one for the computation but chose to also test out a smaller length scale of $\mathscr{L} = 18$ m. The selected values, $\mathscr{L} = 18$ m and $\mathscr{L} = 30$ m correspond to $\lambda = 27.5$ m and $\lambda = 45.9$ m respectively (according to the linear relationship between turbulent structure size and integral length scale established in Chapter 3).

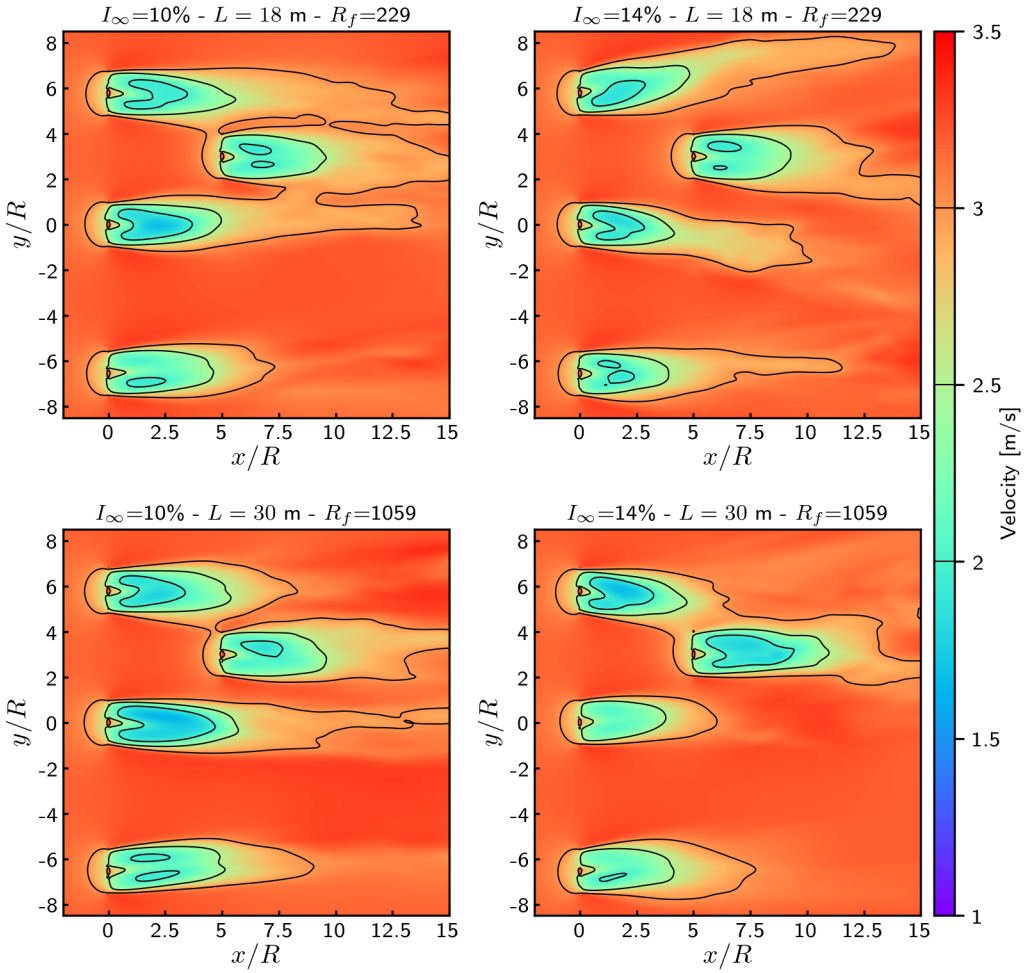

Figure 5.10: *Time-averaged wakes obtained for two turbulence intensities and two integral length scales (TSR=4.1, $\sigma(\lambda) = 75\%$).*

For the four configurations presented in Figure 5.10, a single value of $\sigma(\lambda) = 75\%$ is considered for the variation of the turbulent structure size. Therefore, the only values that differ are the ambient turbulence intensity $I_\infty = 10\%$ or 14% and the associated integral length scale $\mathscr{L} = 18$ m or 30 m. Due to the size of the structures, a filling ratio R_f of one would have led to an incredibly low number of structures (e.g. $N \approx 10$ for $\mathscr{L} = 30$ m) which would have compromised the statistical representation of the flow. Thus, a higher value than $R_f = 1$ had to be chosen and the decision was made to fix fix the number of turbulent structures to $N = 10472$ for all the computations, in order to avoid too much difference between these configurations. Owing to the size of the computational study space, this constant number of $N = 10472$ turbulent structures leads to the filling ratios $R_f = 229$ for $\mathscr{L} = 18$ m and $R_f = 1059$ for $\mathscr{L} = 30$ m. Following the results presented in Figures 5.5, 5.6 and 5.7 of the previous Section, it is anticipated that the wake dissipation will be overestimated. In that sense, the results presented in Figure 5.10 would have a tendency to estimate shorter wakes and hence lower interactions than would be the case in reality. When compared to the result without ambient turbulence of Figure 5.9, the wakes of the four configurations in Figure 5.10 are in fact much shorter. However, mostly due to an increase in wake meandering with ambient turbulence, higher and more numerous interaction phenomena are encountered. In three out of the four studied configurations an interaction phenomenon is observed between an upstream turbine wake and the downstream turbine. Although a higher ambient turbulence intensity sould reduce the wake length, it is not obviously observable from the wake maps of Figure 5.10 nor from the wake lines presented in Figure 5.11. Even though these results are averaged over 188 instantaneous velocity fields, representing an average over 89.6 s of physical time, this should still not be long enough for such high ambient turbulence levels.

The curves presented in Figure 5.11 are very interesting in the way that axial induction is well represented in front of each turbine. A small acceleration in the upstream by-pass can also be observed for the downstream turbine (purple dashed-dotted line). Much longer computations, possibly with a refined discretisation will be required in a near future to better identify the inluence of the integral length scale on the turbine wake. As mentioned in the previous Section, a new asymmetric distribution for the turbulent structure size λ would also improve the results. Firstly, this would lead to a better representation of the physical phenomenon, which is to say many more smaller structures than larger ones for a given central value of λ_0 (see also [88]). Also, and this assertion would need to be further validated, a higher possibility to tend to a filling ratio R_f of one together with a sufficiently high number of structures to enable a statistical representation. If a R_f of one is achievable, the overestimation of the dissipation could be avoided leaving more space for possible variations depending on the integral length scale $\mathscr{L}$ and/or a small variation of ambient turbulence, as it is the case between $I_\infty = 10\%$ and $I_\infty = 14\%$ here. However, the current numerical set-up can already give very interesting insights into interaction configurations, such as in the case of this NEPTHYD layout with an incoming velocity yawed with respect to the main flow direction.

5.3.3 Yawed flows

Figure 5.12 shows the wake configurations for an incoming flow inclined with angle ranging from 5° to 20° with respect to the main current direction. This representation follows the methodology proposed in Figure 5.8 and the plots of Figure 5.12 are similar to the schematic representations of Figure 5.8(c). For these computations, the same numerical parameters are chosen as for $I_\infty = 10\%$ and $\mathscr{L} = 18$ m, imposing $R_f \approx 229$ with $\sigma(\lambda) = 75\%$. All the turbines are rotating at $TSR = 4.1$.

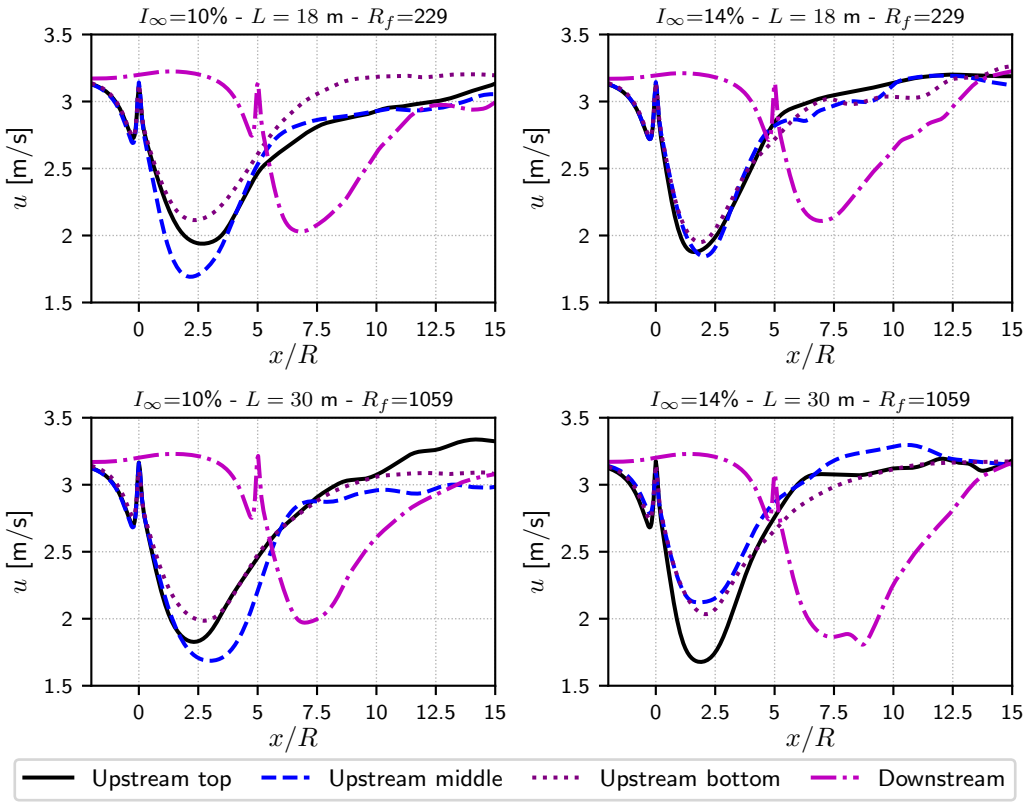

Figure 5.11: *Time-averaged wake lines obtained for two turbulence intensities and two integral length scales (TSR=4.1, $\sigma(\lambda) = 75\%$). For each turbine, the corresponding line passes through its centre.*

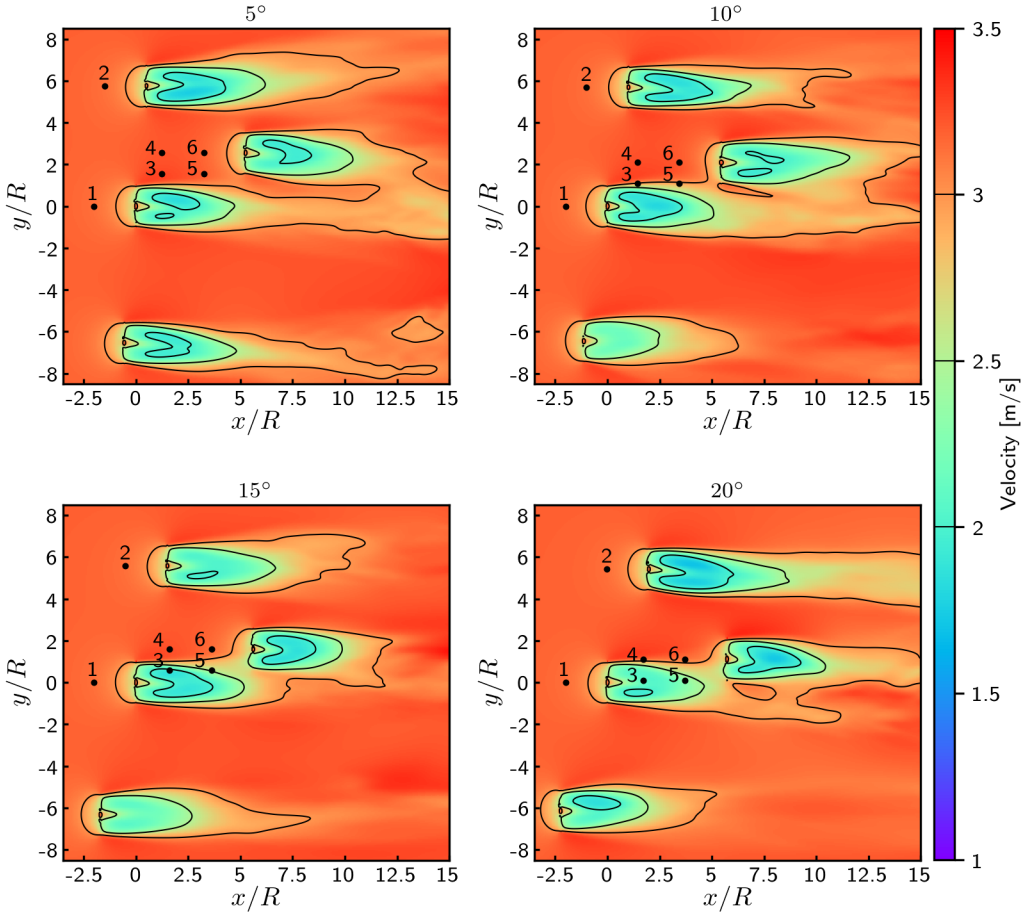

Figure 5.12: *Time-averaged wakes obtained for several yaw angles ($I_\infty = 10\%$, $\mathscr{L} = 18$ m, $Rf \approx 229$, TSR=4.1, $\sigma(\lambda) = 75\%$).*

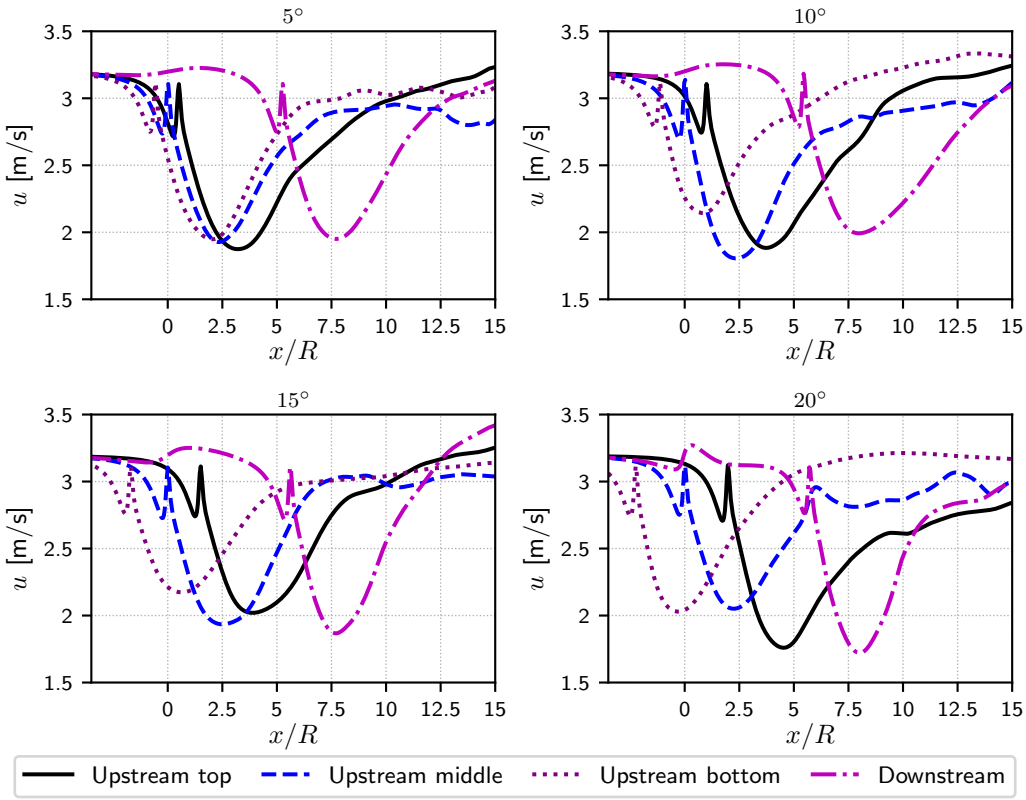

Figure 5.13: *Time-averaged wake lines obtained for four yaw angles ($I_\infty = 10\%$, $L = 18$ m, $Rf \approx 229$, TSR=4.1, $\sigma(\lambda) = 75\%$). For each turbine, the corresponding line passes through its centre.*

Individually, each turbine wake looks similar to those presented in the previous Paragraph. However, as the angle increases, more and more interaction can be observed. At an inclination angle of 10°, a weak interaction can already be observed on the image of Figure 5.12 but nothing is observable on the corresponding wake lines of Figure 5.13 (keeping in mind that the wake lines are taken from the turbine center of rotation and aligned with the turbine direction). Although a weak interaction is visible around the tip of the blades, nothing is yet visible on the lines. However, for the last two configurations with 15° and 20° inclinations of the current, very clear interactions can be observed on the corresponding plots of Figure 5.12. The induction zone of the downstream turbine is clearly connected to the wake of the upstream middle turbine. The interaction is higher for the last 20° case, where approximately half of the downstream turbine is perceiving the upstream wake and also associated additional velocity fluctuations. From the downstream wake lines (violet dashed-dotted lines of Figure 5.13), a small modification is already visible upstream of the turbine but a large modification of the downstream wake is evidenced, the velocity becoming progressively higher for the 15° and 20° inclinations. Such modifications and impacts on the flow perceived by the downstream turbine were anticipated but the present numerical approach can now much better quantify these interactions and even deliver more quantitative information, such as mean velocity deficit, mean shear flow profile and also additional velocity fluctuations.

To better quantify these aspects, numerical probes are defined in the flow domain and are represented by the points denoted from 1 to 6 in each plots of Figure 5.12. Probes 1 and 2 are centred one diameter upstream of the upper and middle upstream turbines

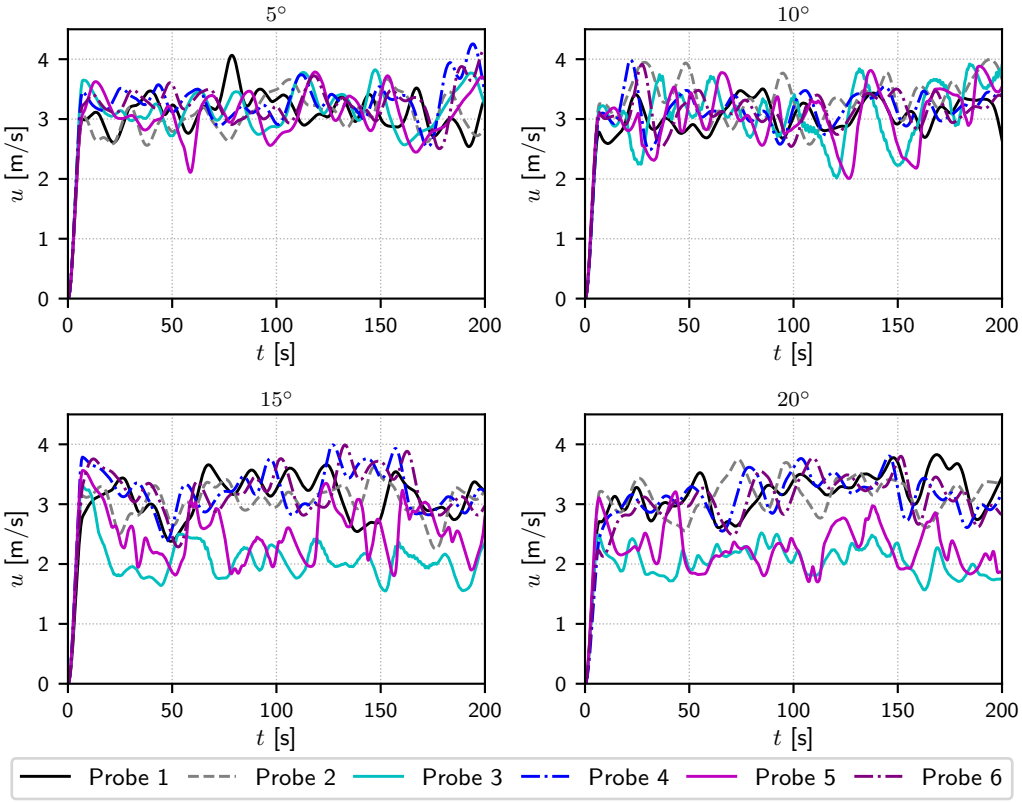

Figure 5.14: *Probes $I_\infty = 10\%$, $L = 18$ m, $Rf \approx 229$, TSR=4.1, $\sigma(\lambda) = 75\%$.*

respectively. These probes are included in order to show the incoming flow disrupted only by ambient turbulence. Probes 4 and 6 are centered one and two diameters upstream of the downstream turbine respectively, whereas probes 3 and 5 are located in front of the blade tip of the downstream turbine, still one and two diameters upstream respectively. These probe locations highly emphasise the tightness of this layout proposed by Engie-Alstom at the time. As it is an official pre-commercial set-up proposed by real major companies in the field, it is worth investigating. The 200 s of velocity measurements recorded by each probe are reproduced for each given configuration in Figure 5.14. This measurement duration is possibly not long enough to have fully converged mean and standard deviation values, but clear tendencies can already been observed on the values shown in Figure 5.15. As anticipated, for a 5° yaw angle, no significant impact can be observed : probes 1 and 2 display a mean velocity a little lower than the far upstream incoming velocity of 3.2 m/s due to axial induction ; probes 3 to 6 display higher values due to a small acceleration in the by-pass ; and a slightly higher mean velocity than 3.2 m/s is recorded for probes 4 and 6 as expected. What's more, no conclusions can be drawn from the standard deviations of these quantities (Figure 5.15(b)). For a 10° yaw angle, some interesting phenomena can be identified. Firstly, probe 2 shows a higher mean velocity value together with a higher standard deviation. There is no other explanation than the possibility of "natural" oscillations due to the passing of turbulent structures which cause the velocity to increase, and were not counterbalanced by a sufficient averaging duration. Probes 3 and 5 show close to the same mean velocity values (Figure 5.15(a)) but highly impacted standard deviations (Fig. 5.15(b)). For these two probes, clear explanations can be given : the mean velocities are not highly impacted because they are at the outer limit of the wake, as shown in Figure 5.12 but a higher standard deviation is observed because these probes are

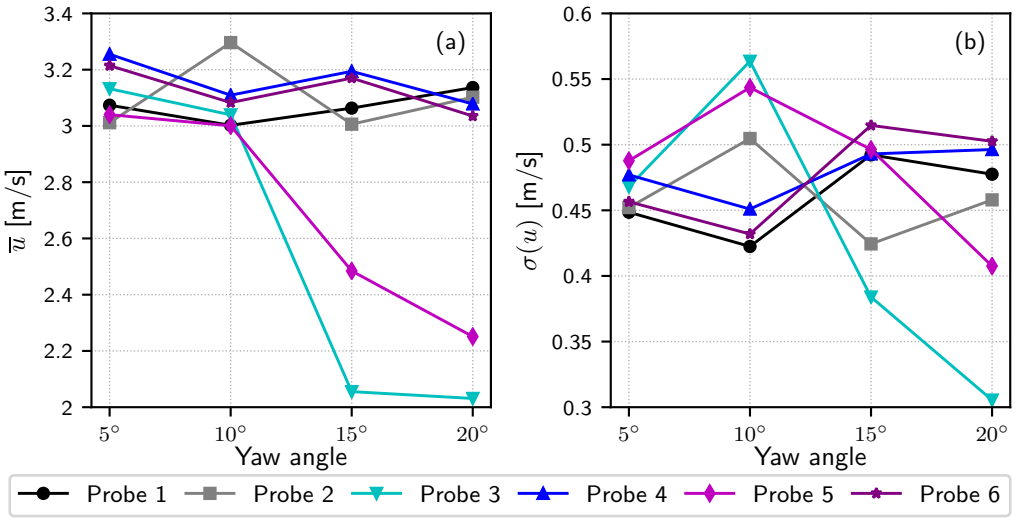

Figure 5.15: *Time average and standard deviation of the velocity u, $I_\infty = 10\%$, $L = 18$ m, $Rf \approx 229$, TSR=4.1, $\sigma(\lambda) = 75\%$.*

in the mixing layer of the wake. As a conclusion for the downstream turbine, the mean flow velocity profile is not highly modified (no real shear in the velocity profile) but the turbine perceives much higher velocity fluctuations at the tip, possibly leading to advanced ageing and possible damage of the blades and drive-train.

For the 15° and 20° yaw angles, these two configurations will be treated together as the evidenced phenomena are similar, although intensified for the higher angle. Probes 1 and 2 show a close to regular behavior, as shown by the averaged velocity (Figure 5.15(a)). The major influence of interaction can be observed for probes 3 and 5 directly from the velocity records of Figure 5.14, showing an important velocity deficit. This deficit translates into a lower averaged velocity value (Figure 5.15(a)), and even more so for the larger yaw angle of 20°. Therefore, the downstream turbine will experience a large shear in the averaged velocity profile since the mean value of probes 4 and 6 remains unchanged. This important shear flow only affects one side of the turbine which inevitably creates load fluctuations. For all four of the tested configurations (from 5° to 20°), these probes are very little affected by the interaction phenomena. Finally, coming back to probes 3 and 5, a decrease of the standard deviations can be observed. This is explained by these probes being situated clearly in the wake of the upstream turbine. This is somewhat obvious, although an increase of these values in the wake would have been expected instead. This aspect needs further validation and confirmation, which would be facilitated by longer simulations : computations run on a longer duration will have much better convergence of these standard deviations. Computations with smaller inter-particles spacing (the Lagrangian equivalent of the mesh size) will also be considered for a better spatial discretisation of the concerned interaction phenomena.

5.4 Conclusions

This Chapter presented an industrial application of the recent implementation of the SEM (Synthetic Eddy Method) in the Lagrangian Vortex framework, using the theoretical basis detailed in Chapter 3. The influence on a turbine wake of parameters such as the turbulence intensity, turbulence integral length scale, the distribution of the turbulent

structure sizes and the turbulent structure filling ratio is isolated and thoroughly analysed. These studies are performed using a 18 m diameter 3 bladed turbine model, of a design similar to that of Alstom's Oceade™ turbine. The upstream mean velocity, turbulence intensities and integral length scales are chosen based on recently published works dedicated to analysing the turbulence characteristics present in the Alderney Race.

The second phase of this study consisted in the simulation and analysis of a four turbine array. This array is the reproduction of the NEPTHYD pre-commercial farm that was granted by the French government in the past year to the consortium composed by Engie-Alstom, just before Alstom-GE decision to stop tidal energy development. In that respect, the tested farm is truly representative of an industrial configuration, both in terms of geometrical layout and of the velocity and turbulence characteristics considered. From the presented results, the individual computed wakes have a downstream extension of approximately 3 to 4 diameters. However, these computations may be a somewhat too dissipative as concluded from the aforementioned analysis of the filling ratio parameter. Unfortunately, the influence of the different turbulence integral length scales did not show clear tendencies in the present results. Nevertheless, this is the first attempt at taking into account the integral length scales for such a configuration and several areas of improvement have been clearly identified. The account for tidal angular asymmetry is also tested on the NEPTHYD four turbine configuration in order to emphasise possible turbine-turbine interaction. At a 10° yaw angle, the downstream turbine is not clearly in the wake of the upstream turbine, and the average velocity profile is not largely affected. However the velocity series computed by numerical probes located $1D$ and $2D$ upstream of the downstream turbine showed increased velocity fluctuations, most probably due to the fact that the tip of the downstream turbine blades is in the mixing layer of the upstream wake. For yaw angles increasing up to 20°, an important shear in the mean velocity profile is experienced all over the blade on nearly half of the turbine swept area. From these two configurations, it is clear that the induced blade and drive train fluctuating loads will be largely affected.

Conclusion

The numerical developments explored in the scope of this work pave the way for possibilities of more complete and realistic simulations of tidal turbines. Various additions and adaptations were theoretically justified and implemented into a complex and multi faceted simulation code, participating to its continuing development and optimisation by adding to its capabilities. A new method for better taking into account turbine blades was devised, together with a new possibility for the computation of efforts. Further advancements were made on the simulation of ambient turbulence, including the validation and use of a pre-existing method in order to reach important conclusions on its various parameters as well as a pre-commercial tidal farm configuration, and the preliminary study of a better physically suited alternative.

The method and preliminary validations presented in the first part of this manuscript have taken this simulation code to the closest it has ever been to an accurate force computation on a full three-dimensional rendition of turbine blades, after years of unfruitful attempts. It had become clear leading up to this PhD work that the account for the turbine blades required an in-depth revision : most importantly due to discrepancies in the computed power curves, but also for a better account of a full detailed turbine geometry, as well as anticipating the future possibility of the simulation of stall. In the literature, simulating three-dimensional turbine blades using combinations of source and dipole singularities appears to be a common practice. However different approaches exist as for the determination of the intensities of the source and dipole contributions, with varying levels of complexity. The exact detailed steps used for determining these intensities are rarely explicited in recent publications, as they are often considered as a long ago established matter. In this respect, the works of Morino [85] have provided a clear context from which a mathematical justification could be retraced to ensure that this singularity method is correctly applied. Thus this work was able to thoroughly detail and justify the implementation of this alternative decomposition. This framework was completed using Ogami's new method for the computation of efforts [86], which allows for a clever work around the issue of obtaining the velocity potential in order to apply Bernoulli's relation. The opportunity was taken to take a closer look into this fairly recent method, by confirming its validation, and then taking it further with a detailed explanation of the computation of the integration constant as well as a decentered alternative of the scheme. Preliminary results and validations of the various implementations added into the code have shown that these methods appear very promising. Although their combination is still on the verge of producing complete satisfying results such as a pressure curve around a three-dimensional turbine blade with an accurate wake, these methods alone are worthy of interest. In order to complete this study, a closer look into blade mesh configurations and the fluid particle emission process may be required, which will provide an opportunity to refine these aspects of the pre-existing simulation code as well.

Also within the aim of better representing all the important factors impacting a real

tidal turbine, the second part of this PhD work continued the developments and analysis begun with the works of Clément Carlier [9] on statistical models to represent ambient turbulence in the Lagrangian framework. Using the adaptation of Jarrin's SEM [91] already implemented into the simulation code, an in depth analysis of the convergence of the method and of the physical properties of reconstructed flows was carried out. This method was also proven to accurately reproduce the qualitative influence of turbulence intensity on the shortening of a turbine wake. These results have served to further validate this unique adaptation of the SEM in a Lagrangian context applied to the entire simulation domain.

Pursuing this study, the alternative divergence-free adaptation of Poletto's DFSEM [46] was explored in order to get closer to a physically consistent representation of a turbulent flow. This alternative method was adapted as well to the Lagrangian framework so that the SEM or DFSEM can be used in the simulation software as wished. The same validations of mathematical and physical properties were performed as for the SEM, concluding that this method results in a faster statistical convergence and close to identical PSDs and length scale relations. However despite the accurate verified reproduction of Reynolds Stress Tensors, the influence of ambient turbulence intensity generated with this method was not yet well evidenced on turbine wakes. A closer look will be required into the implementation of this promising new development.

In light of these results, the initial SEM was chosen for pursuing the analysis of all physical and mathematical parameters of the model on turbine wakes. Some conclusions were straightforward and other seemed more complex, such as the isolation of the influence of the turbulent structure size λ from that of the structure filling ratio R_f. A comparison with flume tank experimental results showed satisfying tendencies for the numerical results, tampered by the fact that the base simulation code appears to be too dissipative, which is more disruptive for low turbulence intensities. Several areas of future refinement were also evidenced, such as the length of the time averages and the distribution of the turbulent structure sizes.

This study culminated in the simulation of a full tidal turbine farm under realistic conditions, including the positioning and yaw of the turbines, the upstream velocity and turbulence intensity, and the turbulent length scales considered in a real pre-commercial tidal site in the Alderney Race. Incidentally, this result also showcases the increasing capabilities of the simulation software, from three-turbine simulations at low turbulence intensities requiring weeks of runtime at the time of Clément Carlier's thesis to this four-turbine configuration at high turbulence intensities currently running in under four days. The end results demonstrated the influence of wake interaction combined with ambient turbulence, two key factors in simulating turbine farms, to which this Lagrangian framework and turbulence account are particularly well suited : the Lagrangian representation of the flow allows for an easy adaptability to any interacting multi-turbine configuration, and the turbulence model guarantees the retention of turbulent intensity throughout any length of simulated area. Interesting conclusions were reached regarding the significant impact of yaw on this industrial tidal site configuration. In the future, a greater range of parameters could be considered, and more complex turbine configurations could be tested out.

Finally, only a small amount of additional verifications should be required in order to achieve the driving objective of this work, which is also the ambition of many current studies : namely the realistic simulation of the influence of ambient turbulence on a fully rendered tidal turbine, with a more accurate computation of localized efforts, and taking into account wake interaction together with additional flow conditions present in realistic

tidal sites. Further developments would then be possible to continue integrating as many realistic site conditions in the simulation tool as possible. A first step could be the addition of a vertical velocity gradient in the incoming upstream velocity to emulate real flow conditions and the effect of bathymetry. The upstream velocity could also be improved with an account for incoming waves, with the use of a Stokes drift type model for instance. The effect of waves would add to the fluctuations on turbine loads, which could be further explored with a structural study of the fatigue and possible deformation of turbine blades when combined with the accurate localized computation of efforts on their detailed geometry. Within these conditions of incoming waves and ambient turbulence, a control law could also be introduced on the rotation of the turbine, to emulate the use of Response Amplitude Operators adapting turbine rotation in response to the fluctuation of loads.

Bibliography

[1] G. Ingram, "Wind turbine analysis using the blade element momentum method," tech. rep., School of Ingineering, Durham University, Durham, UK, October 2011.

[2] M. Togneri and I. Masters, "Synthetic turbulence generation for turbine modelling with BEMT," in *3rd Oxford Tidal Energy Workshop*, (Oxford, UK), 7-8 April 2014.

[3] I. Masters, A. Williams, T. N. Croft, M. Togneri, M. Edmunds, E. Zangiabadi, I. Fairley, and H. Karunarathna, "A comparison of numerical modelling techniques for tidal stream turbine analysis," *Energies*, vol. 8, no. 8, pp. 7833–7853, 2015.

[4] M. Togneri, G. Pinon, C. Carlier, C. Choma Bex, and I. Masters, "Comparison of synthetic turbulence approaches for blade element momentum theory prediction of tidal turbine performance and loads," *Renewable Energy*, vol. 145, pp. 408 – 418, 2020.

[5] U. Ahmed, I. Afgan, D. Apsley, T. Stallard, and P. Stansby, "Cfd simulations of full-scale tidal turbine : comparison of les and rans with field data," in *11th European Wave and Tidal Energy Conference (EWTEC)*, September 2015. Nantes, France.

[6] U. Ahmed, D. Apsley, I. Afgan, T. Stallard, and P. Stansby, "Fluctuating loads on a tidal turbine due to velocity shear and turbulence : Comparison of cfd with field data," *Renewable Energy*, vol. 112, pp. 235 – 246, 2017.

[7] F. Maganga, *Caractérisation numérique et expérimentale des effets d'interaction entre une hydrolienne et le milieu marin.* PhD thesis, Univeristé du Havre, 2011.

[8] P. Mycek, *Étude numérique et expérimentale du comportement d'hydroliennes.* PhD thesis, Université du Havre, 2013.

[9] C. Carlier, *Simulation du comportement d'hydroliennes : modélisation de l'influence de la turbulence ambiante et des effets d'interactions.* PhD thesis, Normandie Université, 2017.

[10] A. Bahaj, W. Batten, and G. McCann, "Experimental verifications of numerical predictions for the hydrodynamic performance of horizontal axis marine current turbines," *Renewable Energy*, vol. 32, no. 15, pp. 2479–2490, 2007.

[11] W. M. J. Batten, A. S. Bahaj, A. F. Molland, and J. R. Chaplin, "The prediction of the hydrodynamic performance of marine current turbines," *Renewable Energy*, vol. 33, no. 5, pp. 1085–1096, 2008.

[12] R. Malki, A. Williams, T. Croft, M. Togneri, and I. Masters, "A coupled blade element momentum – computational fluid dynamics model for evaluating tidal stream turbine performance," *Applied Mathematical Modelling*, vol. 37, no. 5, pp. 3006 – 3020, 2013.

[13] F. Salvatore, Z. Sarichloo, and D. Calcagni, "Marine turbine hydrodynamics by a boundary element method with viscous flow correction," *Journal of Marine Science and Engineering*, May 2018.

[14] P. Mycek, B. Gaurier, G. Germain, G. Pinon, and E. Rivoalen, "Numerical and experimental study of the interaction between two marine current turbines," *International Journal of Marine Energy*, vol. 1, no. 0, pp. 70 – 83, 2013.

[15] J. Falcão de Campos, P. F. de Sousa, and J. Bosschers, "A verification study on low-order three-dimensional potential-based panel codes," *Computers &amp ; Fluids*, vol. 35, no. 1, pp. 61 – 73, 2006.

[16] T. McCombes, C. Johnstone, and A. Grant, "Unsteady wake modelling for tidal current turbines," *IET Renewable Power Generation*, vol. 5, pp. 299–310(11), July 2011.

[17] A. Boujleben, A. Ibrahimbegovic, and E. Lefrançois, "An efficient computational model for fluid-structure interaction in application to large overall motion of wind turbine with flexible blades," *Applied Mathematical Modelling*, vol. 77, pp. 392–407, 2020.

[18] G. Pinon, P. Mycek, G. Germain, and E. Rivoalen, "Numerical simulation of the wake of marine current turbines with a particle method," *Renewable Energy*, vol. 46, no. 0, pp. 111 – 126, 2012.

[19] R. Karsten, A. Swan, and J. Culina, "Assessment of arrays of in-stream tidal turbines in the bay of fundy," *Philosophical Transactions of the Royal Society A : Mathematical,Physical and Engineering Sciences*, vol. 371, no. 1985, pp. –, 2013.

[20] T. Divett, R. Vennell, and C. Stevens, "Optimization of multiple turbine arrays in a channel with tidally reversing flow by numerical modelling with adaptive mesh," *Philosophical Transactions of the Royal Society A : Mathematical, Physical and Engineering Sciences*, vol. 371, p. pp, February 2013.

[21] M. J. Churchfield, Y. Li, and P. J. Moriarty, "A large-eddy simulation study of wake propagation and power production in an array of tidal-current turbines," *Philosophical Transactions of the Royal Society A : Mathematical, Physical and Engineering Sciences*, vol. 371, p. pp, February 2013.

[22] P. Mycek, B. Gaurier, G. Germain, G. Pinon, and E. Rivoalen, "Experimental study of the turbulence intensity effects on marine current turbines behaviour. part II : Two interacting turbines," *Renewable Energy*, vol. 68, no. 0, pp. 876 – 892, 2014.

[23] E. Osalusi, J. Side, and R. Harris, "Structure of turbulent flow in emec's tidal energy test site," *International Communications in Heat and Mass Transfer*, vol. 36, no. 5, pp. 422–431, 2009.

[24] E. Osalusi, J. Side, and R. Harris, "Reynolds stress and turbulence estimates in bottom boundary layer of fall of warness," *International Communications in Heat and Mass Transfer*, vol. 36, no. 5, pp. 412 – 421, 2009.

[25] J. Thomson, B. Polagye, V. Durgesh, and M. Richmond, "Measurements of turbulence at two tidal energy sites in Puget Sound, WA," *IEEE Journal of Oceanic Engineering*, vol. 37, no. 3, pp. 363–374, 2012.

[26] I. A. Milne, R. N. Sharma, R. G. J. Flay, and S. Bickerton, "Characteristics of the turbulence in the flow at a tidal stream power site," *Philosophical Transactions of the Royal Society A : Mathematical, Physical and Engineering Sciences*, vol. 371, p. pp, February 2013.

[27] K. McCaffrey, B. Fox-Kemper, P. E. Hamlington, and J. Thomson, "Characterization of turbulence anisotropy, coherence, and intermittency at a prospective tidal energy site : Observational data analysis," *Renewable Energy*, vol. 76, pp. 441–453, 2015.

[28] M. Thiébaut, J.-F. Filipot, C. Maisondieu, G. Damblans, R. Duarte, E. Droniou, N. Chaplain, and S. Guillou, "A comprehensive assessment of turbulence at a tidal-stream energy site influenced by wind-generated ocean waves," *Energy*, vol. 191, p. 116550, 2020.

[29] A. Sentchev, M. Thiébaut, and S. Guillou, *Turbulence characterization at tidal-stream energy site in Alderney Race*. CRC Press, 2020.

[30] P. Mercier, M. Thiébaut, S. Guillou, C. Maisondieu, E. Poizot, A. Pieterse, J. Thiébot, J.-F. Filipot, and M. Grondeau, "Turbulence measurements : An assessment of acoustic doppler current profiler accuracy in rough environment," *Ocean Engineering*, vol. 226, p. 108819, 2021.

[31] L. Furgerot, A. Sentchev, P. Bailly du Bois, G. Lopez, M. Morillon, E. Poizot, Y. Méar, and A.-C. Bennis, "One year of measurements in alderney race : preliminary results from database analysis," *Philosophical Transactions of the Royal Society A : Mathematical, Physical and Engineering Sciences*, vol. 378, 2020.

[32] A. Sentchev, T. D. Nguyen, L. Furgerot, and P. Bailly du Bois, "Underway velocity measurements in the alderney race : towards a three-dimensional representation of tidal motions," *Philosophical Transactions of the Royal Society A : Mathematical, Physical and Engineering Sciences*, vol. 378, 2020.

[33] M. Thiébaut, J.-F. Filipot, C. Maisondieu, G. Damblans, C. Jochum, L. F. Kilcher, and S. Guillou, "Characterization of the vertical evolution of the three-dimensional turbulence for fatigue design of tidal turbines," *Philosophical Transactions of the Royal Society A : Mathematical, Physical and Engineering Sciences*, vol. 378, 2020.

[34] M. Thiébaut, J.-F. Filipot, C. Maisondieu, G. Damblans, R. Duarte, E. Droniou, and S. Guillou, "Assessing the turbulent kinetic energy budget in an energetic tidal flow from measurements of coupled ADCPs," *Philosophical Transactions of the Royal Society A : Mathematical, Physical and Engineering Sciences*, vol. 378, 2020.

[35] A. C. L. Bourgoin, S. S. Guillou, J. Thiébot, and R. Ata, "Turbulence characterization at a tidal energy site using large-eddy simulations : case of the alderney race," *Philosophical Transactions of the Royal Society A : Mathematical, Physical and Engineering Sciences*, vol. 378, 2020.

[36] N. Guillou, S. P. Neill, and J. Thiébot, "Spatio-temporal variability of tidal-stream energy in north-western europe," *Philosophical Transactions of the Royal Society A : Mathematical, Physical and Engineering Sciences*, vol. 378, 2020.

[37] G. Lopez, A.-C. Bennis, Y. Barbin, A. Sentchev, L. Benoit, and L. Marié, "Surface currents in the alderney race from high-frequency radar measurements and three-dimensional modelling," *Philosophical Transactions of the Royal Society A : Mathematical, Physical and Engineering Sciences*, vol. 378, 2020.

[38] P. Bailly du Bois, F. Dumas, M. Morillon, L. Furgerot, C. Voiseux, E. Poizot, Y. Méar, and A.-C. Bennis, "The alderney race : general hydrodynamic and particular features," *Philosophical Transactions of the Royal Society A : Mathematical, Physical and Engineering Sciences*, vol. 378, 2020.

[39] N. Jarrin, S. Benhamadouche, D. Laurence, and R. Prosser, "A synthetic-eddy-method for generating inflow conditions for large-eddy simulations," *International Journal of Heat and Fluid Flow*, vol. 27, pp. 585–593, 2006.

[40] P. Bernard, A. Viré, V. Moureau, G. Lartigue, L. Beaudet, P. Deglaire, and L. Bricteux, "Large-eddy simulation of wind turbines wakes including geometrical effects," *Computers And Fluids*, vol. 173, pp. 133–139, 2018.

[41] P. Mercier, M. Grondeau, S. Guillou, J. Thiébot, and E. Poizot, "Numerical study of the turbulent eddies generated by the seabed roughness. case study at a tidal power site," *Applied Ocean Research*, vol. 97, p. 102082, 2020.

[42] P. Chatelain, S. Backaert, G. Winckelmans, and S. Kern, "Large eddy simulation of wind turbine wakes," *Flow Turbulence and Combustion*, vol. 91, pp. 587–605, 2013.

[43] M. Bossy, J. Espina, J. Moricel, C. Paris, and A. Rousseau, "Modeling the wind circulation around mills with a lagrangian stochastic approach," *The SMAI journal of computational mathematics*, vol. 2, pp. 177–214, 2016.

[44] G. Pinon, C. Carlier, A. Fur, B. Gaurier, G. Germain, and E. Rivoalen, "Account of ambient turbulence for turbine wakes using a synthetic-eddy-method," *Journal of Physics : Conference Series*, vol. 854, no. 1, p. 012016, 2017.

[45] P. Mycek, G. Pinon, C. Lothodé, A. Dezotti, and C. Carlier, "Iterative solver approach for turbine interactions : application to wind or marine current turbine farms," *Applied Mathematical Modelling*, vol. 41, pp. 331 – 349, 2017.

[46] R. Poletto, *Divergence free develoment of the Synthetic Eddy Method in order to improve synthetic turbulence for embedded LES simulations*. PhD thesis, University of Manchester, 2014.

[47] L. Rosenhead, "The formation of vortices from a surface of discontinuity," *Proc. Roy. Soc. London*, vol. A(134), pp. 170–192, 1931.

[48] A. Chorin, "Vortex sheet approximation of boundary layers," *J. Comput. Phys.*, vol. 27, pp. 428–442, 1978.

[49] A. Leonard, "Vortex methods for flow simulation," *Journal of Computational Physics*, vol. 37, no. 3, pp. 289–335, 1980.

[50] C. Rehbach, "Calcul numérique d'écoulements tridimensionnels instationnaires avec nappes tourbillonaires," *La Recherche Aérospatiale*, vol. 5, pp. 289–298, 1977.

[51] J. Hess, "Calculation of potential flow about arbitrary three dimensional lifting bodies," tech. rep., Final Technical Report, McDonnel Douglas Report No. MDC J5679-01 - Also AD 755 480, 1972.

[52] A. H.-D. Cheng and D. T. Cheng, "Heritage and early history of the boundary element method," *Engineering Analysis with Boundary Elements*, vol. 29, pp. 268–302, 2005.

[53] J. Bousquet, *Méthode des singularités*. Cépaduès - Editions, 1990.

[54] E. Rivoalen and S. Huberson, "Numerical simulation of axisymmetric viscous flows by means of a particle method," *Journal of Computational Physics*, vol. 152, no. 1, pp. 1 – 31, 1999.

[55] F. Hauville, *Optimisation des méthodes de calculs d'écoulements tourbillonnaires instationnaires*. PhD thesis, Université du Havre, January 1996.

[56] O. Le Maˆ itre, S. Huberson, and E. Souza De Cursi, "Unsteady model of sail and flow interaction," *Journal of Fluids and Structures*, vol. 13, pp. 37–59, 1999.

[57] F. Hauville and Y. Roux, "Réglage dynamique d'une voile par une méthode d'intéraction fluide/structure," in *9èmes Journées de l'Hydrodynamique*, 2003.

[58] G. Pinon, *Modélisation numérique de jets transverses : Application au cas des inverseurs de poussée d'un avion en phase d'atterrissage*. PhD thesis, Université du Havre, 2005.

[59] G. Pinon, H. Bratec, S. Huberson, G. Pignot, and E. Rivoalen, "Vortex method for simulation of a 3D round jet in a cross-stream," *Journal of Turbulence*, vol. 6, no. 18, pp. 1–25, 2005.

[60] G. S. Winckelmans and A. Leonard, "Contributions to vortex particle methods for the computation of three-dimensional incompressible unsteady flows," *Journal of Computational Physics*, vol. 109, no. 2, pp. 247–273, 1993.

[61] J. T. Beale and A. Majda, "High order accurate vortex methods with explicit velocity kernels," *Journal of Computational Physics*, vol. 58, pp. 188–208, 1985.

[62] G. K. Batchelor, *An introduction to fluid dynamics*. Cambridge University Press, UK, 1967.

[63] P. Mycek, G. Pinon, G. Germain, and Élie Rivoalen, "A self-regularising DVM–PSE method for the modelling of diffusion in particle methods," *Comptes Rendus Mécanique*, vol. 341, no. 9–10, pp. 709 – 714, 2013.

[64] B. Cantaloube and S. Huberson, "Calcul d'écoulements de fluide incompressible non visqueux autour de voilures tournantes par une méthode particulaire," *La Recherche Aérospatiale*, vol. 6, pp. 403–415, 1986.

[65] N. N. Mansour, "Numerical simulation of the tip vortex off a low-aspect ratio wing at transonic speed," in *AIAA 22nd Aerospace Sciences Meeting* (A. I. of Aeronautics and Astronautics, eds.), (Reno, Nevada, USA), January 1984.

[66] J.-P. Choquin and G.-H. Cottet, "Sur l'analyse d'une classe de méthodes de vortex tridimensionnelles," *C. R. Acad. Sci.*, vol. 306, pp. 739–742, May 1988. Série I.

[67] E. Rivoalen, *Etude numérique et experimentale de tourbillons de sillage proches d'une surface libre*. PhD thesis, Université du Havre, 1994.

[68] P. Degond and S. Mas-Gallic, "The weighted particle method for convection-diffusion equations. Part I : The case of an isotropic viscosity," *Math. Comp.*, vol. 53, no. 188, pp. 485–507, 1989.

[69] J. Choquin and S. Huberson, "Particles simulation of viscous flow," *Computers &amp ; Fluids*, vol. 17, no. 2, pp. 397 – 410, 1989.

[70] P. Sagaut, *Large Eddy Simulation for Incompressible Flows : an Introduction*. Scientific Computation, Springer, 2006.

[71] J. Mansfield, O. Knio, and C. Meneveau, "Dynamic les of colliding vortex rings using a 3d vortex method," *J. Comp. Phys.*, vol. 152, no. Issue 1, pp. 305–345, 1999.

[72] J. R. Mansfield, O. M. Knio, and C. Meneveau, "Dynamic les of colliding vortex rings using a 3d vortex method," *Journal of Computational Physics*, vol. 152, no. 1, pp. 305–345, 1999.

[73] N. Mansour, J. Ferziger, and W. Reynolds, "Large-eddy simulation of a turbulent mixing layer," tech. rep., Report TF-11, Thermosciences Div., Dept. of Mech. Eng., Stanford University, 1978.

[74] Y. Ogami and T. Akamatsu, "Viscous flow simulation using the discrete vortex model - the diffusion velocity method," *Computers & Fluids*, vol. 19, no. 3-4, pp. 433–441, 1991.

[75] P. Mycek, G. Pinon, G. Germain, and E. Rivoalen, "Formulation and analysis of a diffusion-velocity particle model for transport-dispersion equations," *Computational and Applied Mathematics*, vol. 35, no. 2, pp. 447–473, 2016.

[76] K. Lindsay and R. Krasny, "A particle method and adaptive treecode for vortex sheet motion in three-dimensional flow," *Journal of Computational Physics*, vol. 172, no. 2, pp. 879–907, 2001.

[77] Y. M. Marzouk and A. F. Ghoniem, "K-means clustering for optimal partitioning and dynamic load balancing of parallel hierarchical N-body simulations," *Journal of Computational Physics*, vol. 207, pp. 493–528, 2005.

[78] P. Mycek, B. Gaurier, G. Germain, G. Pinon, and E. Rivoalen, "Experimental study of the turbulence intensity effects on marine current turbines behaviour. part I : One single turbine," *Renewable Energy*, vol. 66, no. 0, pp. 729 – 746, 2014.

[79] C. Carlier, P. Mycek, B. Gaurrier, G. Germain, G. Pinon, and E. Rivoalen, "Étude expérimentale et numérique du comportement d'hydroliennes à axe horizontale," in *XIIIèmes Journées Nationales Génie Côtier – Génie Civil*, Juillet 2014. Dunkerque, France.

[80] B. Gaurier, C. Carlier, G. Germain, G. Pinon, and E. Rivoalen, "Three tidal turbines in interaction : An experimental study of turbulence intensity effects on wakes and turbine performance," *Renewable Energy*, vol. 148, pp. 1150 – 1164, 2020.

[81] V. A. Riziotis and S. G. Voutsinas, "Dynamic stall modelling on airfoils based on strong viscous–inviscid interaction coupling," *International Journal for Numerical Methods in Fluids*, vol. 56, no. 2, pp. 185–208, 2008.

[82] L. Greco, F. Salvatore, and F. D. Felice, "Validation of a quasi–potential flow model for the analysis of marine propellers wake," in *Twenty-Fifth Symposium on Naval Hydrodynamics*, (St. John's, Newfoundland, Canada), August 2004.

[83] F. Salvatore, F. Bellotto, D. Calcagni, F. D. Felice, D. Dhomé, and J.-C. Allo, "Validation of a computational hydrodynamics model for horizontal-axis marine current turbines," in *10th European Wave and Tidal Energy Conference (EWTEC)*, 6-11th Sept. 2015 2015. Nantes, France.

[84] F. Salvatore, C. Testa, and L. Grego, "A viscous/inviscid coupled formulation for unsteady sheet cavitation modelling of marine propellers," in *Fifth International Symposium on Cavitation*, (Osaka, Japan), November 2003.

[85] L. Morino, *Nonlinear Problems of Fluid Dynamics*, vol. 6 of *Developments in Boundary Element Methods*, ch. Helmholtz and Poincaré Potential-Vorticity Decompositions for the Analysis of Unsteady Compressible Viscous Flows, pp. 1–54. Elsevier Applied Science Publishers, 1990.

[86] Y. Ogami, "A three-dimensional source-vorticity method for simulating incompressible potential flows around a deforming body without the kutta condition," *Computers and Fluids*, vol. 154, pp. 184–199, 2017.

[87] C. E. Brennen, "A review of added mass and fluid inertial forces," tech. rep., Department of the Navy, Port Hueneme, CA, USA, 1982.

[88] C. Choma Bex, C. Carlier, A. Fur, G. Pinon, G. Germain, and E. Rivoalen, "A stochastic method to account for the ambient turbulence in lagrangian vortex computations," *Applied Mathematical Modelling*, vol. 88, pp. 38 – 54, 2020.

[89] J. Mansfield, O. Knio, and C. Meneveau, "Towards lagrangian large vortex simulation," in *ESAIM : Proceedings, Vol. 1*, pp. 49–64, 1996.

[90] J. Mansfield, O. Knio, and C. Meneveau, "A dynamic LES scheme for the vorticity transport equation : formulation and a priori tests," *J. Comp. Phys.*, vol. 145, no. Issue 2, pp. 693–730, 1998.

[91] N. Jarrin, *Synthetic Inflow boundary conditions for the numerical simulation of turbulence*. PhD thesis, University of Manchester, 2008.

[92] I. Afgan, J. McNaughton, S. Rolfo, D. Apsley, T. Stallard, and P. Stansby, "Turbulent flow and loading on a tidal stream turbine by les and rans," *International Journal of Heat and Fluid Flow*, vol. 43, pp. 96–108, 2013.

[93] M. Togneri and I. Masters, "Parametrising turbulent marine flows for a blade element momentum model of tidal stream turbines," in *9th European Wave and Tidal Energy Conference (EWTEC)*, September 2011. Southampton, UK.

[94] B. J. Jonkman and L. Kilcher, "Turbsim user's guide : Version 1.06.00," tech. rep., National Renewable Energy Laboratory, September 2012.

[95] M. Togneri, I. Masters, C. Carlier, C. Choma Bex, and G. Pinon, "Comparison of synthetic turbulence approaches for two numerical tidal turbine models," in *Proceedings of the Twelfth European Wave and Tidal Energy Conference* (A. Lewis, ed.), (University College Cork, Ireland), pp. 765 1–765 10, EWTEC, Aug 27–Sep 1 2017. ISSN : 2309-1983.

[96] J. Mann, "The spatial structure of neutral atmosphere surface-layer turbulence," *Journal of Fluid Mechanics*, vol. 273, pp. 141–168, 1994.

[97] P. Chatelain, M. Duponcheel, S. Zeoli, S. Buffin, D.-G. Caprace, G. Winckelmans, and L. Bricteux, "Investigation of the effect of inflow turbulence on vertical axis wind turbine wakes," *Journal of Physics : Conference Series (Print)*, vol. 854, no. 1, p. 012011, 2017.

[98] G. Cottet and P. Koumoutsakos, *Vortex methods : theory and practice*. Cambridge University Press, 2000.

[99] T. S. Lund, X. Wu, and K. D. Squires, "Generation of turbulent inflow data for spatially-developing boundary layer simulations," *Journal of Computational Physics*, vol. 140, pp. 233–258, 1998.

[100] O. D. Medina, F. Schmitt, R. Calif, G. Germain, and B. Gaurier, "Correlation between synchronised power and flow measurements, a way to characterize turblence effecs on marine current turbine.," in *11th European Wave and Tidal Energy Conference (EWTEC)*, September 2015. Nante, France.

[101] G. K. Batchelor, *The Theory of Homogeneous Turbulence*. Cambridge University Press, 1953.

[102] O. D. Medina, F. G. Schmitt, R. Calif, G. Germain, and B. Gaurier, "Turbulence analysis and multiscale correlations between synchronized flow velocity and marine turbine power production," *Renewable Energy*, vol. 112, pp. 314 – 327, 2017.

[103] C. Carlier, G. Pinon, B. Gaurier, G. Germain, and E. Rivoalen, "A synthetic eddy-method to represent the ambient turbulence in numerical simulation of marine current turbine," in *10th European Wave and Tidal Energy Conference (EWTEC)*, September 2015. Nantes, France.

[104] R. Poletto, T. Craft, and A. Revell, "A new divergence free synthetic eddy method for the reproduction of inlet flow conditions for les," *Flow, Turb. and Combustion*, vol. 91, pp. 519–539, 2013.

[105] A. A. Environnementale, "Projet nepthyd," tech. rep., Conseil Général de l'environement et du développement durable : http ://www.cgedd.developpement-durable.gouv.fr, last acces 2016, June the 16th.

[106] C. Choma Bex, G. Pinon, M. Slama, B. Gaston, G. Germain, and E. Rivoalen, "Lagrangian Vortex computations of turbine wakes : recent improvements using Poletto's Synthetic Eddy Method (SEM) to account for ambient turbulence," in *The Science of Making Torque from Wind (TORQUE 2020)*, (Delft, The Netherlands), 28 sept - 02 October 2020.

[107] F. Maganga, G. Germain, J. King, G. Pinon, and E. Rivoalen, "Experimental characterisation of flow effects on marine current turbine behaviour and on its wake properties," *IET Renewable Power Generation*, vol. 4, no. 6, pp. 498–509, 2010.

[108] N. Maslov, J.-F. Charpentier, and C. Claramunt, "A modelling approach for a cost-based evaluation of the energy produced by a marine energy farm," *International Journal of Marine Energy*, vol. 9, pp. 1 – 19, 2015.

Appendix A

Deriving coefficients for the shape function used in Poletto's DFSEM

Beginning from relation (6.2.10) of Poletto's thesis [46] :

$$\langle u_i' \, u_i' \rangle = \frac{1}{N} \sum_{k=1}^{N} \left\langle \frac{[q_\sigma(d^k)]^2}{(d^k)^6} \left[(d^k)^2 - (r_i^k)^2 \right] \right\rangle \, . \tag{A.1}$$

This is the i^{th} component of the average of the fluctuations of the turbulent kinetic energy. However for $i = 1, 2$ or 3 we have : $\langle u_i' \, u_i' \rangle = 1$. When adding the three components we obtain :

$$\langle u_1' \, u_1' + u_2' \, u_2' + u_3' \, u_3' \rangle = \frac{1}{N} \sum_{k=1}^{N} \left\langle \frac{[q_\sigma(d^k)]^2}{(d^k)^6} \left[3(d^k)^2 - \left((r_1^k)^2 + (r_2^k)^2 + (r_3^k)^2 \right) \right] \right\rangle \, , \tag{A.2}$$

i.e.

$$(d^k)^2 = (r_1^k)^2 + (r_2^k)^2 + (r_3^k)^2 \, , \tag{A.3}$$

and

$$\langle u_1' \, u_1' + u_2' \, u_2' + u_3' \, u_3' \rangle = 3 \, , \tag{A.4}$$

thus :

$$\frac{1}{N} \sum_{k=1}^{N} \left\langle \frac{[q_\sigma(d^k)]^2}{(d^k)^4} \right\rangle = \frac{3}{2} \, . \tag{A.5}$$

$q_\sigma(d^k)$ is a radially symmetric function which must verify a number of properties given in Poletto's thesis. One such function verifying the appropriate conditions is given by :

$$q_\sigma(d^k) = B \left(\sin(\pi d^k) \right)^2 \cdot d^k \, , \tag{A.6}$$

with B a constant value to be determined. By replacing the function $q_\sigma(d^k)$ in Equation (A.5) we have :

$$\frac{[q_\sigma(d^k)]^2}{(d^k)^4} \; = \; B^2 \frac{\left(\sin(\pi d^k) \right)^4}{(d^k)^2} \, . \tag{A.7}$$

We suppose a uniform probability distribution for the average operator $< \cdot >$.

The shape function $q_\sigma(d^k)$ is defined inside a sphere of volume V_B and radius σ, thus :

$$\left\langle \frac{[q_\sigma(d^k)]^2}{(d^k)^4} \right\rangle = B^2 \left\langle \frac{\left(\sin(\pi d^k) \right)^4}{(d^k)^2} \right\rangle = \frac{B^2}{V_B} \int_{\text{Boule}} \frac{\left(\sin(\pi d^k) \right)^4}{(d^k)^2} dV \, . \tag{A.8}$$

By spheric integration, noting $d^k = r/\sigma$:

$$\int_{\text{Boule}} \frac{\left(\sin(\pi d^k)\right)^4}{(d^k)^2} dV = \int_0^{\pi} \sin\phi \, d\phi \cdot \int_0^{2\pi} d\theta \cdot \int_0^{\sigma} \frac{(\sin(\pi r/\sigma))^4}{(r/\sigma)^2} r^2 dr \, . \tag{A.9}$$

Let $u = r/\sigma$, by laking the linearised approximation $(\sin(\pi u))^4 = (\cos(4\pi u) - 4\cos(2\pi u) + 3)/8$ Equation (A.8) becomes :

$$\begin{aligned} \frac{B^2\sigma^3}{V_B} \int_{\text{Boule}} \frac{\left(\sin(\pi d^k)\right)^4}{(d^k)^2} dV &= \frac{B^2\sigma^3}{V_B} \cdot (2) \cdot (2\pi) \cdot \left(\int_0^1 (\cos(4\pi u) - 4\cos(2\pi u))/8 \, du + \int_0^1 3/8 \, du \right) \\ &= \frac{B^2\sigma^3}{V_B} \cdot \frac{3}{2}\pi \, . \end{aligned} \tag{A.10}$$

By combining this result with Equation (A.5) we deduce the value of the constant B :

$$B = \sqrt{\frac{V_B}{\pi\sigma^3}} \, . \tag{A.11}$$

Finally when integrating this constant into the formulation of the shape function given by Equation (A.6), we obtain the finale expression of q_σ for this specific function :

$$q_\sigma(d^k) = \sqrt{\frac{V_B}{\pi\sigma^3}} \left(\sin(\pi d^k)\right)^2 \cdot d^k \, . \tag{A.12}$$

Author : Camille Choma Bex

Abstract : In the current context of diversification of renewable energies, tidal turbines are set to occupy an important niche, and numerical simulation is a crucial tool for their investigation. The in-house simulation code DOROTHY developed in collaboration between IFREMER and LOMC uses the Vortex Particle Method offering a good compromise between physical realism and and computational time. Some additional developments are required in order to make of this software a fully rounded numerical tool able to mimic advanced realistic configurations. Firstly, an important overhaul of its computation of loads has been undertaken, including a new framework to represent the previously simplified and now fully-rendered turbine blades. This endeavour includes the mathematical justification, investigation, and preliminary validation of additional integral methods accounting for the turbine body. Secondly, the importance of the impact of ambient turbulence on the wake interaction and power output within a turbine farm cannot be ignored. This element is introduced using a Synthetic Eddy Method uniquely adapted to the present Lagrangian framework. All aspects of this method as well as a promising alternative are closely examined, culminating in the demonstration of its capabilities for the simulation of the flow and prediction of detrimental interaction effects throughout a projected four turbine pilot farm configuration.

Keywords : Numerical simulation, Tidal turbine, Ambient turbulence, Synthetic Eddy Method, Interaction, Wake, Performance, Integral method, Singularity method

---

Autrice : Camille Choma Bex

Résumé : Dans le contexte actuel de diversification du panel d'énergies renouvelables, les hydroliennes sont sur la voie pour occuper une niche importante, et la simulation numérique est un outil essentiel pour leur étude. Le code de simulation DOROTHY développé en collaboration entre l'IFREMER et le LOMC utilise la méthode Vortex particulaire, qui offre un bon compromis entre réalisme physique et temps de simulation. Des développements supplémentaires sont nécessaires pour faire de ce logiciel un outil complet capable de simuler des configurations réalistes. Tout d'abord, une révision en profondeur du calcul d'efforts a été entreprise, comprenant un nouveau formalisme pour la représentation jusqu'ici simplifiée et à présent fidèlement détaillée des pales de la turbine. Cette contribution inclut la justification mathématique, l'étude, et la validation préliminaire de méthodes intégrales supplémentaires pour la prise en compte du corps de l'hydrolienne. Par ailleurs, l'importance de l'impact de la turbulence ambiante sur l'interaction de sillages et la production de puissance au sein d'une ferme d'hydroliennes ne peut être ignorée. Cet élément est introduit avec l'utilisation d'une méthode synthétique de la turbulence, adaptée pour une prise en compte Lagrangienne. Tous les éléments de cette méthode ainsi qu'une alternative prometteuse sont examinés soigneusement, aboutissant à la démonstration de ses capacités à simuler l'écoulement et prédire des effets indésirables au travers d'une configuration de ferme pilote hydrolienne de quatre machines.

Mots-clé : Simulation numérique, Hydrolienne, Turbulence ambiante, Synthetic Eddy Method, Interaction, Sillage, Performances, Méthodes intégrales, Méthode des singularités